



Additional Testing of the DHC-6 Twin Otter Tailplane Iced Airfoil Section in the Ohio State University 7x10 Low Speed Wind Tunnel

Gerald Gregorek, John J. Dresse, and Karine La Noé
Ohio State University, Columbus, Ohio

The NASA STI Program Office . . . in Profile

Since its founding, NASA has been dedicated to the advancement of aeronautics and space science. The NASA Scientific and Technical Information (STI) Program Office plays a key part in helping NASA maintain this important role.

The NASA STI Program Office is operated by Langley Research Center, the Lead Center for NASA's scientific and technical information. The NASA STI Program Office provides access to the NASA STI Database, the largest collection of aeronautical and space science STI in the world. The Program Office is also NASA's institutional mechanism for disseminating the results of its research and development activities. These results are published by NASA in the NASA STI Report Series, which includes the following report types:

- **TECHNICAL PUBLICATION.** Reports of completed research or a major significant phase of research that present the results of NASA programs and include extensive data or theoretical analysis. Includes compilations of significant scientific and technical data and information deemed to be of continuing reference value. NASA's counterpart of peer-reviewed formal professional papers but has less stringent limitations on manuscript length and extent of graphic presentations.
- **TECHNICAL MEMORANDUM.** Scientific and technical findings that are preliminary or of specialized interest, e.g., quick release reports, working papers, and bibliographies that contain minimal annotation. Does not contain extensive analysis.
- **CONTRACTOR REPORT.** Scientific and technical findings by NASA-sponsored contractors and grantees.

- **CONFERENCE PUBLICATION.** Collected papers from scientific and technical conferences, symposia, seminars, or other meetings sponsored or cosponsored by NASA.
- **SPECIAL PUBLICATION.** Scientific, technical, or historical information from NASA programs, projects, and missions, often concerned with subjects having substantial public interest.
- **TECHNICAL TRANSLATION.** English-language translations of foreign scientific and technical material pertinent to NASA's mission.

Specialized services that complement the STI Program Office's diverse offerings include creating custom thesauri, building customized data bases, organizing and publishing research results . . . even providing videos.

For more information about the NASA STI Program Office, see the following:

- Access the NASA STI Program Home Page at <http://www.sti.nasa.gov>
- E-mail your question via the Internet to help@sti.nasa.gov
- Fax your question to the NASA Access Help Desk at (301) 621-0134
- Telephone the NASA Access Help Desk at (301) 621-0390
- Write to:
NASA Access Help Desk
NASA Center for Aerospace Information
7121 Standard Drive
Hanover, MD 21076



Additional Testing of the DHC-6 Twin Otter Tailplane Iced Airfoil Section in the Ohio State University 7x10 Low Speed Wind Tunnel

Gerald Gregorek, John J. Dresse, and Karine La Noé
Ohio State University, Columbus, Ohio

Prepared under Grant NAG3-1574

National Aeronautics and
Space Administration

Glenn Research Center

Acknowledgments

The authors would like to thank the NASA Glenn Research Center Icing Branch for sponsoring this wind tunnel test through the grant NAG3-1574 to the Ohio State University. We also would like to acknowledge the project advocacy and support that the FAA William J. Hughes Technical Center provided throughout this research effort.

Trade names or manufacturers' names are used in this report for identification only. This usage does not constitute an official endorsement, either expressed or implied, by the National Aeronautics and Space Administration.

Available from

NASA Center for Aerospace Information
7121 Standard Drive
Hanover, MD 21076
Price Code: A05

National Technical Information Service
5285 Port Royal Road
Springfield, VA 22100
Price Code: A05

Table of Contents

Section	Page
Nomenclature	iv
I. Summary	1
II. Introduction	2
III. Experimental Facility	4
IV. Model Description	5
a) Airfoil Sections.....	5
b) Ice Shapes.....	6
V. Data Acquisition	13
VI. Test Procedure	14
VII. Data Reduction	15
VIII. Results and Discussion.....	17
a) Ice Shape Effects	17
b) Velocity Effects	18
c) Repeatability	18
d) Section Effects.....	18
IX. Conclusions.....	33
Appendix A. Tap Locations	35
Appendix B. Run Log	41
Appendix C. Solid Wall Correction Calculations.....	43
Appendix D. Data Reduction Output File Formats	47
Appendix E. DHC-6 Twin Otter Tailplane Coefficient Data	49
Appendix F. IRT Ice Shape Information.....	79
References	81

Nomenclature

α, AOA	angle-of-attack
α_{stall}	angle-of-attack at stall
δ_e	elevator deflection
AOA, α	angle-of-attack
c	chord
C_D	section drag coefficient
C_{D0}	section drag coefficient at $\alpha=0^\circ$
C_H	section hinge moment coefficient
C_L	section lift coefficient
$C_{L\text{max}}$	peak section lift coefficient
$C_{M\cdot CM1/4}$	section moment about 1/4 chord
C_p	pressure coefficient
P_{total}	total pressure
P_{static}	static pressure
q, Q	dynamic pressure
V	velocity

I. Summary

In an effort to investigate the Ice Contaminated Tailplane Stall (ICTS) phenomenon, a full scale 2-Dimensional tailplane airfoil model of the NASA Glenn Research Center DeHavilland DHC-6 Twin Otter Icing Research Aircraft was tested in The Ohio State University 7×10 ft. wind tunnel. This test was a continuation of a similar wind tunnel test which took place in 1994. Two additional leading edge ice contours were added to the previous investigations' test matrix.

The primary Twin Otter tailplane consists of two airfoil sections. The first airfoil, Section 1, is used on approximately 70% of the entire tailplane span. This airfoil was tested uniced, and with four representative ice shapes attached to the leading edge, with angles of attack ranging from small positive to large negative values. The ice shapes were designated according to either the program that created them or their place of origin. The four ice representations were named S&C, LEWICE, IRT1 and IRT2. These shapes are representative of four potential ice formations. Aerodynamic coefficients, C_L , C_M , and C_H were obtained by integrating static pressure coefficient, C_P , values obtained from surface taps. Testing was accomplished for the most part at 60 kts, but some higher speed tests were run at 100 kts. The second airfoil, Section 2, is used on 30% of the tailplane span and was also tested uniced, with maximum positive and negative elevator deflections. In addition to testing the representative ice shapes, a carborundum grit was applied to the leading edge to determine what, if any, effects were produced by a light debris buildup.

Surprisingly, the generic ice shape models (S&C and LEWICE) produced more detrimental effects than the ice shape models molded from actual ice accretions. Perhaps this strange effect was caused by the jagged edge of the ice models causing turbulent boundary layers whereas the larger and more uniform S&C/LEWICE models caused intense vortices resulting in detached boundary layers. The effects of icing that would have the greatest effect on aircraft stability and control were shown in the changes in lift and hinge moment. For the clean Section 1 airfoil with $\delta_e = 0^\circ$ elevator deflection, $C_{l_{max}} = -1.23$ and $\alpha_{stall} = -17.8^\circ$. With the IRT1 ice shape attached, these values were reduced to $C_{l_{max}} = -0.73$ and $\alpha_{stall} = -10.5^\circ$ and with the IRT2 ice shape attached, these values were reduced to $C_{l_{max}} = -0.85$ and $\alpha_{stall} = -15.5^\circ$. Hinge moment data with ice shapes showed a definite change with the LEWICE ice shape producing the largest shift.

Velocity variations did not result in any noticeable differences with relatively small elevator deflections. Differences did show up once the elevator deflection reached the -20° position. Varying the airfoil Section did indeed have a significant effect on the aerodynamic coefficients. In general, the $C_{l_{max}}$ was slightly more negative for Section 2 than Section 1 while the difference in α_{stall} varied from zero to several degrees.

The results obtained from this wind tunnel test have given an effective set of data with which to begin an analysis of tailplane aerodynamics in icing conditions. The data will be incorporated into the DHC-6 Twin Otter database and used to quantify tailplane aerodynamics during simulated maneuvering flight. This understanding will be needed and fully utilized in the development of maneuvers to identify aircraft susceptible to tailplane stall in icing conditions.¹

II. Introduction

This wind tunnel test is the second test performed by The Ohio State University as part of the NASA, FAA, and OSU Tailplane Icing Program. The purpose of the program is to quantify the effect of tailplane icing on aircraft stability and control to aid in the development of a flight test procedure that will identify aircraft susceptible to tailplane icing. As a first step in this program, wind tunnel testing of the 2-Dimensional aerodynamics of the tailplane of the NASA Glenn Research Center Icing Research Aircraft, a DeHavilland DHC-6 Twin Otter (Figure 1), was undertaken. Pressure data from surface taps were acquired and integrated to obtain lift, drag, pitching moment, and hinge moment coefficients. It should be noted that during the test of 1994 (See Reference 1) pressure belt taps were applied to the surface of the model and used to collect pressure data, but evaluation and comparison of the data showed that the surface taps and the belt tap data were similar enough that the belt taps could be used on the flight vehicle to obtain valid pressures. The pressure belts were not used in the present tests.

Two additional leading edge ice shapes were evaluated for the present test, as well as selected repetition of tests from the first test series of ice shapes designated S&C and Lewice. The shape of the two new leading edge ice accretion models, designated IRT1 and IRT2 (Figure 5), were generated using the NASA IRT wind tunnel in an effort to provide actual ice accretion shape data before the next full scale flight test. The two new leading edge ice shapes are different from the previously tested S&C and Lewice (Figure 5) shapes in that they are actual casts of ice accreted on an airfoil; therefore having a relatively rough surface. The IRT1 shape is a model of an ice accretion collected for 22 minutes after de-icing boot failure whereas IRT2 is a model of ice after 15 minutes of accretion time with 3 minute cyclings of the de-icing boot.

For this additional testing, the experimental facility as well as the model used were the same as in the initial test of 1994. This also included the traversing wake pressure measurement system. However, in an effort to keep up with time constraints, the ScanivalvesTM were not used and a new system of pressure data acquisition by Pressure Systems Incorporated (PSI) was utilized. Using the PSI equipment reduced the average run time from 30 minutes to approximately 10 minutes. As noted earlier, the pressure belts were present on the model during the tests, but not used for surface pressure acquisition. It should be noted that the previous tests indicated that the tunnel speed of 100 kts did not significantly alter the aerodynamic coefficients; therefore the majority of data was taken at 60 knots.

At the start of the present test sequence, a few of the earlier test points were re-examined in order to check for repeatability. After successful comparison with the 1994 series, new test points were added to expand the first tests and the new ice shapes were installed and tested. Lastly, a carborundum grit simulating a light icing encounter was applied to the leading edge and data was taken for comparison to other configurations.

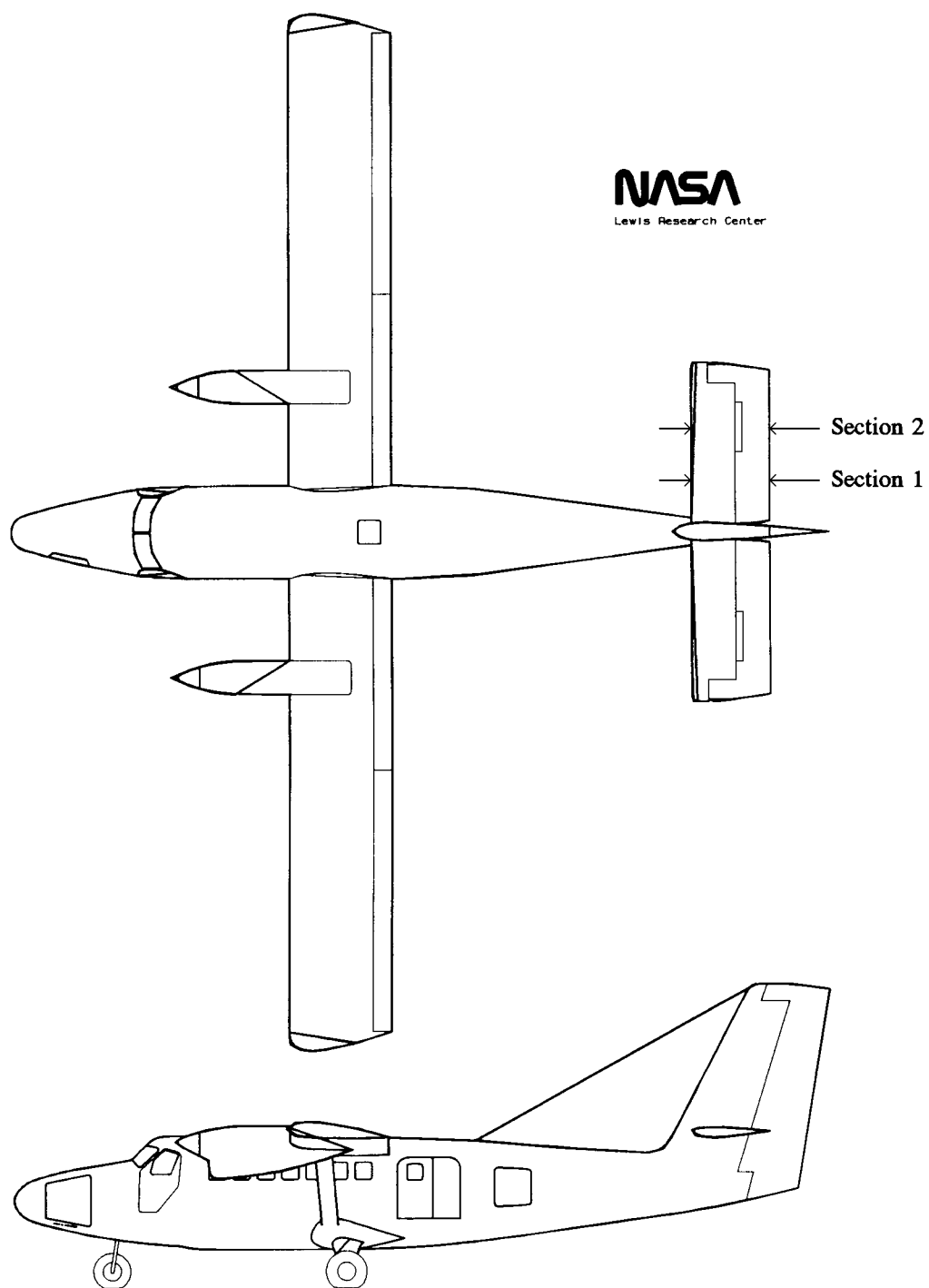


Figure 1 NASA Glenn Research Center Icing Research Aircraft.

III. Experimental Facility

The Aeronautical and Astronautical Research Laboratory Low Speed Wind Tunnel Facility (OSU LSWT) is a closed-loop circuit with a 7×10 ft. high speed test section, and a 14×16 ft. low speed test section. A 2000 Hp electric motor provides dynamic pressures up to 65 psf in the 7×10 ft. section (Figure 2). A sting balance mount allows models to be tested at angle-of-attack values ranging from -15 to +45 degrees, while the rotating tunnel floor has a range of -90 to +270 degrees.¹

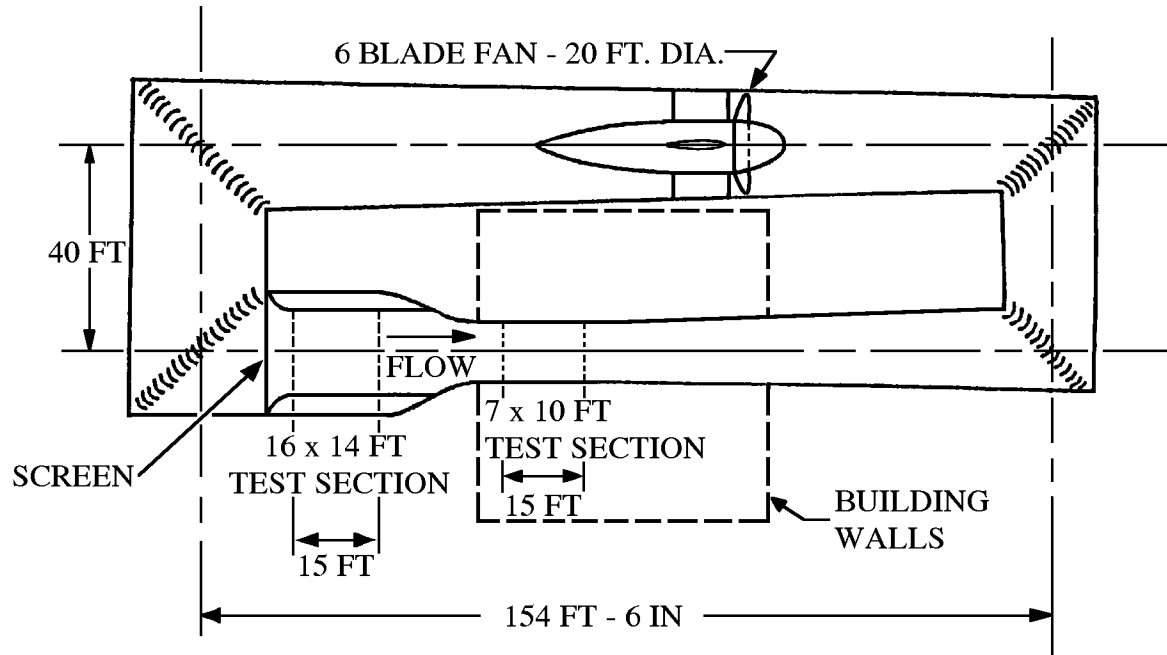


Figure 2 OSU Low Speed Wind Tunnel Facility

Tunnel speed is manually set based on average values obtained from two dedicated tunnel total pressure probes and two static pressure probes. A PC-class computer is used to control sting and mounting table angles, and wake probe sweep, as well as data acquisition tasks. Up to 14 data channels can be sampled. Signal conditioning and amplification are provided by individual rack mounted units.¹

Testing of 2-dimensional airfoils is conducted by installing a 7 ft. span model to fill the height of the high speed test section. The model is attached to the floor mounting table, which is then rotated to provide the desired angle-of-attack. Surface taps on the model are used to acquire pressure distributions, which are integrated to obtain model forces and coefficients. To determine momentum drag, wake survey probes are swept across the test section downstream of the model.¹

IV. Model Description

a) Airfoil Sections

The two airfoil sections tested are shown in Figure 3. The Section 1 airfoil is used on 70% of the tailplane span and is referred to as a clean airfoil when no ice shapes are attached to it. The tailplane area used by each section is indicated in the two-view aircraft drawing (Figure 1). Drawings of the four ice shapes are shown in Figure 5. Some minor smoothing of the lofted airfoil shape was required; a 0.020 inch "bump" at the lower leading edge was removed, and a straight line contour from the elevator main spar to the trailing edge was assumed.¹

The primary factors in the model design were to provide a smooth aerodynamic surface while allowing flexibility in model configuration and low fabrication costs. A highly stiff design was also desired, to maintain model shape under load. The chosen model design consisted of airfoil sections machined in Machineable Plastic, also known as REN material, supported by metal tubing spars and aluminum ribs. This allowed the utilization of CNC machining to fabricate the airfoil shape with high accuracy.¹

A schematic of the model is shown in Figure 4. The 20 inch span Machineable Plastic sections were supported by two internal metal tubing spars through each of the stabilizer and elevator sections. These sections transmitted their loads to the ribs through pins. The ribs contained keyways for keys mounted on the stabilizer spar tubes to provide stiffness under model moment loadings. Three ribs and two endplates structurally connected the spar tubes of the stabilizer to the forward spar tube of the elevator. The ribs of the elevator overlapped those of the stabilizer, to form a hinge around the forward elevator spar tube. End ribs on the elevator provided attach points to the endplates, which were used for changing the elevator deflection angle. The endplates contained rods to attach the model to the tunnel yaw table floor supports, and to a ceiling pivot. The model was mounted to the yaw table such that the table center of rotation was at 28% model chord.¹

Removable plug sections were used to create the two airfoil sections tested. The stabilizer section consisted of the airfoil for Section 1, with an aft extension plug used to create the Section 2 stabilizer airfoil. The elevator section consisted of the Section 2 airfoil with leading edge plugs to create the Section 1 airfoil. Figures 6 through 10 show the model as installed in the tunnel.¹

Tap locations were chosen to provide high resolution where pressure gradients were large, and low resolution elsewhere to minimize the total number of taps. Taps were labeled starting with #1 on the leading edge of the stabilizer and ending with #86 on the elevator trailing edge. Odd numbered taps were located on the lower, or suction, side of the airfoil as installed in the aircraft, with even numbers on the upper, or pressure, side, except at the boat-tail ends. The tap locations of the ice shapes covered and replaced some of those of the clean airfoil. The final tap locations for each airfoil section and ice shape configuration are listed in Appendix A, which also shows a graphic of their positions on the airfoils.¹

Surface taps were installed in-house prior to the completion of the section assembly. Taps were located on a 12 inch airfoil section using a Bridgeport milling machine with digital distance readout. Tap locations were determined relative to a coordinate system specifically chosen to be readily indicated using known positions on the section. Once the locations were marked along the section moldline, 0.0625 inch diameter holes were drilled normal to the surface 0.5 inches below one edge. Mating holes were then drilled vertically into the milled out end of the section. Stainless steel tubing was then fitted to these mating holes and routed along the section end and through tubing passageway holes. The tubing was glued and sealed to the mating hole using plumbers paste.

With the tubing completed, the milled out end was filled and glued to a mating 8 inch section to complete the 20 inch section. Strip-a-tube tubing was then attached to the stainless steel tubing and routed through the passageways in each section to connect the surface taps to the Scanivalve™ ports. The tubing length was approximately 15 ft.¹

The belt was installed by first milling a slot into the pressure side of the stabilizer and elevator. Double sided tape and epoxy were then used to secure the belts to the section. The free ends of the belts were then routed through the slot and into the tubing passageways.¹

b) Ice Shapes

The representative ice shapes (See Figure 5) were named S&C, LEWICE, IRT1, and IRT2. The S&C ice shape has been used in several stability and control programs on the Twin Otter. This ice shape was determined using a combination of in-flight photographs of icing on the Twin Otter's tailplane, and the ADS-4 report "Engineering Summary of Airframe Icing Technical Data", by General Dynamics/Convair. The LEWICE ice shape was predicted using the LEWICE 1.3 computer program. The specific input conditions were: velocity = 120 knots, liquid water content = 0.5 g/m³, median volumetric diameter = 20μm, icing time = 45 minutes, $\alpha = 0^\circ$, total temperature = -4°C. The ice shape was determined in five equal time steps. Each step consisted of a 9 minute accretion time, a redefining of the iced airfoil geometry, and a recalculation of the airflow over the new geometry. The 45 minute accretion time was chosen to be conservative while aligning with the FAA requirement of demonstrating capability with 45 minute accretion time on an unprotected surface¹.

The IRT1 and IRT2 ice shapes are models of actual leading edge ice accretion. The following method of manufacture was provided by Thomas Ratvasky of the NASA Glenn Research Center. First, ice is allowed to build up on the leading edge of an airfoil model in the NASA Glenn Icing Research wind tunnel. The ice located on either side of the area of interest is cleaned off of the model. Then a mold box with the bottom panel cut out in the shape of the leading edge is fitted against the model, forming an enclosed area surrounding the ice of interest and the leading edge of the airfoil model. The box is then filled with a silicon-based molding material (RTV 3110) that cures at below freezing temperatures. The molding material fills the box and surrounds the ice shape filling in all of the intricate cavities. (For more details about the tunnel conditions during the creation of IRT1 and IRT2, please see Appendix F.)

Once the molding material has cured, the mold box is removed from the airfoil model and the mold is extracted from the box. The mold has the shape of the box with a cavity that has the impression of the ice and leading edge of the model.

Producing the mold is only the first of two steps in creating a finished ice shape. After the ice shaped mold is created, a plug of the airfoils' leading edge is made and inserted into the ice shaped mold leaving a small cavity between the leading edge and the mold. A polyurethane material is mixed and poured into the cavity where it fills all of the ridges and bumps left in the ice mold. After curing, the casting is removed from the mold and plug. Because the properties of this type of mold are driven by the environment in the Icing Research Tunnel, they do not always have the resilience to separate nicely from the casting. In fact, some of the original mold may even tear off with the casting. These torn off pieces are cleaned off of the casting, which serves as the master casting.

The master casting is then used to make another mold using a different mold material that allows for a cleaner separation between mold and casting. This secondary mold is then used in the same manner described above to mass produce other castings. For this particular wind tunnel test, NASA made enough castings to span the airfoil model inside the 7×10 Low Speed Wind Tunnel. For the full scale flight test, there will be enough segments produced to fit on the entire tailspan (~20ft) of the DHC-6 Twin Otter.

Because the installed ice shapes covered up many of the leading edge pressure taps, a method was devised to bring the pressure taps up through the ice shapes. This involved drilling new pressure taps and in some cases, simply attaching new tubing and rerouting the pressure lines. For the pressure taps in the vicinity of the de-icing boot, large holes were drilled through the ice shapes above where the taps were located. Wires were inserted through the large holes and into the pressure tap holes. Finally, the large holes were filled with body putty and sanded accordingly; the wires were then removed (See Figure 10).

Lastly, a carborundum grit was applied to the leading edge to simulate insect debris on the leading edge. A template with a repeating “random” pattern of holes was laid over 6 inch wide double sided tape. The carborundum grit, type #30, was sprinkled onto the template with some of it sinking through the drilled holes and sticking to the double sided tape. This tape was then applied to the leading edge starting at approximately the stagnation line and laid down towards the trailing edge going over both the top and the bottom of the airfoil. A photograph of the grit tape is shown in Figure 11. A schematic of the applied grit tape is shown in Figure 12.

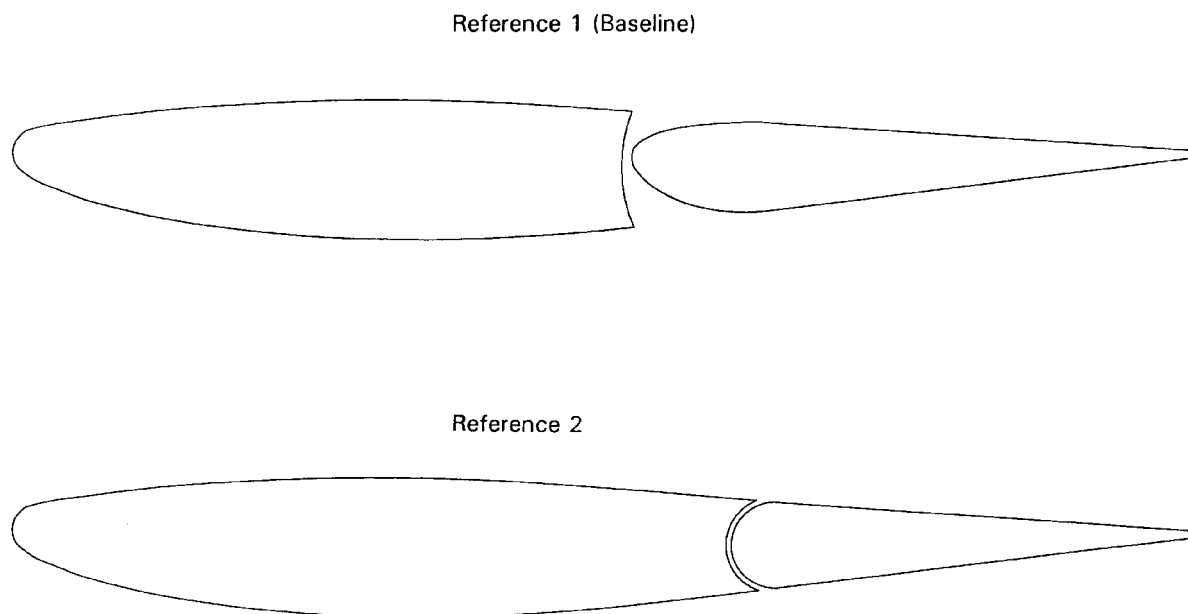


Figure 3 Section 1 and Section 2 airfoil profiles.

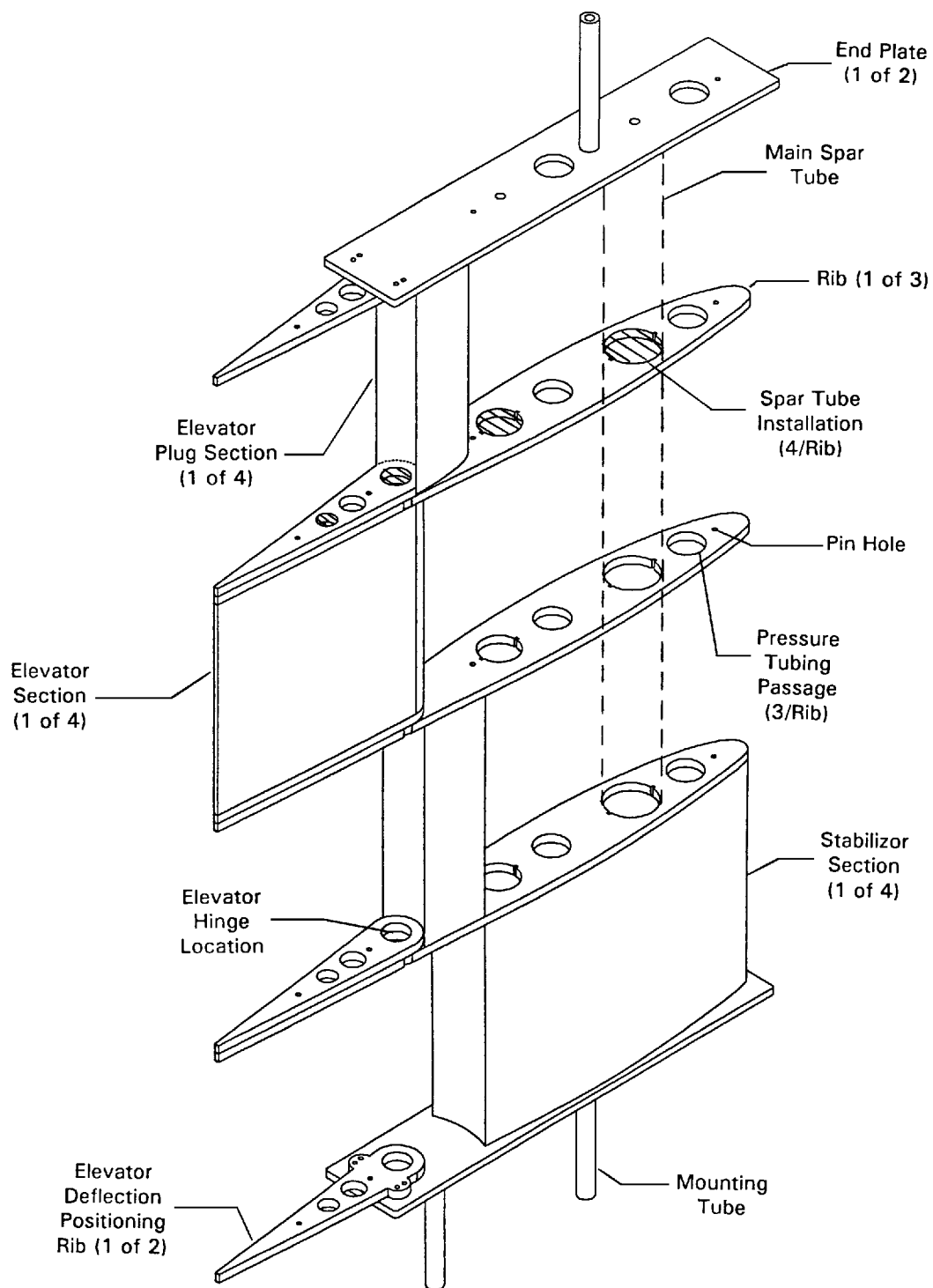


Figure 4 DHC-6 wind tunnel model schematic.

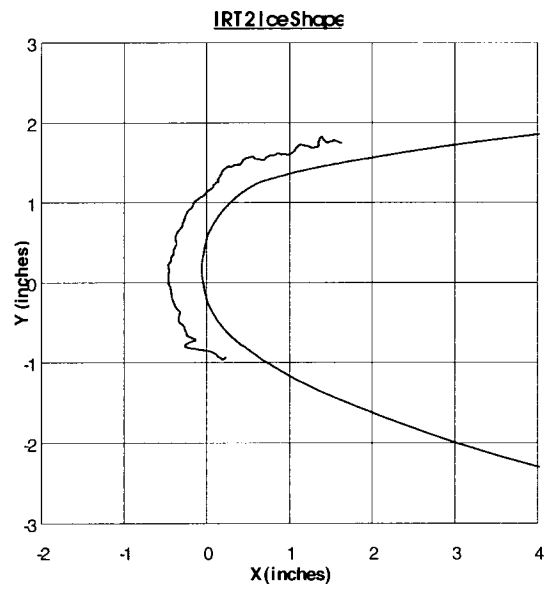
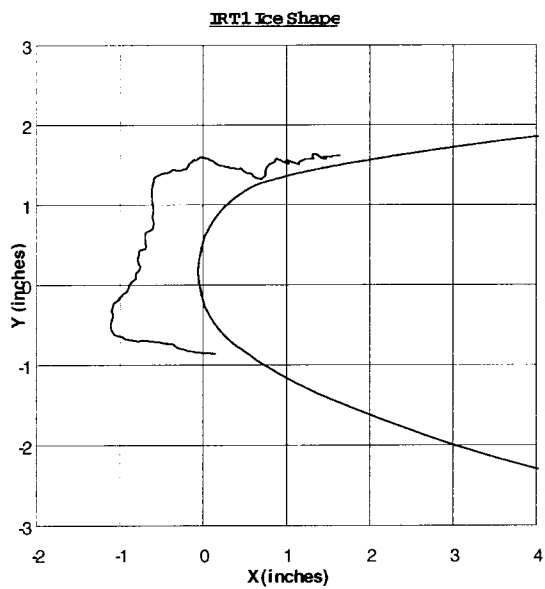
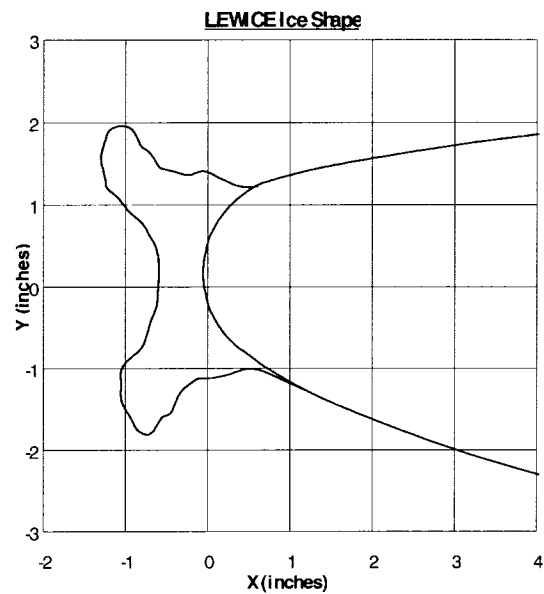
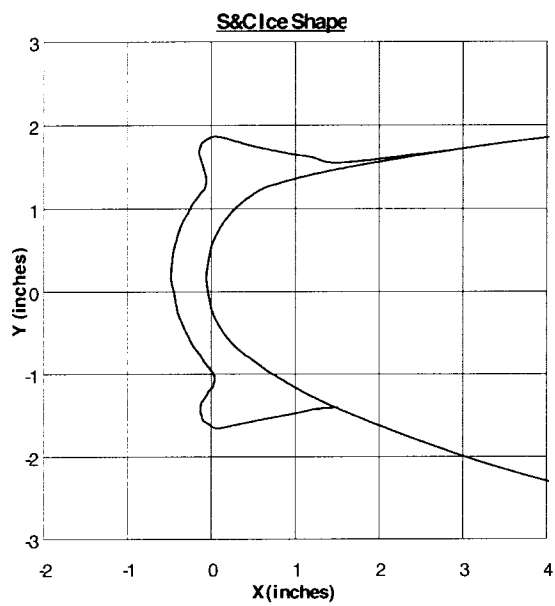


Figure 5 Ice shape model profiles.

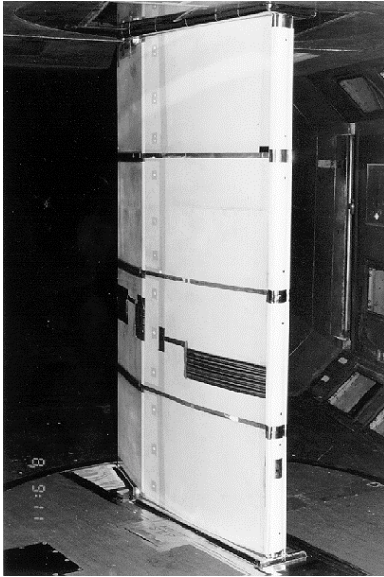


Figure 6 S&C ice shape installed.

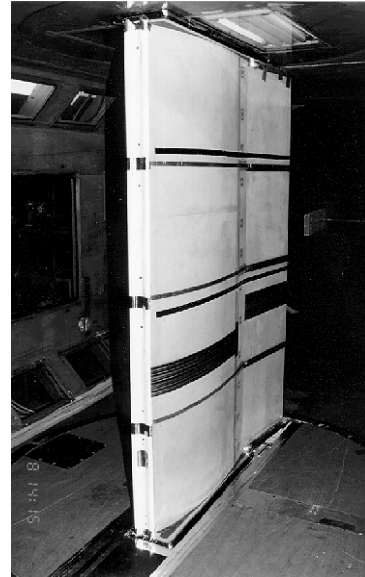


Figure 7 LEWICE ice shape installed.



Figure 8 IRT1 ice shape installed.



Figure 9 IRT2 ice shape installed.

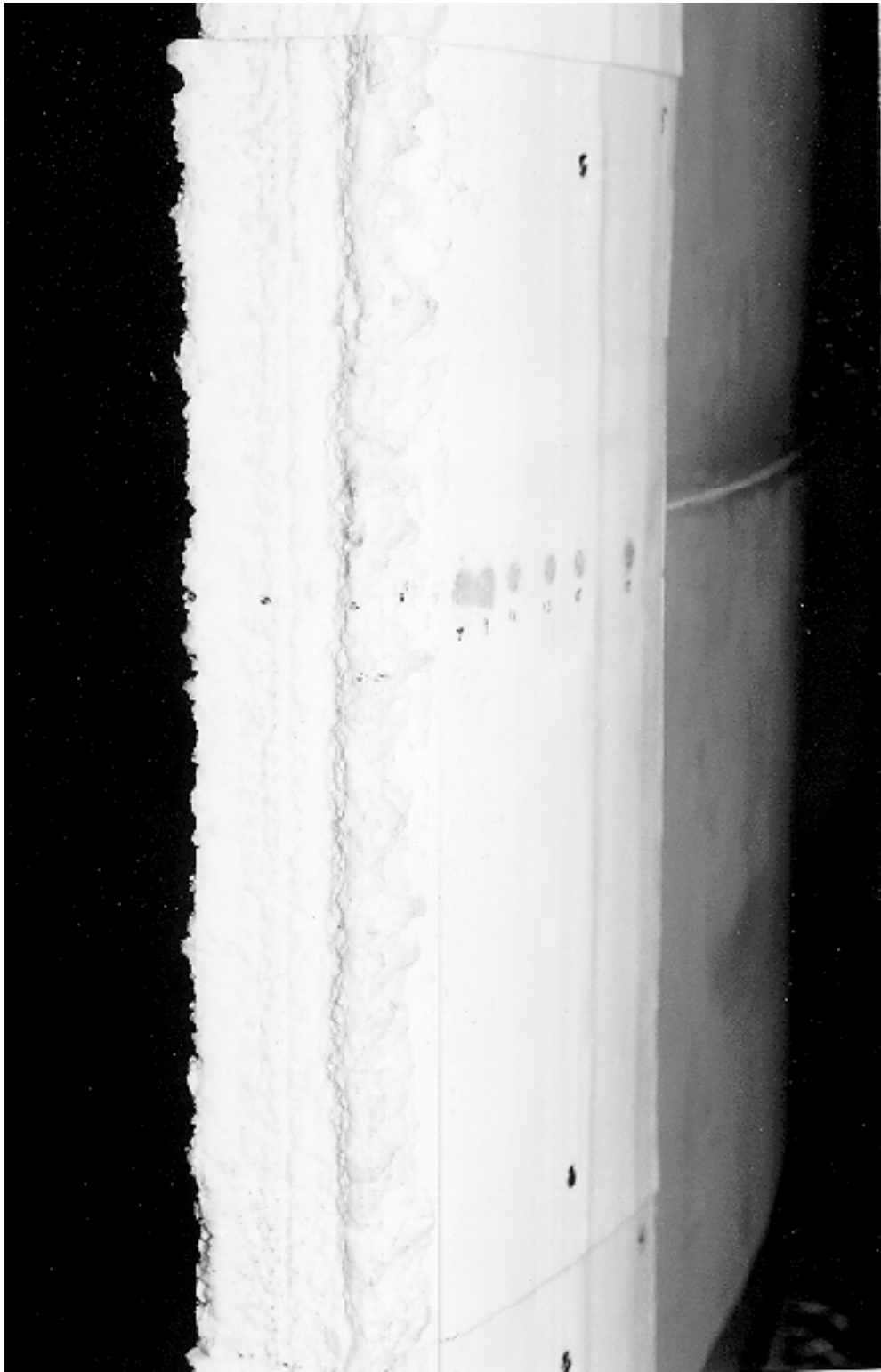


Figure 10 IRT1 ice shape installed with pressure taps in view.

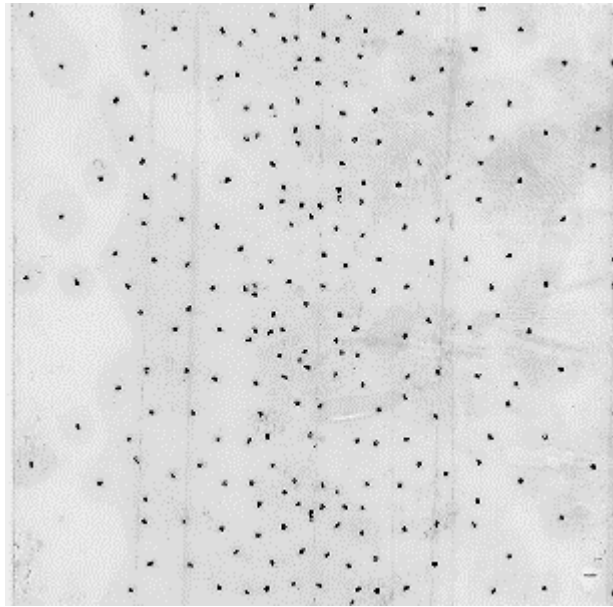


Figure 11 Grit tape with grit applied. Shown actual size.

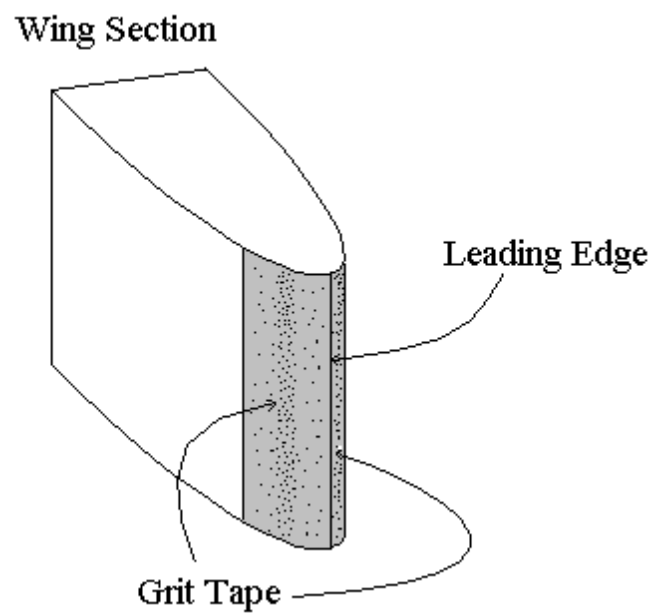


Figure 12 Schematic of the grit tape placement.

V. Data Acquisition

In an effort to reduce testing time, the previously used ScanivalvesTM were not utilized during this sequence of wind tunnel runs. Instead, a Pressure Systems IncorporatedTM (PSI) data scanning system was used. This particular setup included a 780B Data Acquisition and Control Unit, a 780B Pressure Calibration Unit, an 81-IFC scanning module interface, one 32-port 5-psid pressure scanning module and two 2.5-psid 32-port pressure scanning modules. With the three pressure modules, a maximum of 96 individual pressures could be measured. The use of the PSITM gear made it possible to complete a test run of 16 points in about 10 minutes whereas the ScanivalvesTM would have taken approximately 30 minutes.

The wake measurement system consisted of pressure probes mounted to a 16 ft. length of aerodynamic tubing which spanned the test section horizontally. The tubing was supported by roller guides located at each wall exterior and one roller guide mounted on a vertical section of aerodynamic tubing located at approximately 1/3 of the of the tunnel width from the port wall. Three sets of total and static pressure probes were attached to the aerodynamic tubing. These probes were 4 inches apart with 32 inches between sets to allow some overlap during the 36 inch sweep across the test section. An individual probe was used for each total and static pressure to allow measurements to be made at a constant tunnel cross-section location. Both total and static wake probe pressures were measured with 2.5 psi differential transducers.¹

Tunnel conditions were measured using dedicated 2.0 psi differential transducers for pitot pressures while 0.5 psi differential transducers were used for the static pressures. All differential transducers were vented to the atmosphere with atmospheric pressure determined from a sensitive altimeter.¹

A 386 class PC controlled all data gathering and data reduction operations with only tunnel airspeed being manually controlled. Angle-of-attack positioning, operation of the ScanivalvesTM, operation of the wake probe sweep, and recording of all raw data performed by the run program.¹

VI. Test Procedure

Appendix B contains a run-log for this test. Repeatability runs of the Baseline configuration of 60 kts were taken at $\delta_e = 14.2^\circ, 0.0^\circ, -10.0^\circ$, and -26.6° . In addition, the last data point of each polar sweep was taken at $\alpha = 0.0^\circ$ as a repeatability check.

The daily test procedure consisted of first adjusting all signal conditioners and amplifiers. Then the atmospheric pressure was determined from a sensitive altimeter and recorded on paper for future insertion into the data acquisition program. The run software was set for the current test configuration and a no-wind tare was taken. The run program was then started, which positioned the model to the first angle-of-attack of the sweep (usually $+4^\circ$). The tunnel fan was then started and manually set to the desired velocity as displayed by the run program. Once this velocity was stabilized, the angle-of-attack sweep mode was engaged. The run program then positioned the model and took data for all desired angle-of-attack points. A typical angle-of-attack sweep of 10 points (angles-of-attack) took approximately 10 minutes to complete. If a wake probe was desired, it occurred after pressure tap data were taken at each angle-of-attack. This sweep added an extra 2 minutes to the time taken for each individual test point. Because of this, only a limited number of wake probe sweeps were accomplished. An attempt was made between each test point to set the tunnel velocity at 60 kts; reason being that at high angles-of-attack, the rotating model created more blockage slowing the airspeed.

With the angle-of-attack sweep completed, any desired post-run note was entered into the run program, and the raw data were saved to the hard disk. The raw data were the final result generated by the run program. The raw data file included the output voltages of all transducers, and the tap location and calibration data. This method of data storage allowed a run to be modified post-test if errors in the setup or tap-file were discovered after testing was completed.

Limited tuft flow visualization was also performed. Upper and a lower rows of tufts consisting of white string were attached to the model with a black electrical tape.

VII. Data Reduction

Aerodynamic coefficient data were obtained by integrating the pressure coefficient distributions of the stabilizer and elevator separately. A typical pressure distribution is shown in Figure 13. This integration was accomplished by applying the averaged pressure of adjacent taps to the area between them. When summed, these values gave coefficients defined relative to the local element coordinate system. These local coefficients were then converted to a lift and drag contribution by the appropriate axis transformation. Moment was obtained similarly using moment arms of the distance from a reference center to the center of each integration area.¹

Wake data was only collected for a limited number of test runs. In order to adjust the pressure drag coefficient to include some wake drag data, a weighted-average bias value was determined by comparing the wake and pressure drag coefficients at $\alpha = 0^\circ$ and $\delta_e = 0^\circ$ for each section and ice shape. These bias values were then applied to all of the pressure drag coefficients obtained with the same section and ice shape configuration.

Once the aerodynamic coefficients were obtained, a solid wall correction was applied. The formulas used to calculate the corrected data are shown in Appendix C. An example of the typical magnitude of the corrections is given in Figure 14 which shows corrected and uncorrected data for an ice shape run. A buoyancy term was not included in the corrections which is used in Ref. 2 as a C_D correction. Ref. 2 implies that a buoyancy correction is valid only for large elements of an aircraft configuration and is not significant for airfoils alone.¹

In addition to the aerodynamic coefficients, the reduction program also calculated other important data. Other output files generated contained uncorrected, corrected, wake drag, and wall static pressure coefficients. Appendix D contains a description of the file name and data structure conventions of these output files.

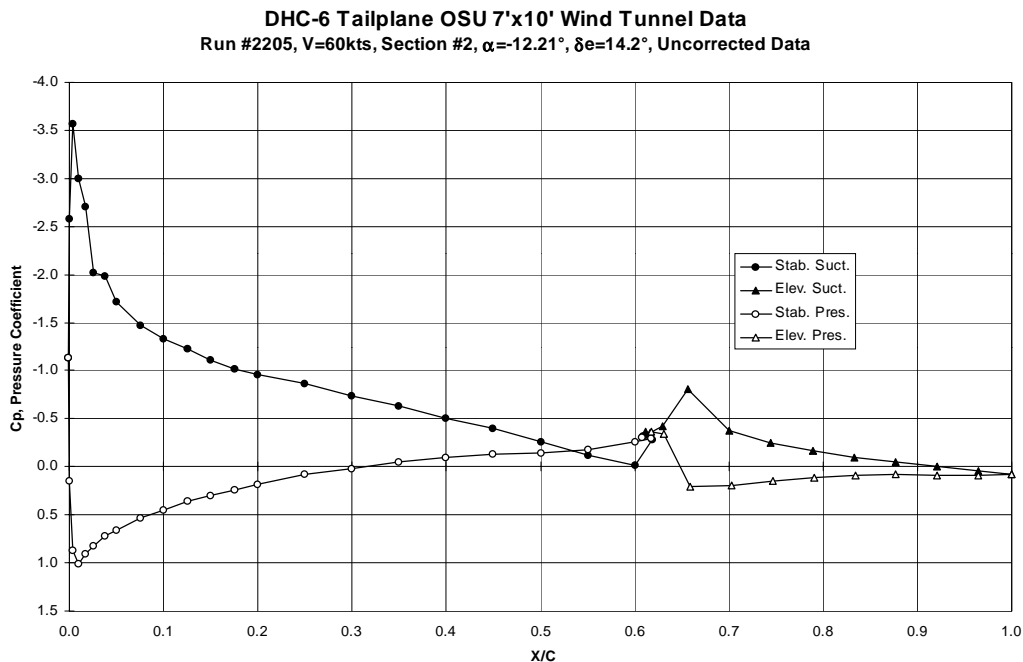


Figure 13 Example of a typical pressure distribution.

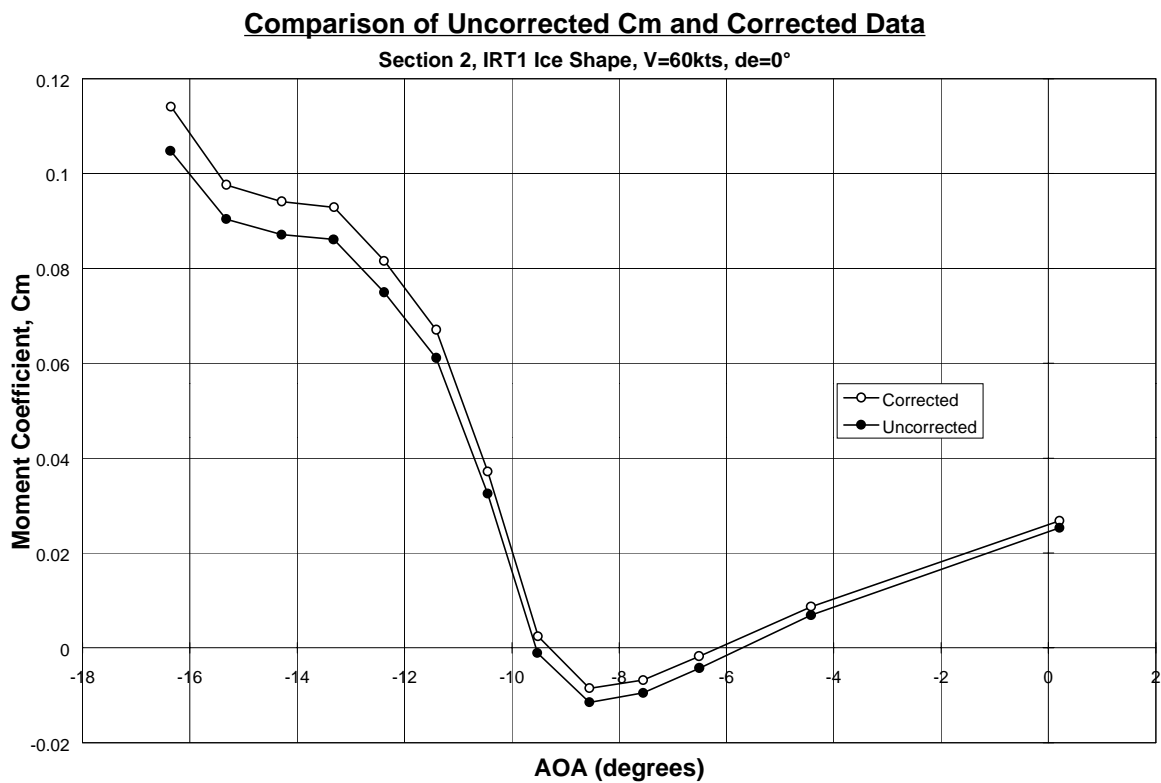
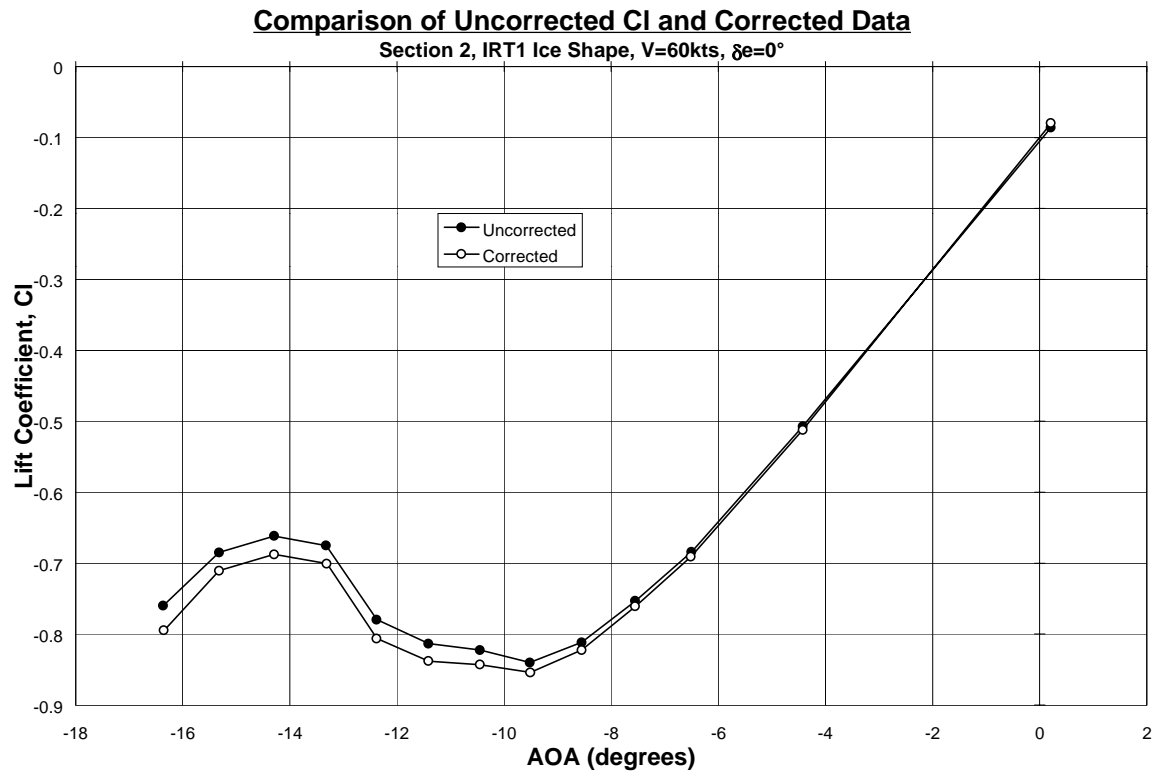


Figure 14 Example of data reduction correction magnitudes.

VIII. Results and Discussion

The purpose of this test was to quantify the aerodynamic effects of various ice shapes on the twin Otter Tailplane. This quantification was sought relative to the tailplane stall phenomenon. The two most important phenomena were therefore lift and hinge moment. These subjects are discussed in the following section. Appendix E contains a complete data presentation of all test results of C_L , C_D , C_M , and C_H conveniently located on a single page for each.

All data are presented with the tailplane as installed on the aircraft using an aircraft reference system; therefore the airfoil appears to be upside down. The values of interest are those occurring at negative angle-of-attack when the tailplane is generating negative lift, or positive down-force. Other sign conventions worth noting are; angle-of-attack positive with stabilizer leading edge up, moment and hinge moment positive when nose up, and elevator deflection positive with the trailing edge down. Figure 15 presents a schematic describing the axis system and sign conventions.

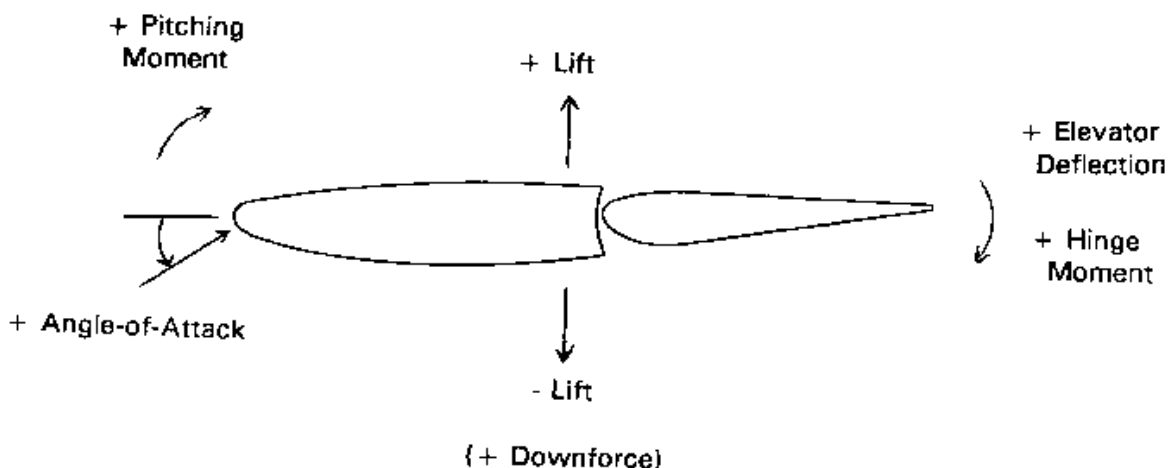


Figure 15 Schematic of axis systems and sign conventions.

a) Ice Shape Effects

The lift characteristics with zero elevator deflection are shown in Figure 16. It is clearly shown that the ice shapes reduce the $C_{l_{max}}$ from that of the clean airfoil $C_{l_{max}}$. Figure 16 also shows how the stalled angle-of-attack, α_{stall} , is significantly reduced by the ice shapes. Specifically, the negative $C_{l_{max}}$ was reduced from -1.4 for the clean airfoil to approximately -0.7 for the LEWICE ice shape configuration. The α_{stall} was also reduced from -16° to approximately -8° for similar configurations. Application of leading edge grit (the inclusion of grit data governed the use of this section 2 plot versus a section 1 plot) only affects the α_{stall} by a few degrees ($\sim 1^\circ$ to 2°) and reduces (makes more positive) the $C_{l_{max}}$ by about 0.1 . The hinge moment characteristics are shown in Figure 17. The Lewice and S&C ice shapes tend to have a more drastic affect on the hinge moment than the actual ice molds.

As may be expected, various elevator deflections cause the α_{stall} to either increase or decrease. This phenomenon is shown in Figure 18. Note that negative elevator deflections cause the α_{stall} to become more negative whereas positive deflections cause the α_{stall} to grow more negative; much like how ailerons would affect an inverted wing. The exact opposite occurs with the $C_{l_{\text{max}}}$ term. With the IRT1 ice shape installed (Fig. 18) and with $\delta_e = -10^\circ$, $C_{l_{\text{max}}} = -0.95$ and $\alpha_{\text{stall}} = -8.5^\circ$, whereas at $\delta_e = +10^\circ$, $C_{l_{\text{max}}} = -0.5$ and $\alpha_{\text{stall}} = -12.5^\circ$. These trends continue, although different in magnitude, even with large elevator deflections and occur with both Sections (Figs 19, 20, and 21).

A similar effect happens with the hinge moment coefficient, C_H (Fig. 22). A negative elevator deflection tends to raise the curve while positive deflections tend to lower the curve. The effect is even more noticeable with large elevator deflections (Fig. 23). With small deflections such as -10° and $+10^\circ$, the difference between the curves is approximately $\Delta C_H = 0.1$. At large deflections, though, the difference approaches $\Delta C_H = 0.13$. This trend is continued and magnified with the use of Section 2 (Figs. 24 and 25).

b) Velocity Effects

The characteristic velocity effects are shown in Figures 26 through 29. These plots reflect the velocity effect on the IRT1 and IRT2 ice shapes along with the various sections. Figure 26, which shows the lift coefficient vs. angle-of-attack, demonstrates that as the elevator deflection grows more positive, the $C_{l_{\text{max}}}$ becomes less negative and α_{stall} becomes more negative. At 60kts, with $\delta_e = -20^\circ$ there is a notable increase (more positive) in negative C_L from approximately 3° to -7° at a lower speed. With the IRT2 ice shape installed, the data (Fig. 28) show that there is even smaller or nonexistent difference between the high and low speed values.

c) Repeatability

In order to verify that comparison between the data of 1994 and 1996 would be valid, several repeat test runs were accomplished. These were carried out for both Sections 1 and 2 with elevator deflections of 14.2° , 0.0° , and -20.0° . The lift coefficients (Figs. 30 and 32) repeated relatively well except for the large deflection of -20.0° where the 1996 data showed a similar $C_{l_{\text{max}}}$, but a more negative α_{stall} . The hinge moment data (Figs. 31 and 33) also showed such a general trend. The 1996 data matched fairly well except for the large deflection of -20.0° .

d) Section Effects

The Section 2 airfoil was tested at a velocity of 60 kts with $\delta_e = 14.2^\circ$, 0.0° , and -20.0° . Lift and hinge moment coefficient plots are shown in Figures 34 through 43. A notable characteristic of the Section 2 airfoil data is the general decrease (more negative) C_L . For a δ_e of 0.0° and a clean airfoil, the difference between the $C_{l_{\text{max}}}$'s is approximately 0.15. This nominal difference is also seen with most of the other ice shapes, except for IRT2 (Figs 34 through 38). With the hinge moment data, there is also a difference between Section 1 and Section 2. Once again, the biggest differences exist for the elevator deflection of -20° (Figs. 39 through 43).

As the elevator deflection grew more negative, the hinge moment coefficient for Section 2 became more positive than the Section 1 hinge moment coefficient. For the case of the elevator deflection becoming more positive, the hinge moment coefficient for Section 2 would become more negative than that of Section 1. This trend continued throughout the hinge moment coefficient plots (Figs. 39 through 43).

DHC-6 Tailplane OSU 7X10 Wind Tunnel Data
Ice Shape Effects, $V=60$ kts, Section 2, $\delta e=0.0$

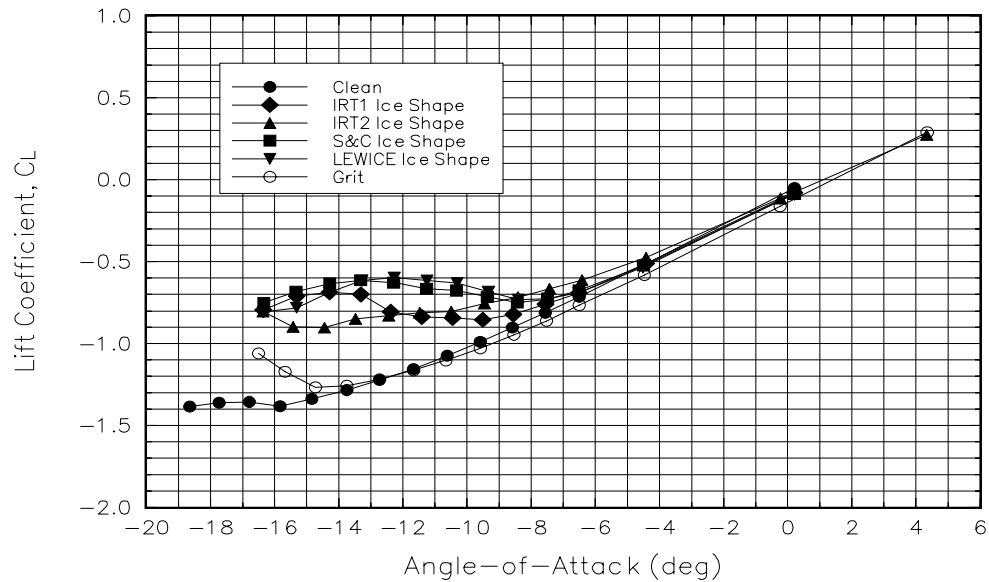


Figure 16 Ice shape effects, lift coefficients.

DHC-6 Tailplane OSU 7X10 Wind Tunnel Data
Ice Shape Effects, $V=60$ kts, Section 2, $\delta e=0.0$

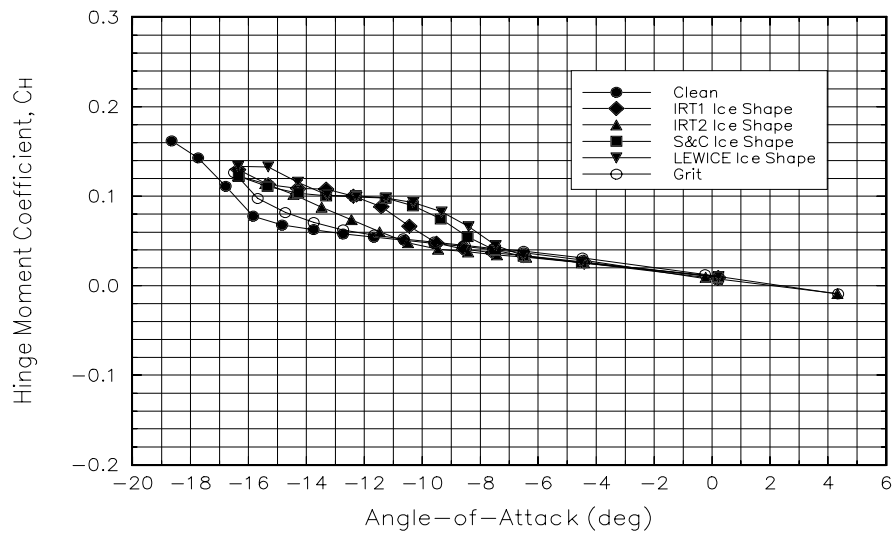


Figure 17 Ice shape effects, hinge moment coefficients.

DHC-6 Tailplane OSU 7X10 Wind Tunnel Data
Ice Shape Effects, V=60 kts, Section 1, Min Deflections

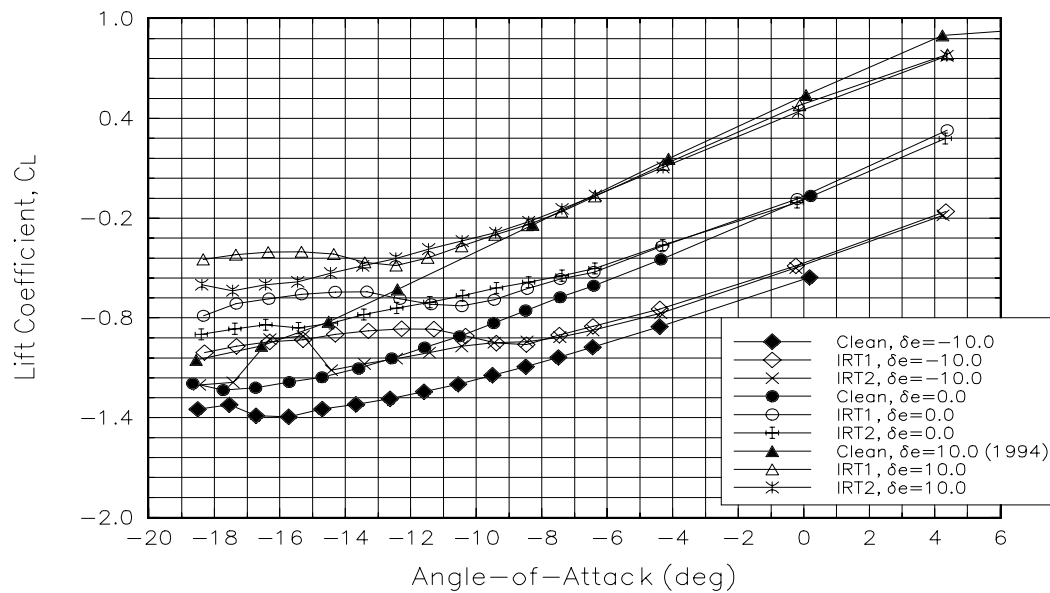


Figure 18 Ice shape effects, lift coefficient at small elevator deflections. Section 1.

DHC-6 Tailplane OSU 7X10 Wind Tunnel Data
Ice Shape Effects, V=60 kts, Section 1, Large Deflections

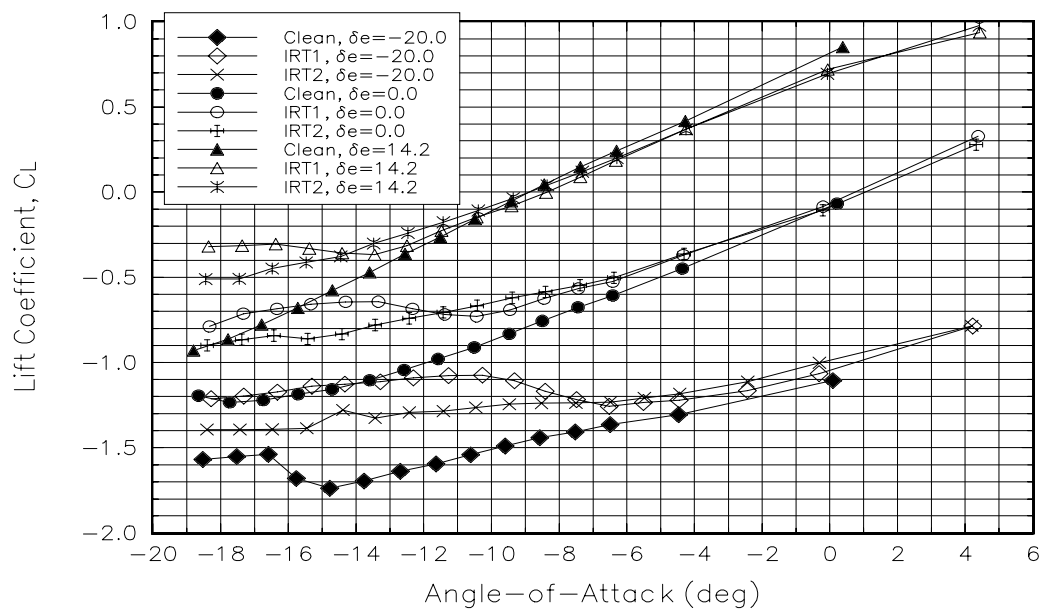


Figure 19 Ice shape effects, lift coefficient at large elevator deflections. Section 1.

DHC-6 Tailplane OSU 7X10 Wind Tunnel Data
Ice Shape Effects, V=60 kts, Section 2, Min Deflections

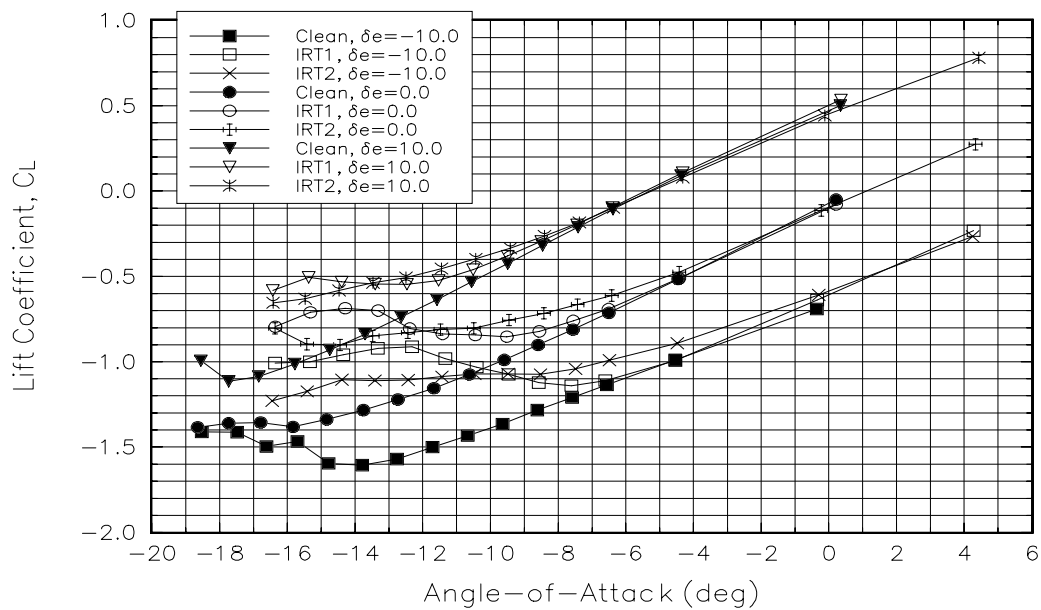


Figure 20 Ice shape effects, lift coefficient at small elevator deflections. Section 2.

DHC-6 Tailplane OSU 7X10 Wind Tunnel Data
Ice Shape Effects, V=60 kts, Section 2, Large Deflections

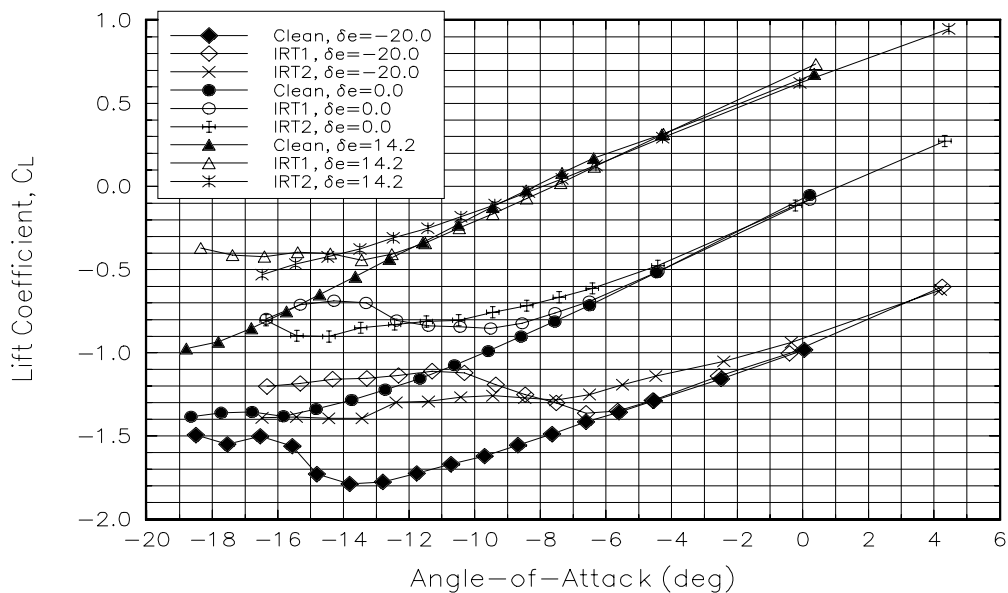


Figure 21 Ice shape effects, lift coefficient at large elevator deflections. Section 2.

DHC-6 Tailplane OSU 7X10 Wind Tunnel Data
Ice Shape Effects, V=60 kts, Section 1, Min Deflections

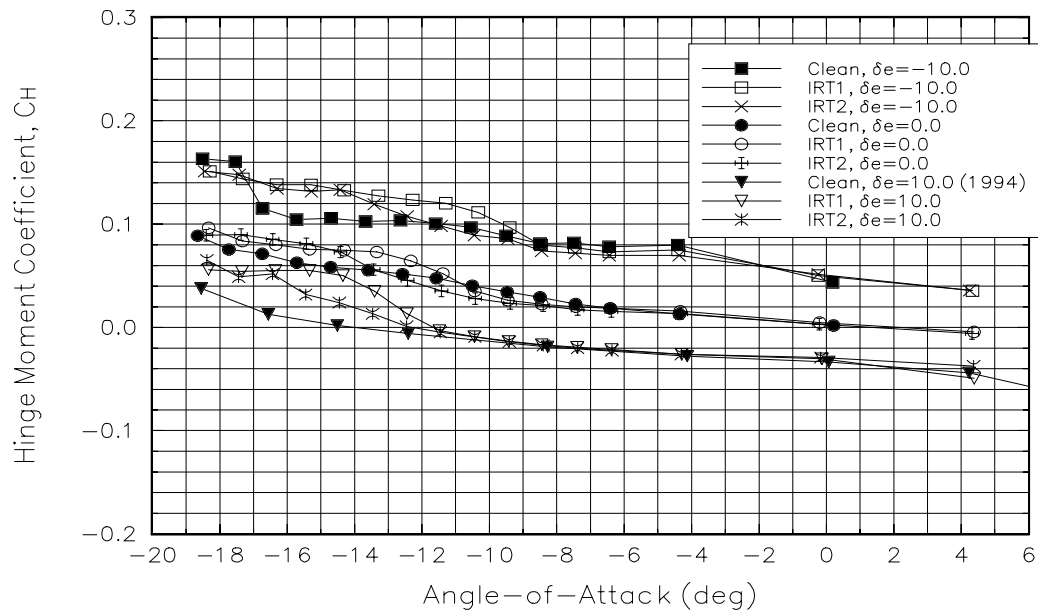


Figure 22 Ice shape effects, hinge moment coefficient at small elevator deflections. Section 1.

DHC-6 Tailplane OSU 7X10 Wind Tunnel Data
Ice Shape Effects, V=60 kts, Section 1, Large Deflections

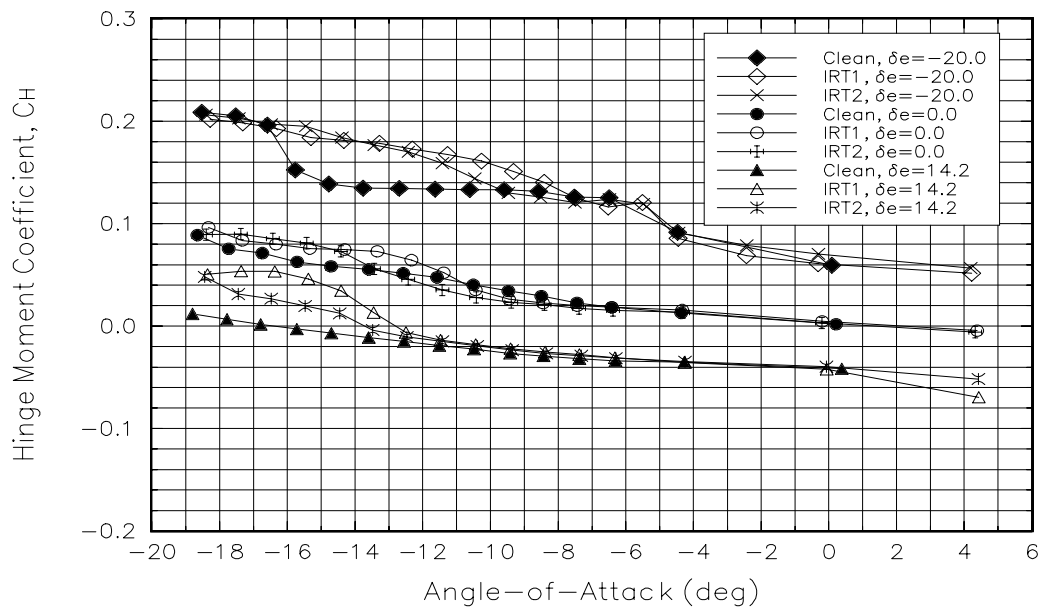


Figure 23 Ice shape effects, hinge moment coefficient at large elevator deflections. Section 1.

DHC-6 Tailplane OSU 7X10 Wind Tunnel Data
Ice Shape Effects, V=60 kts, Section 2, Min Deflections

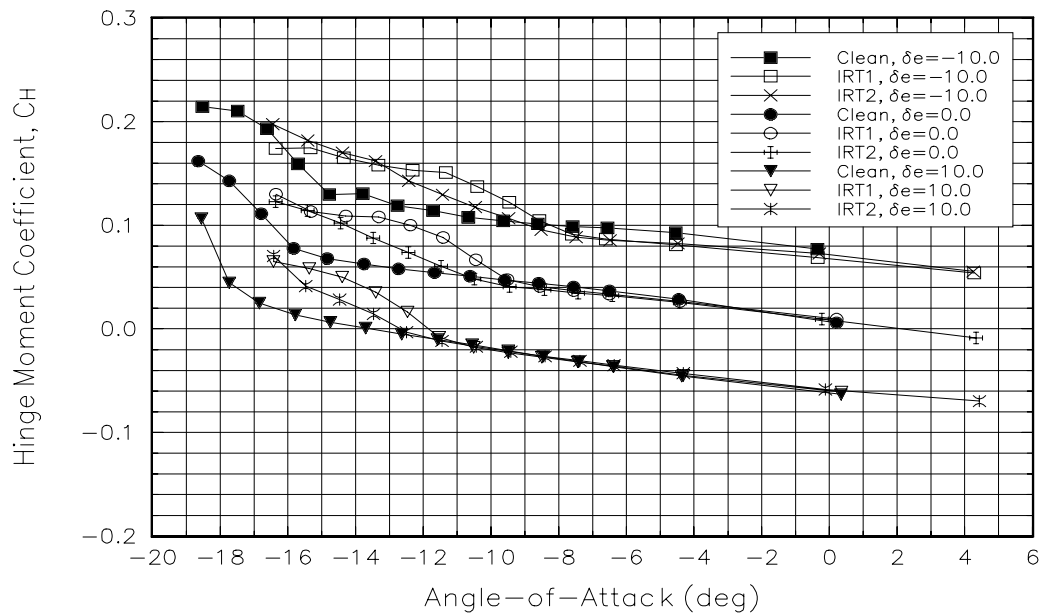


Figure 24 Ice shape effects, hinge moment coefficient at small elevator deflections. Section 2.

DHC-6 Tailplane OSU 7X10 Wind Tunnel Data
Ice Shape Effects, V=60 kts, Section 2, Large Deflections

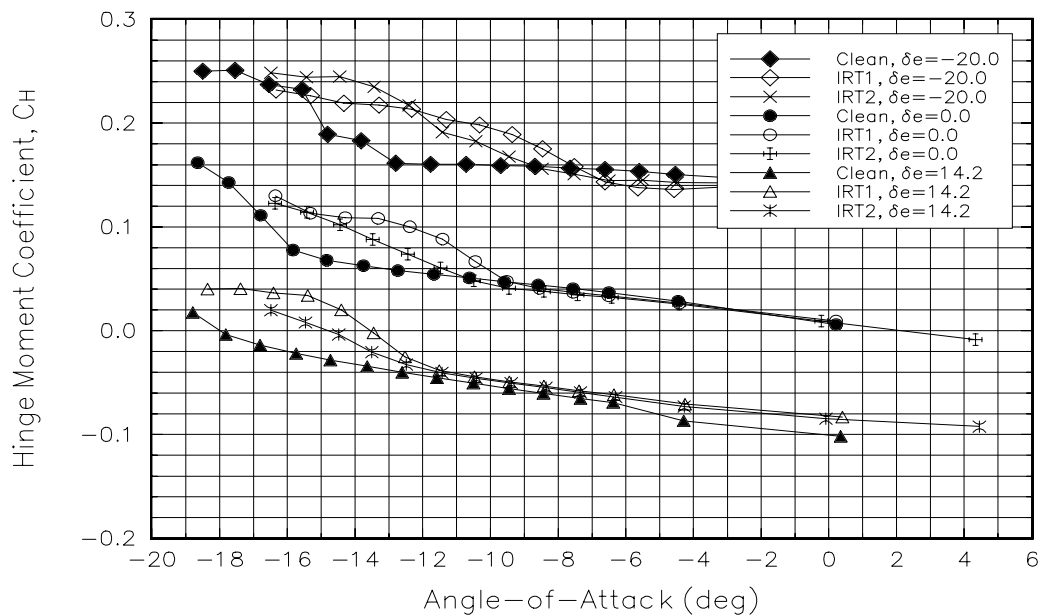


Figure 25 Ice shape effects, hinge moment coefficient at large elevator deflections. Section 2.

DHC-6 Tailplane OSU 7X10 Wind Tunnel Data
Velocity Effects, IRT1 Ice Shape, Section 1, Large δe 's

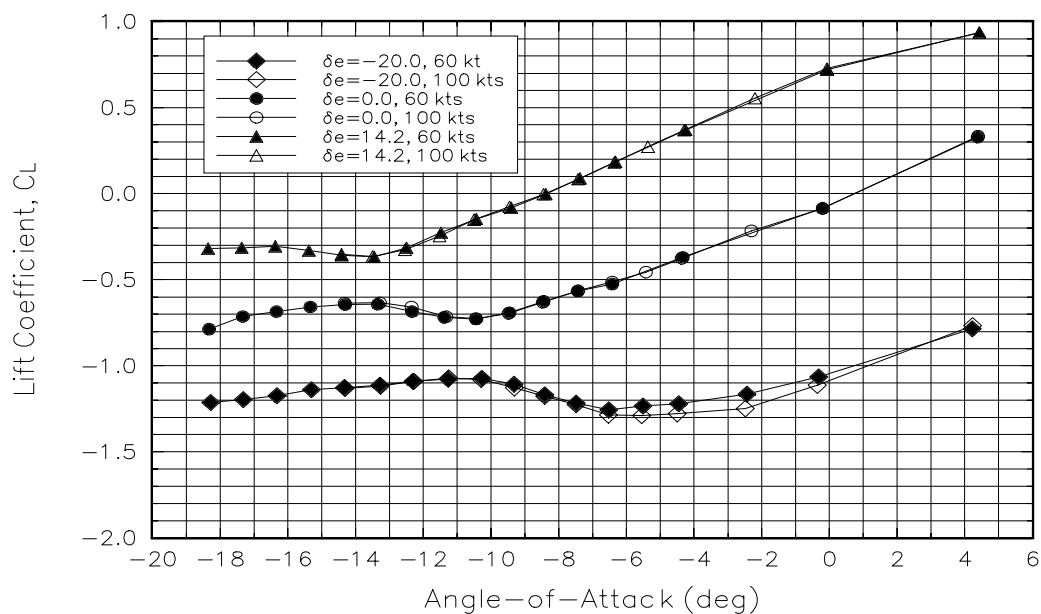


Figure 26 Velocity effects, lift coefficient at large elevator deflections. Section 1. IRT1.

DHC-6 Tailplane OSU 7X10 Wind Tunnel Data
Velocity Effects, IRT1 Ice Shape, Section 1, Large δe 's

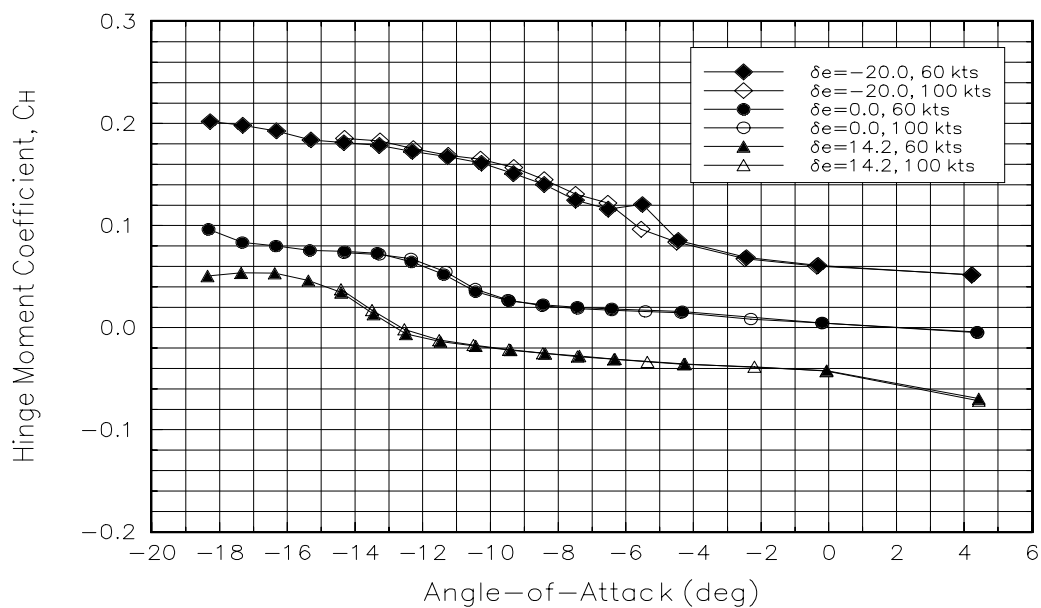


Figure 27 Velocity effects, hinge moment coefficient at large elevator deflections. Section 1. IRT1.

DHC-6 Tailplane OSU 7X10 Wind Tunnel Data
Velocity Effects, IRT2 Ice Shape, Section 1, Large δe 's

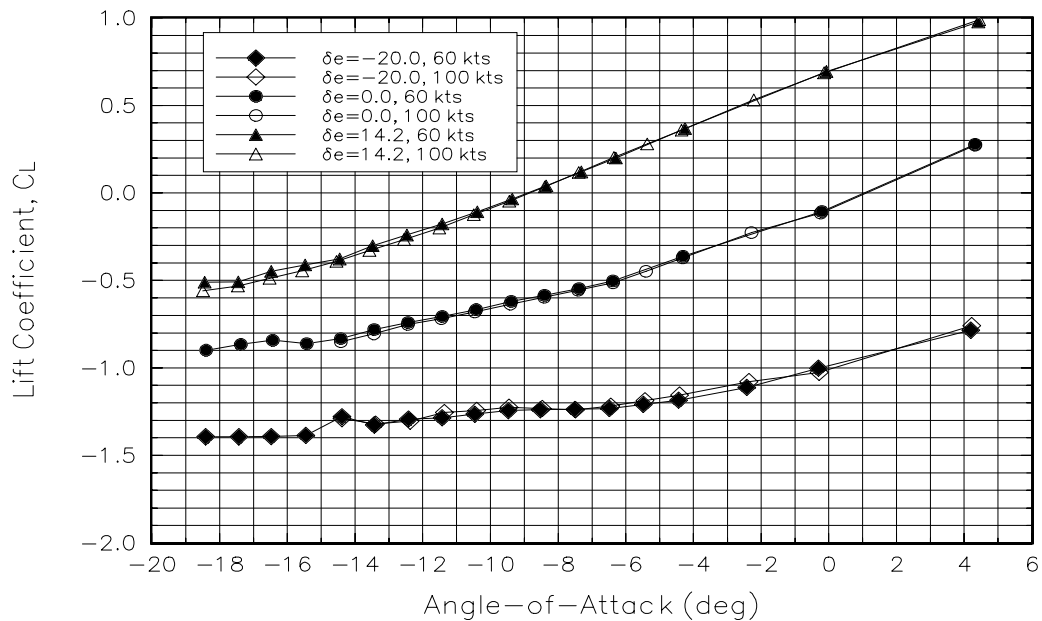


Figure 28 Velocity effects, lift coefficient at large elevator deflections. Section 1. IRT2.

DHC-6 Tailplane OSU 7X10 Wind Tunnel Data
Velocity Effects, IRT2 Ice Shape, Section 1, Large δe 's

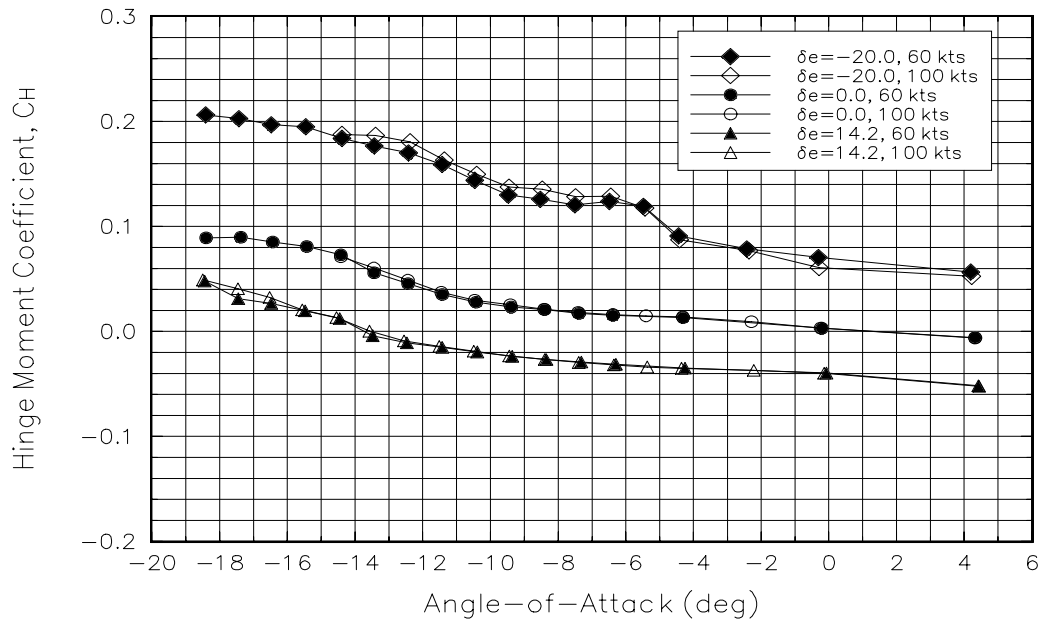


Figure 29 Velocity effects, hinge moment coefficient at large elevator deflections. Section 1. IRT2.

DHC-6 Tailplane OSU 7X10 Wind Tunnel Data
Repeatability, Section 1, Clean, 60 kts

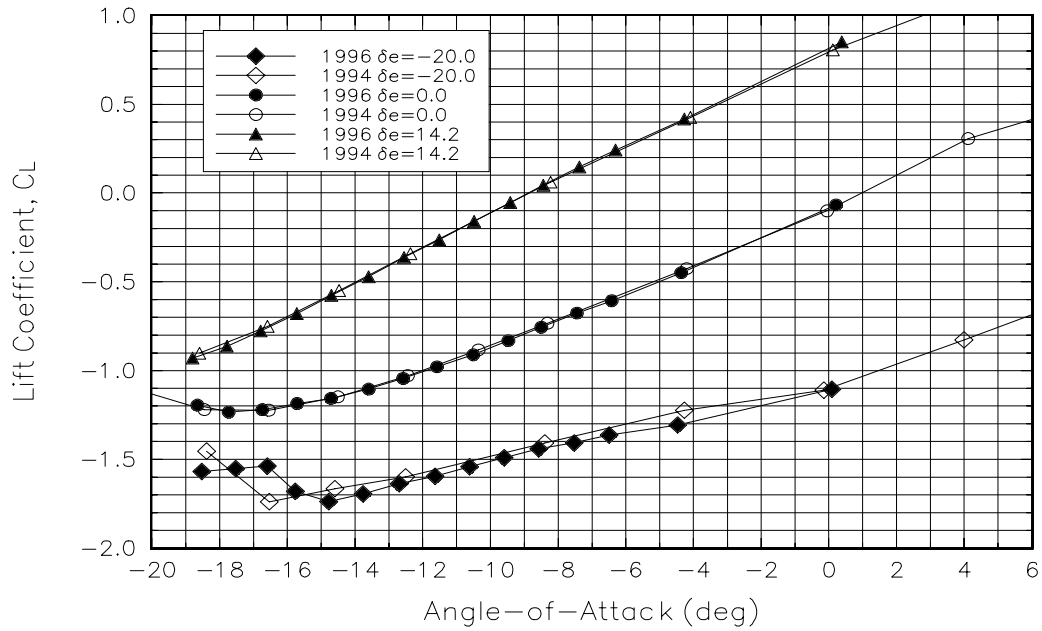


Figure 30 Repeatability check, lift coefficient w/ 1994 data vs. 1996 data. Section 1.

DHC-6 Tailplane OSU 7X10 Wind Tunnel Data
Repeatability, Section 1, Clean, 60 kts

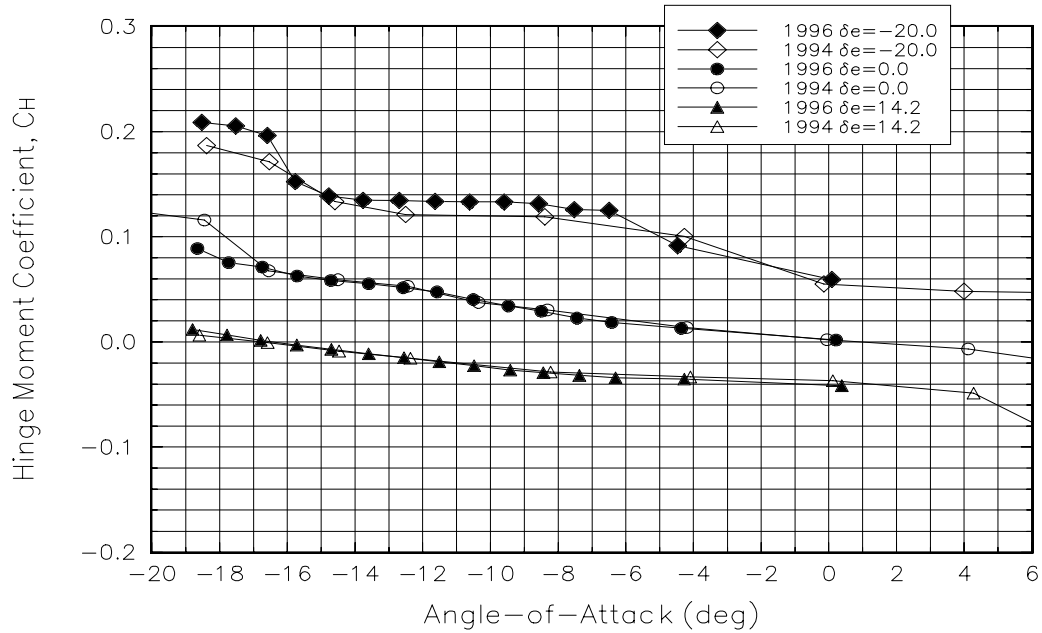


Figure 31 Repeatability check, hinge moment coefficient w/ 1994 data vs. 1996 data. Section 1.

DHC-6 Tailplane OSU 7X10 Wind Tunnel Data
Repeatability, Section 2, Clean, 60 kts

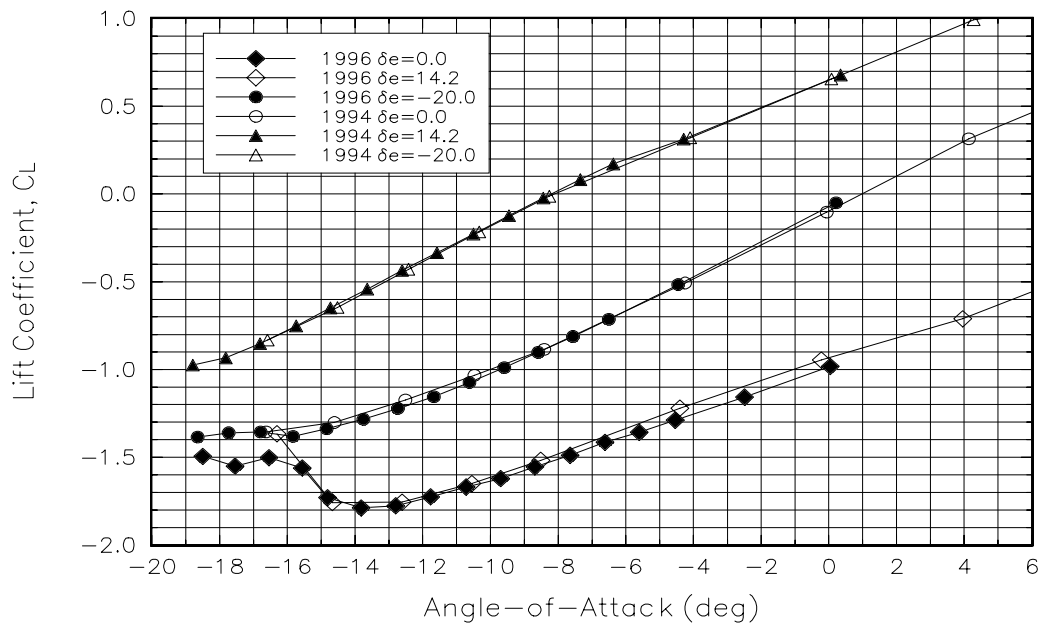


Figure 32 Repeatability check, lift coefficient w/ 1994 data vs. 1996 data. Section 2.

DHC-6 Tailplane OSU 7X10 Wind Tunnel Data
Repeatability, Section 2, Clean, 60 kts

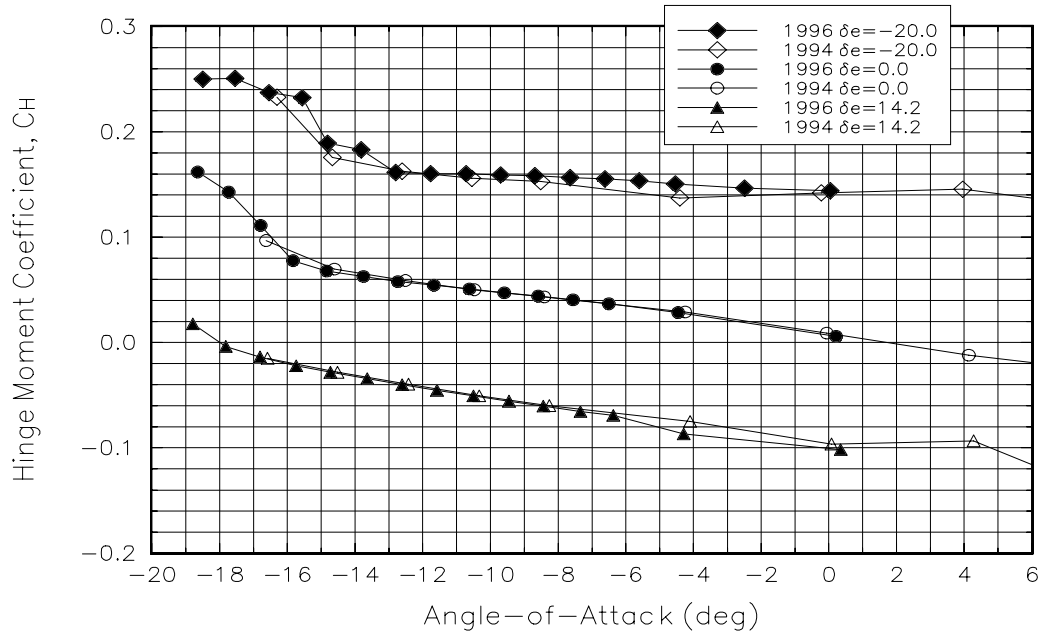


Figure 33 Repeatability check, hinge moment coefficient w/ 1994 data vs. 1996 data. Section 2.

DHC-6 Tailplane OSU 7X10 Wind Tunnel Data
Section effects, Clean, 60 kts

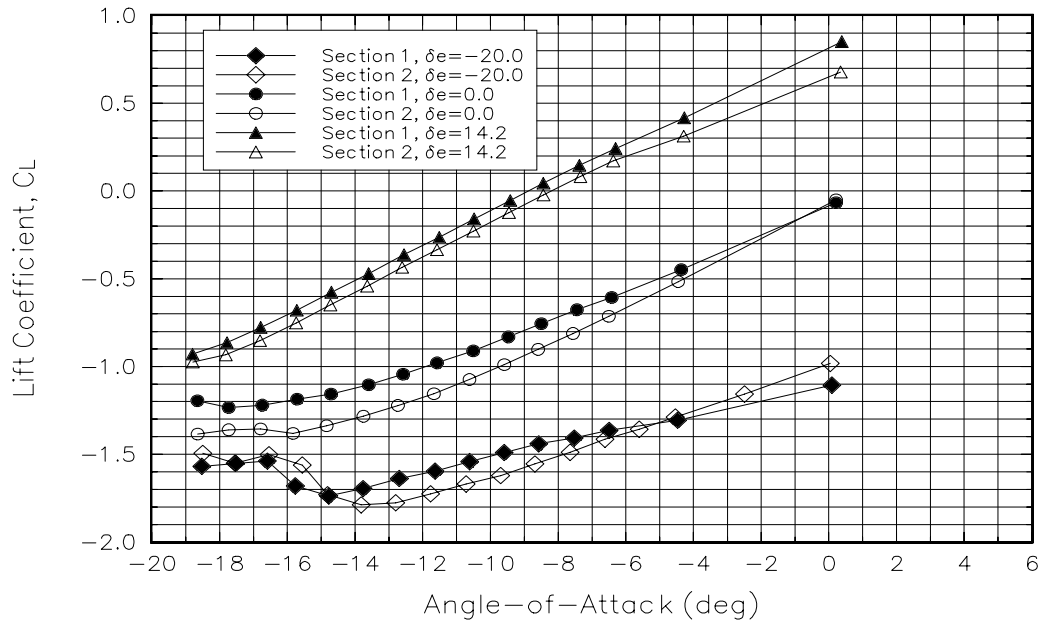


Figure 34 Section effects on the lift coefficient; clean.

DHC-6 Tailplane OSU 7X10 Wind Tunnel Data
Section effects, S&C, 60 kts

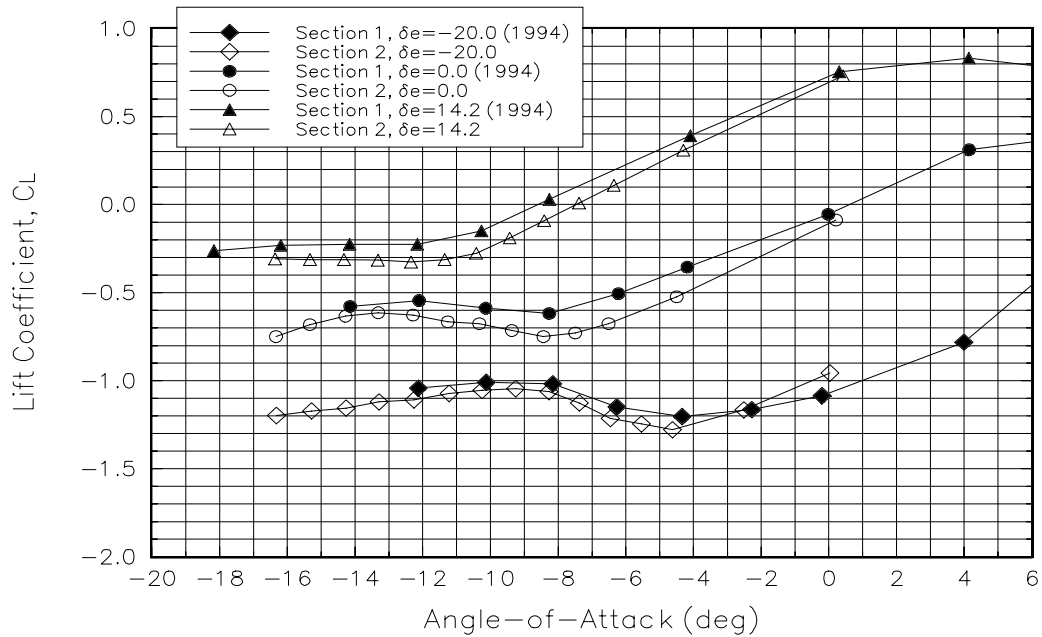


Figure 35 Section effects on the lift coefficient; S&C ice shape.

DHC-6 Tailplane OSU 7X10 Wind Tunnel Data
Section effects, Lewice, 60 kts

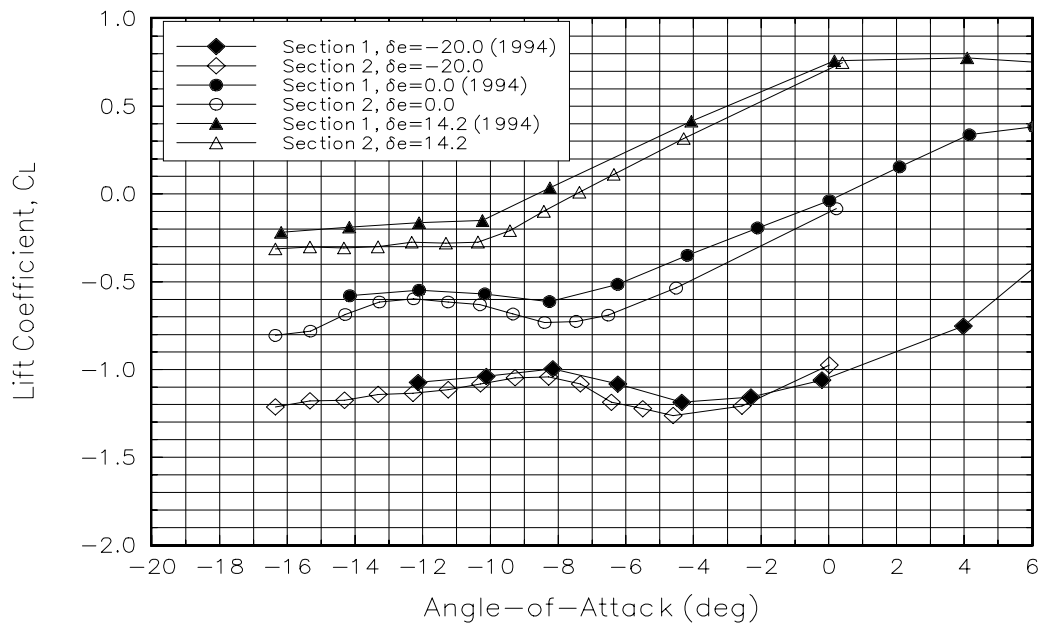


Figure 36 Section effects on the lift coefficient; LEWICE ice shape.

DHC-6 Tailplane OSU 7X10 Wind Tunnel Data
Section effects, IRT1, 60 kts

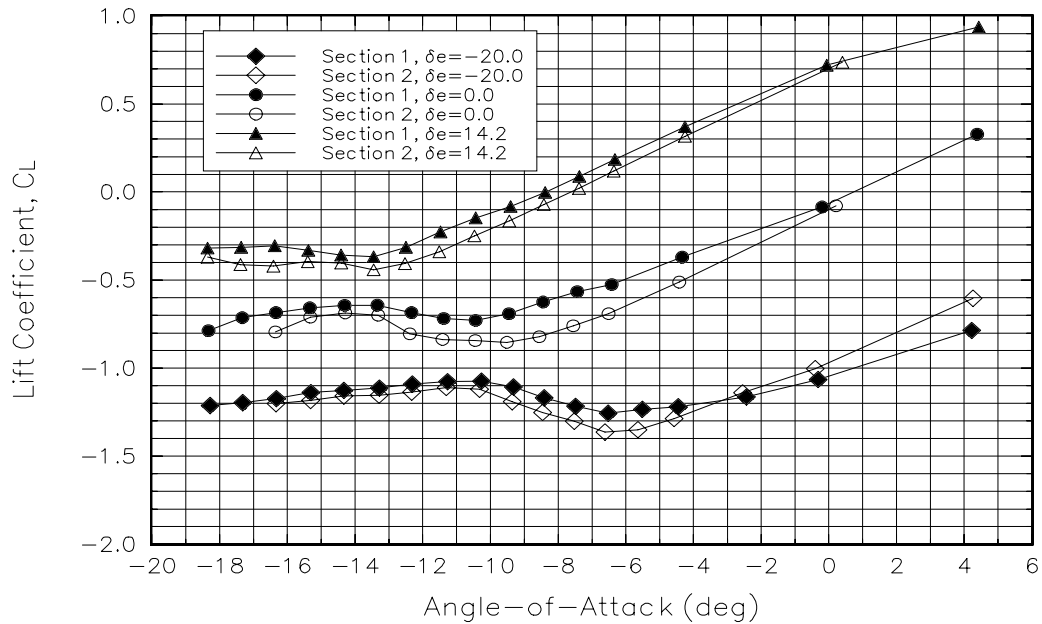


Figure 37 Section effects on the lift coefficient; IRT1 ice shape.

DHC-6 Tailplane OSU 7X10 Wind Tunnel Data
Section effects, IRT2, 60 kts

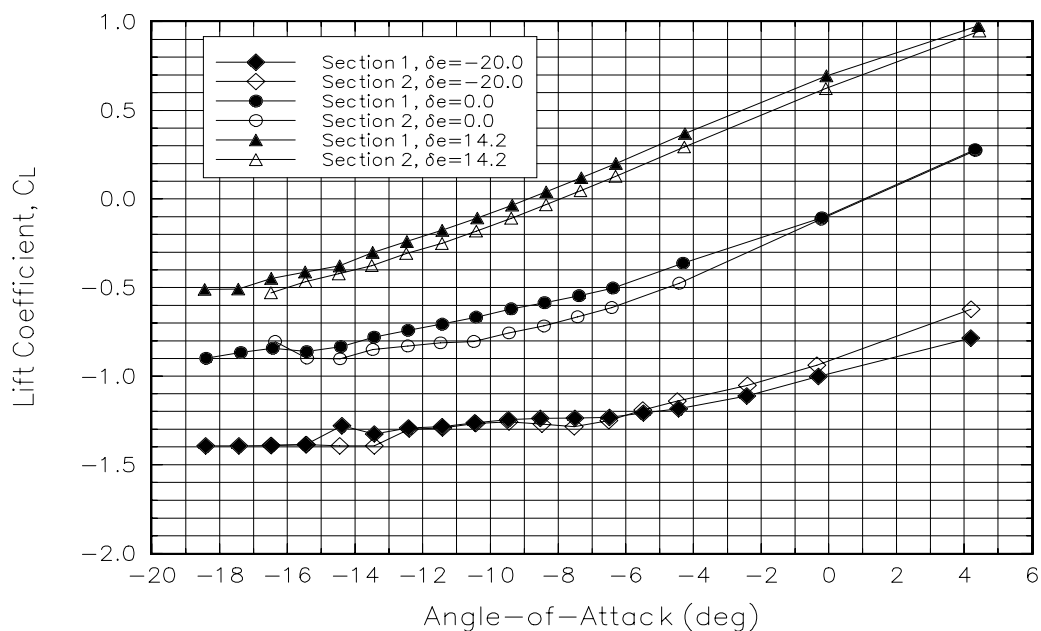


Figure 38 Section effects on the lift coefficient; IRT2 ice shape.

DHC-6 Tailplane OSU 7X10 Wind Tunnel Data
Section effects, Clean, 60 kts

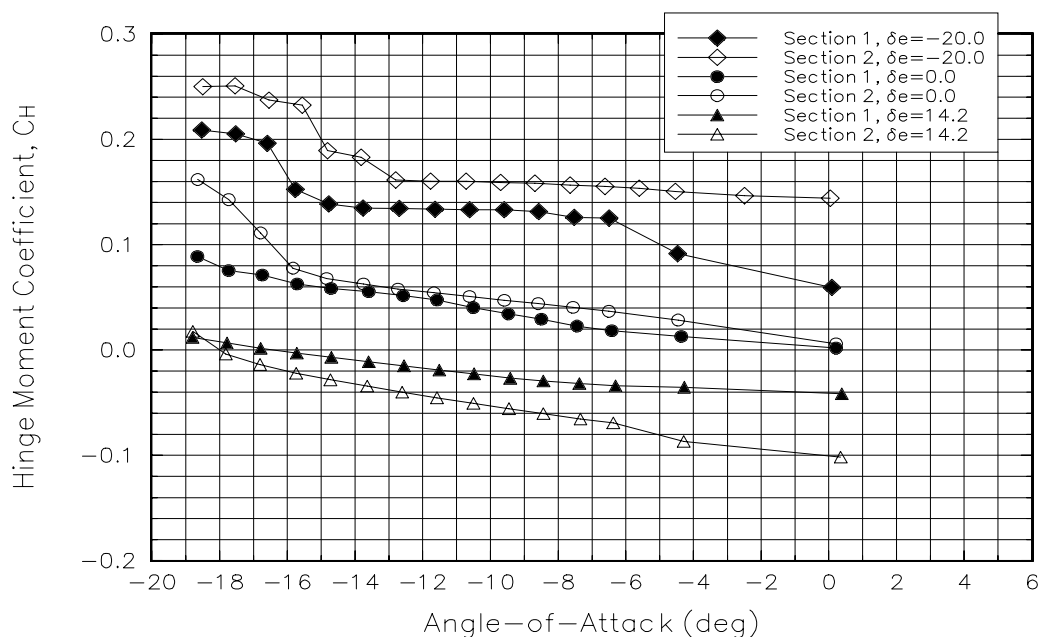


Figure 39 Section effects on the hinge moment coefficient; clean.

DHC-6 Tailplane OSU 7X10 Wind Tunnel Data
Section effects, S&C, 60 kts

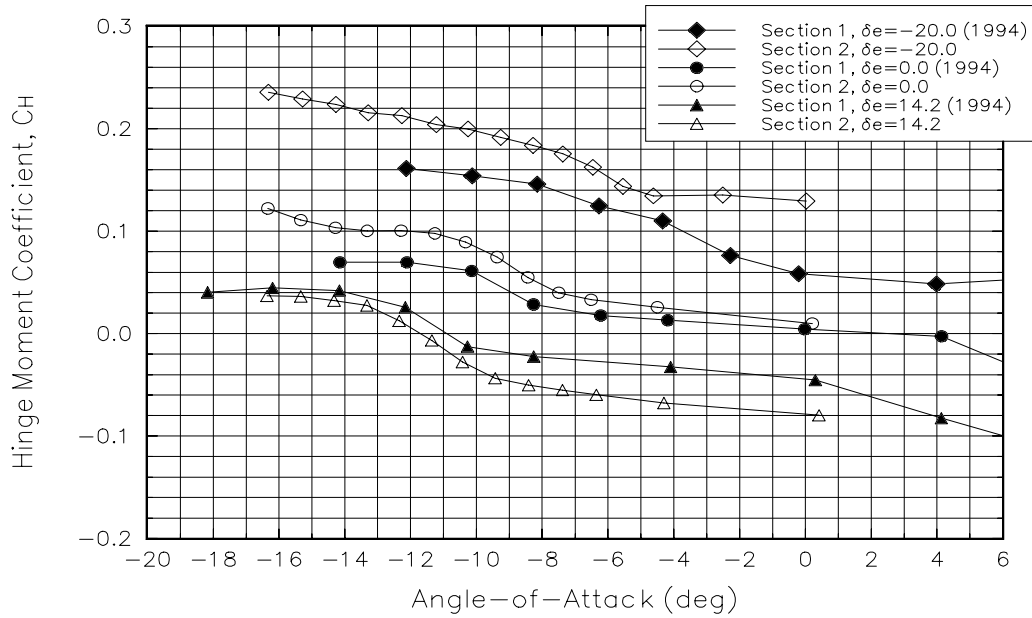


Figure 40 Section effects on the hinge moment coefficient; S&C ice shape.

DHC-6 Tailplane OSU 7X10 Wind Tunnel Data
Section effects, Lewice, 60 kts

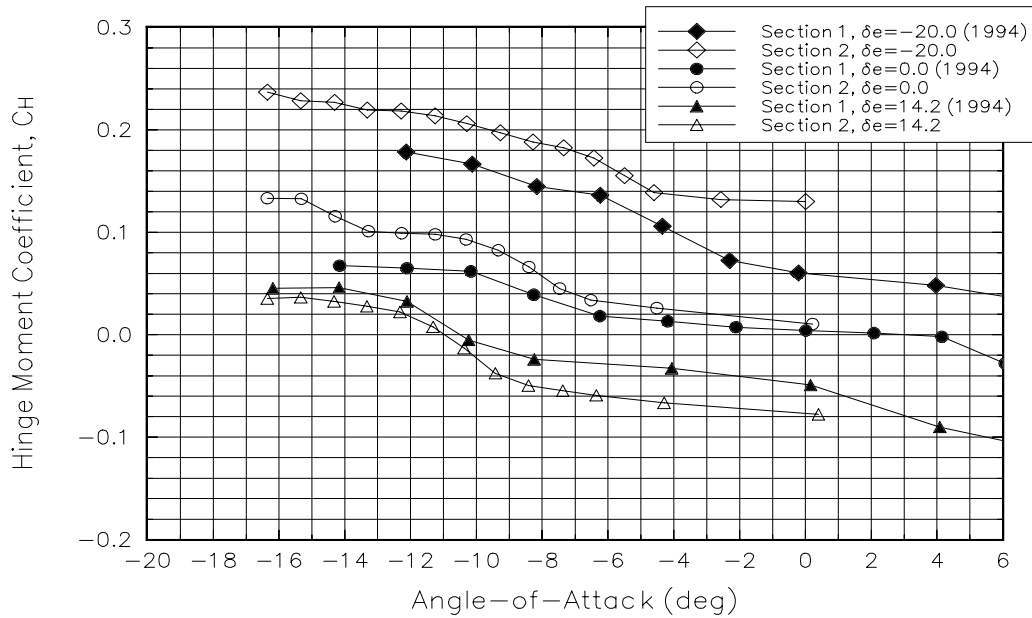
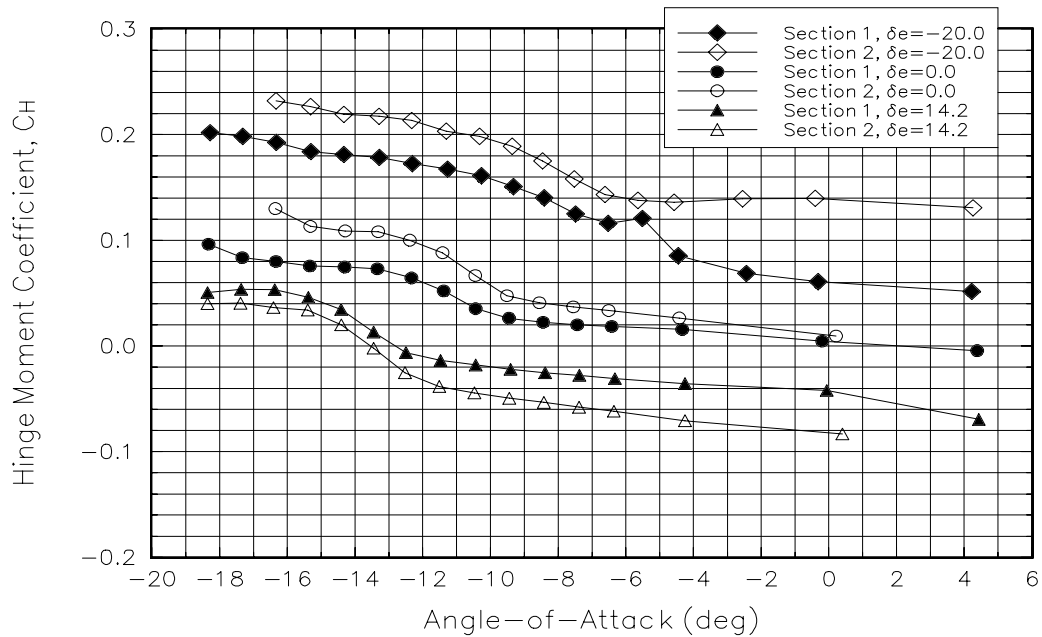


Figure 41 Section effects on the hinge moment coefficient; LEWICE ice shape.

DHC-6 Tailplane OSU 7X10 Wind Tunnel Data
Section effects, IRT1, 60 kts



**Figure 42 Section effects on the hinge moment coefficient;
IRT1 ice shape.**

DHC-6 Tailplane OSU 7X10 Wind Tunnel Data
Section effects, IRT1, 60 kts

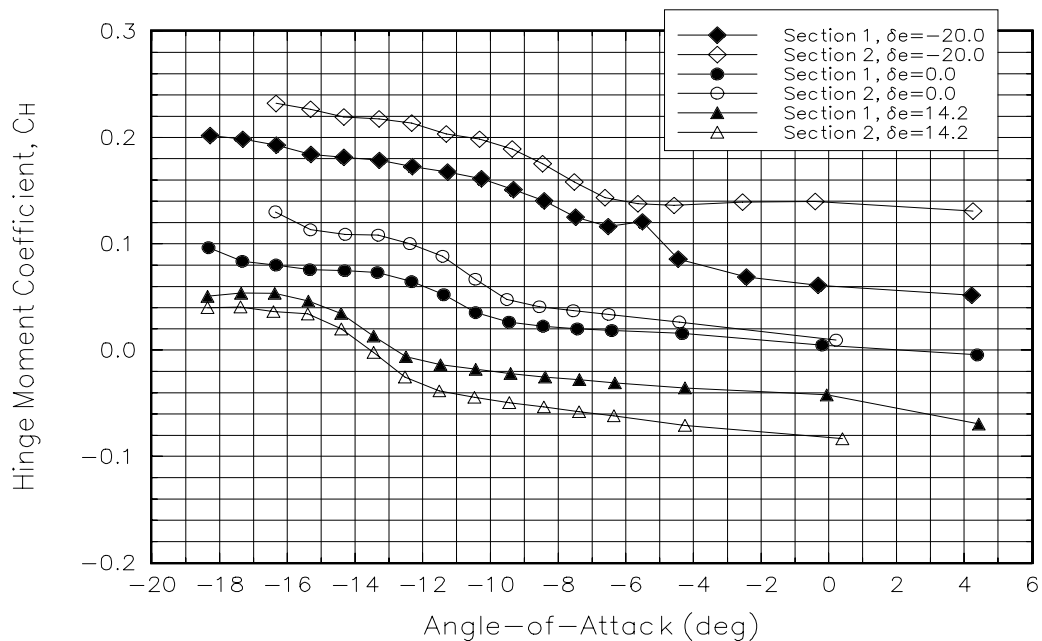


**Figure 43 Section effects on the hinge moment coefficient; IRT2 ice
shape.**

IX. Conclusions

A wind tunnel test has been completed which quantified the 2-D aerodynamics of the DHC-6 Twin Otter Tailplane with and without representative ice shapes. The results obtained are consistent with the expected aerodynamic trends. The effects of icing that would have the greatest effect on aircraft stability and control were shown in the changes in lift and hinge moment. For the clean Section 1 airfoil with $\delta_e = 0^\circ$ elevator deflection, $C_{l_{\max}} = -1.23$ and $\alpha_{\text{stall}} = -17.8^\circ$. With the IRT1 ice shape attached, these values were reduced to $C_{l_{\max}} = -0.73$ and $\alpha_{\text{stall}} = -10.5^\circ$. For the IRT2 ice shape attached, these values were reduced to $C_{l_{\max}} = -0.85$ and $\alpha_{\text{stall}} = -15.5^\circ$. Hinge moment data with ice shapes showed a definite change with the LEWICE ice shape producing the largest shift.

Velocity variations did not result in any noticeable characteristic differences and relatively small elevator deflections. Differences did show up once the elevator deflection reached the -20° position.

Varying the airfoil Section did indeed have a significant effect on the aerodynamic coefficients. In general, the $C_{l_{\max}}$ was slightly more negative for Section 2 than Section 1 while the difference in α_{stall} varied from zero to several degrees.

This wind tunnel test has produced an effective set of data with which to begin an analysis of tailplane aerodynamics in icing conditions. The data will allow the tailplane aerodynamics during simulated maneuvering flight to be quantified. Such information will allow a more complete understanding of the contribution of the tailplane to the aircraft's motion during maneuvering flight. This understanding will be needed and fully utilized in the development of maneuvers to identify aircraft susceptible to tailplane stall in icing conditions.

Appendix A Tap Locations

Section 1, Clean

TAP #	X/C	TAP #	X/C	TAP #	X/C
1	-.0011	31	.3000	74	.7448
2	.0003	32	.3500	75	.7463
3	.0001	33	.3500	76	.7888
4	.0041	34	.4000	77	.7901
5	.0039	35	.4000	78	.8327
6	.0100	36	.4500	79	.8338
7	.0100	37	.4500	80	.8767
8	.0175	38	.5000	81	.8775
9	.0169	39	.5000	82	.9207
10	.0250	40	.5226	83	.9212
11	.0250	41	.5243	84	.9646
12	.0373	42	.5180	85	.9650
13	.0380	43	.5185	86	1.0000
14	.0500	52	.5261		
15	.0500	53	.5363		
16	.0750	54	.5354		
17	.0750	55	.5462		
18	.1000	56	.5449		
19	.1000	57	.5759		
20	.1256	58	.5741		
21	.1260	59	.5955		
22	.1500	60	.5936		
23	.1500	61	.6152		
24	.1753	62	.6131		
25	.1750	63	.6346		
26	.2000	64	.6326		
27	.2000	70	.6569		
28	.2500	71	.6589		
29	.2500	72	.7009		
30	.3000	73	.7026		

Notes:

- 1) Stabilizer taps are #1–43, elevator taps are #52–86

Section 2, Clean

TAP #	X/C	TAP #	X/C	TAP #	X/C
1	-.0011	31	.3000	78	.8327
2	.0003	32	.3500	79	.8338
3	.0001	33	.3500	80	.8767
4	.0041	34	.4000	81	.8775
5	.0039	35	.4000	82	.9207
6	.0100	36	.4500	83	.9212
7	.0100	37	.4500	84	.9646
8	.0175	38	.5000	85	.9650
9	.0169	39	.5000	86	1.0000
10	.0250	44	.5500		
11	.0250	45	.5500		
12	.0373	46	.6000		
13	.0380	47	.6000		
14	.0500	48	.6173		
15	.0500	49	.6086		
16	.0750	50	.6084		
17	.0750	51	.6089		
18	.1000	65	.6119		
19	.1000	66	.6164		
20	.1256	67	.6174		
21	.1260	68	.6297		
22	.1500	69	.6314		
23	.1500	70	.6569		
24	.1753	71	.6589		
25	.1750	72	.7009		
26	.2000	73	.7026		
27	.2000	74	.7448		
28	.2500	75	.7463		
29	.2500	76	.7888		
30	.3000	77	.7901		

Notes:

- 1) Stabilizer taps are #1–51, elevator taps are #65–86

S&C Ice Shape Tap Locations

TAP #	X/C	Y/C
1	-0.0084	0.0030
2	-0.0027	0.0201
3	-0.0014	-0.0150
4	-0.0018	0.0315
5	-0.0019	-0.0264
6	0.0088	0.0308
7	0.0088	-0.0275
8	0.0175	0.0286
9	0.0175	-0.0258

LEWICE Ice Shape Tap Locations

TAP #	X/C	Y/C
1	-0.0104	0.0029
2	-0.0207	0.0338
3	-0.0165	-0.0282
4	-0.0044	0.0239
5	-0.0044	-0.0213

IRT1 Ice Shape Tap Locations

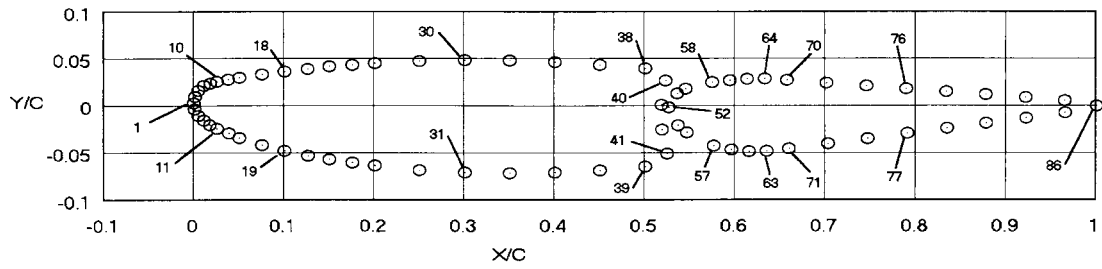
TAP#	X/C	Y/C
1	-0.0118	0.0128
2	-0.0098	0.0258
3	-0.0214	-0.0047
4	0.0026	0.0226
5	-0.0112	-0.0114
6	0.0084	0.0253
7	0.0077	-0.0189
8	0.0173	0.0278
9	0.0152	-0.0228
10	0.0250	0.0285
11	0.0237	-0.0266
12	0.0377	0.0311
13	0.0365	-0.0314
14	0.0502	0.0325
15	0.0486	-0.0358
16	0.0756	0.0343
17	0.0738	-0.0434

IRT2 Ice Shape Tap Locations

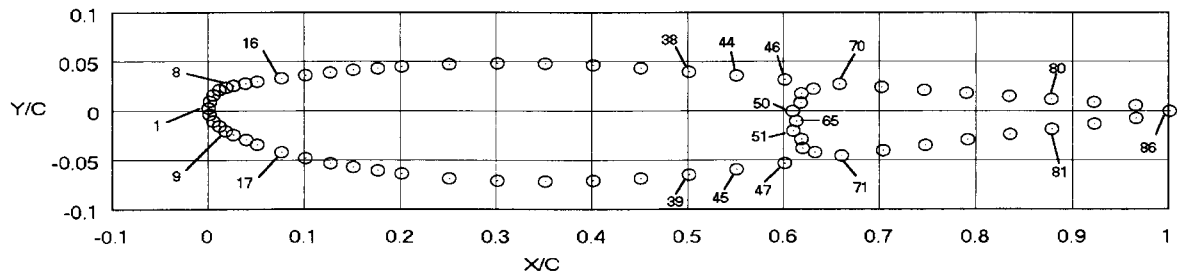
TAP#	X/C	Y/C
1	-0.0057	0.0033
2	-0.0037	0.0110
3	-0.0055	-0.0060
4	0.0005	0.0176
5	-0.0009	-0.0133
6	0.0095	0.0238
7	0.0075	-0.0189
8	0.0172	0.0275
9	0.0148	-0.0220
10	0.0253	0.0290
11	0.0234	-0.0257
12	0.0380	0.0311
13	0.0367	-0.0308
14	0.0506	0.0322
15	0.0487	-0.0353
16	0.0759	0.0336
17	0.0741	-0.0422

Tap Locations for the Various Ice Shapes

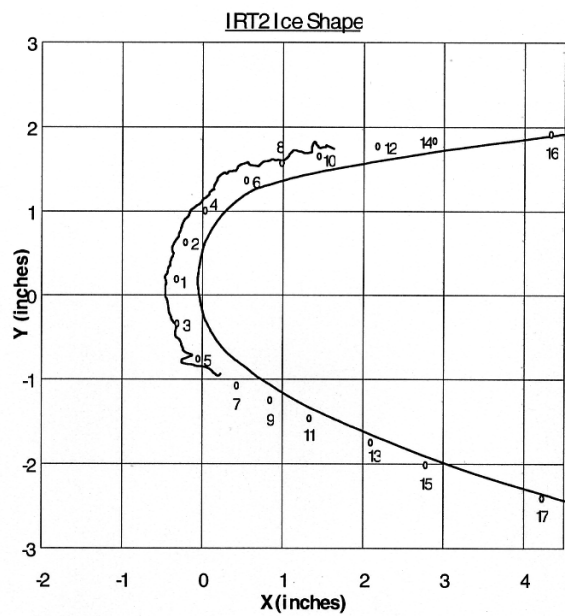
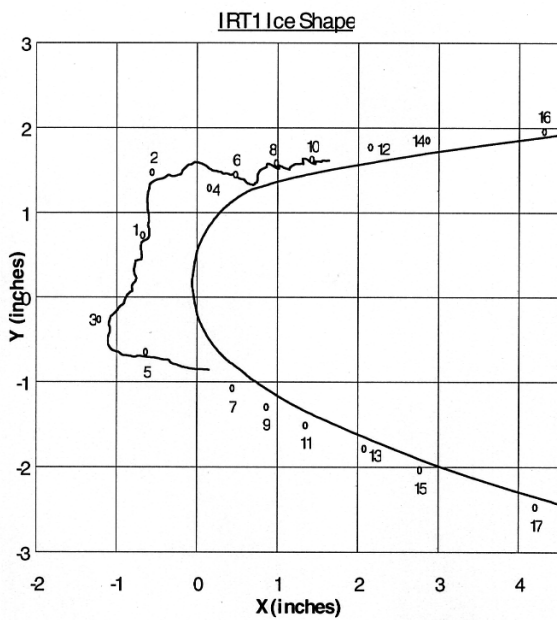
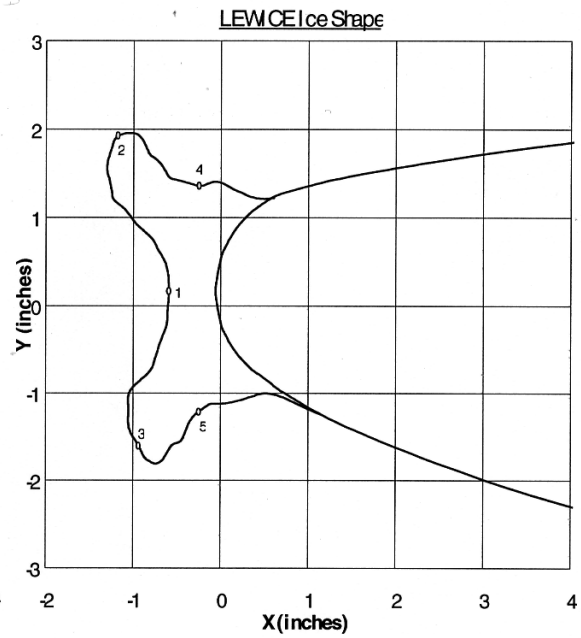
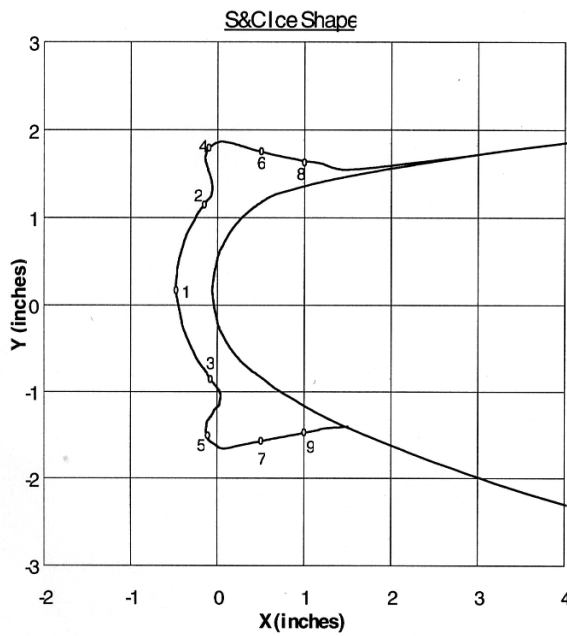
Section 1 (Baseline)



Section 2



DHC-6 Tailplane Airfoil Section Tap Locations



Airfoil Profiles With Ice Shapes and Tap Locations

Appendix B

Run Log

Run #	Section	Ice Shape	Elevator	Velocity	Wake?	.HIS file	Notes
0001	2	Clean	0.0°	60 kts	No	try.his	Check run
0002	2	Clean	0.0°	60 kts	No	test2.his	Check run
0003	2	Clean	0.0°	60 kts	No	tip201.his	Bad run
1103	2	Clean	0.0°	60 kts	Yes	tip207.his	Bad run
2203	2	Clean	0.0°	60 kts	No	tip207.his	Bad run
3303	2	Clean	0.0°	60 kts	No	tip212.his	
4403	2	Clean	0.0°	60 kts	No	tip212.his	Repeat run
0004	2	Clean	10.0°	60 kts	No	tip201.his	Bad run
0005	2	Clean	14.2°	60 kts	Yes	tip208.his	Bad run
2205	2	Clean	14.2°	60 kts	No	tip212.his	
0006	2	Clean	-10.0°	60 kts	No	tip201.his	Bad run
0007	2	Clean	-20.0°	60 kts	Yes	tip206.his	Bad run
2207	2	Clean	-20.0°	60 kts	No	tip212.his	
0008	2	Clean	-26.6°	60 kts	No	tip201.his	Bad run
0009	2	S&C	0.0°	60 kts	No	tip202.his	Bad run
0010	2	S&C	14.2°	60 kts	No	tip202.his	Bad run
A0010	2	S&C	14.2°	60 kts	No	tip202.his	Bad run
0011	2	S&C	-20.0°	60 kts	No	tip202.his	Bad run
0012	2	Lewice	0.0°	60 kts	Yes	tip204.his	Bad run
0013	2	Lewice	14.2°	60 kts	No	tip203.his	Bad run
XX0013	2	Lewice	14.2°	60 kts	No	tip203.his	Chk.Wk.Pb.
0014	2	Lewice	-20.0°	60 kts	No	tip205.his	Bad run
0015	2	IRT1	0.0°	60 kts	Yes	tip210.his	
0016	2	IRT1	10.0°	60 kts	No	tip209.his	
0017	2	IRT1	14.2°	60 kts	Yes	tip209.his	
8817	2	IRT1	14.2°	60 kts	No	test3.his	Bad run
9917	2	IRT1	14.2°	60 kts	No	test3.his	Bad run
0018	2	IRT1	-10.0°	60 kts	No	tip211.his	Ran backward
1118	2	IRT1	-10.0°	60 kts	No	tip211.his	
0019	2	IRT1	-20.0°	60 kts	Yes	tip211.his	
0021	2	IRT2	14.2°	60 kts	Yes	tip228.his	
0022	2	IRT2	10.0°	60 kts	No	tip228.his	
0023	2	IRT2	0.0°	60 kts	Yes	tip229.his	
0024	2	IRT2	-10.0°	60 kts	No	tip231.his	
0025	2	IRT2	-20.0°	60 kts	Yes	tip230.his	
0027	1	Clean	0.0°	60 kts	Yes	tip213.his	
1127	1	Clean	0.0°	60 kts	No	tip215.his	Repeat run
0028	1	Clean	14.2°	60 kts	Yes	tip214.his	
0029	1	Clean	-20.0°	60 kts	Yes	tip215.his	Bad run
1129	1	Clean	-20.0°	60 kts	No	tip215.his	Bad run
2229	1	Clean	-20.0°	60 kts	No	tip220.his	

Run #	Section	Ice Shape	Elevator	Velocity	Wake?	.HIS file	Notes
0030	1	IRT1	0.0°	60 kts	yes	tip218.his	
0031	1	IRT1	0.0°	100 kts	no	tip218.his	
0032	1	IRT1	10.0°	60 kts	no	tip219.his	
0033	1	IRT1	14.2°	60 kts	yes	tip219.his	
0034	1	IRT1	14.2°	100 kts	no	tip219.his	
0035	1	IRT1	-10.0°	60 kts	no	tip217.his	
0036	1	IRT1	-20.0°	60 kts	yes	tip216.his	
1136	1	IRT1	-20.0°	60 kts	yes	tip217.his	Repeat run
0037	1	IRT1	-20.0°	100 kts	no	tip216.his	
0038	1	IRT1	-15.0°	60 kts	no	tip219.his	
0039	1	IRT1	-26.6°	60 kts	no	tip219.his	
0040	1	IRT2	0.0°	60 kts	yes	tip224.his	
0041	1	IRT2	0.0°	100 kts	no	tip225.his	
0042	1	IRT2	10.0°	60 kts	no	tip226.his	
0043	1	IRT2	14.2°	60 kts	yes	tip227.his	
0044	1	IRT2	14.2°	100 kts	no	tip227.his	
0045	1	IRT2	-10.0°	60 kts	no	tip221.his	
1145	1	IRT2	-10.0°	60 kts	no	tip221.his	Repeat run
0046	1	IRT2	-20.0°	60 kts	yes	tip222.his	
0047	1	IRT2	-20.0°	100 kts	no	tip222.his	
0048	1	IRT2	-26.6°	60 kts	no	tip223.his	
0050	1	Clean	-10.0°	60 kts	no	tip220.his	
0051	2	Grit	0.0°	60 kts	yes	tip241.his	Additional run
0052	2	Grit	-10.0°	60 kts	yes	tip242.his	Additional run
0053	2	Grit	14.2°	60 kts	no	tip239.his	Additional run
0054	2	Grit	10.0°	60 kts	yes	tip240.his	Additional run
0055	2	Grit	-20.0°	60 kts	no	tip243.his	Additional run
0056	2	Clean	10.0°	60 kts	no	tip233.his	Repeat of 0004
0057	2	Clean	-10.0°	60 kts	no	tip232.his	Repeat of 0006
1157	2	Clean	-10.0°	60 kts	no	tip232.his	Repeat run
0058	2	Clean	-26.6°	60 kts	no	tip232.his	Repeat of 0008
0059	2	S&C	0.0°	60 kts	yes	tip237.his	Repeat of 0007
0060	2	S&C	14.2°	60 kts	no	tip237.his	Repeat of 0010
0061	2	S&C	-20.0°	60 kts	no	tip238.his	Repeat of 0011
0062	2	Lewice	0.0°	60 kts	yes	tip235.his	Repeat of 0012
0063	2	Lewice	14.2°	60 kts	no	tip234.his	Repeat of 0013
0064	2	Lewice	-20.0°	60 kts	no	tip236.his	Repeat of 0014

Appendix C

Solid Wall Correction Calculations

The effect of the walls on the 2-Dimensional airfoil data must be considered. Corrections have been applied to the raw wind tunnel data using the methods of Ref. 2. For this test, three phenomena have been taken into account:

Solid Blockage

Solid blockage creates an increase in velocity due to the reduction of the area through which the air must flow. To quantify this effect, computations have been made by considering the 2-Dimensional model as a cylinder. This cylinder can be simulated as a doublet of strength $\mu = 2\pi V a^2$ (a: the cylinder radius), with the walls represented by the streamlines created by matching doublets on each side of the cylinder. Therefore,

$$\frac{\Delta V}{V_u} = \frac{a^2}{h^2}$$

(The subscript u indicates uncorrected data)

After doing a summation, we obtain,

$$\varepsilon_{sb} = \left(\frac{\Delta V}{V_u} \right)_{tot} = \Lambda \sigma$$

with:

h: tunnel height
c: model chord

$$\sigma = \left(\frac{\pi^2}{48} \right) \left(\frac{c}{h} \right)^2$$

$$\Lambda = \frac{16}{\pi} \int_0^1 \frac{y}{c} \left[(1 - P) \left(1 + \frac{dy}{dx} \right) \right]^{\frac{1}{2}} d \frac{x}{c}$$

x, y: airfoil coordinates, P is no-camber, symmetrical, pressure distribution.

Usually Λ is given by a graph. In our case, $\Lambda = 0.22$

Wake Blockage

Wake blockage creates a velocity increment at the model because of a pressure gradient due to higher velocity which keeps the flow around the model. In computations, the wake is simulated by a line source and the walls by an infinite vertical row of source/sink combinations. This reduces to:

$$\varepsilon_{wb} = \frac{\Delta V}{V_u} = \frac{c}{4h} C_{du}$$

We can then correct the tunnel conditions by these equations:

$$V = V_u (1 + \varepsilon)$$

$$\text{with : } \varepsilon = \varepsilon_{sb} + \varepsilon_{wb}$$

$$q = q_u (1 + 2\varepsilon)$$

$$\text{Re} = \text{Re}_u (1 + \varepsilon)$$

From the dynamic pressure effect and the wake gradient term, we get:

$$C_d = C_{du} (1 - 3\varepsilon_{sb} - 2\varepsilon_{wb})$$

Streamline Curvature

The lift and moment about the quarter chord of an airfoil are too large at a given angle of attack (which is also too large). This is due to the fact that the airfoil seems to have more camber because of the floor and ceiling.

Calculations of this effect are made by assuming that the airfoil can be approximated by a single vortex at its quarter-chord point. The floor and ceiling are represented by a vertical row of vortices, extending to infinity and with alternating signs. The load on the airfoil can be decomposed as a flat plate loading, computed as an angle of attack correction and an elliptical loading which gives the lift, pitching moment, and hinge moment corrections.

It can be shown that the upwash induced at the half chord by the two images is:

$$\Delta\alpha = \frac{1}{8\pi} \frac{c^2}{h^2 + \left(\frac{c}{4}\right)^2} Cl$$

We can consider that $(c/4)^2$ is small compared to h^2 , so it gives σ equal to σ previously found, and we have then :

$$\alpha = \alpha_u + \frac{57.3\sigma}{2\pi} \left(C_{lu} + 4C_{\frac{1}{m-4}u} \right)$$

$$C_l = C_{lu} (1 - \sigma - 2\varepsilon)$$

$$C_{\frac{1}{m-4}} = C_{\frac{1}{m-4}u} (1 - 2\varepsilon) + \frac{\sigma C_l}{4}$$

Hinge Moment

To establish a correction for the hinge moment, we follow the same analysis process discussed above, but we consider only the flap or elevator instead of the entire airfoil. We are now at a three-quarter-chord point, so we lose accuracy by taking $(3c/h)^2 \ll h^2$ in the $\Delta\alpha$ expression. Therefore, including this $3c/4$ term results in $\sigma' = 0.9\sigma$.

So,

$$C_h = C_{hu} (1 - 2\varepsilon) + \frac{\sigma'}{4} C_{lf}$$

with: C_{lf} = lift coefficient of the elevator.

Appendix D

Data Reduction Output File Formats

Uncorrected Coefficients

File Name: AA500XX.DAT

Run: 00XX

Column	Value
1	Angle-of-Attack (degrees)
2	Elevator Deflection (degrees)
3	Mach Number
4	Reynolds Number (millions)
5	Q (psi)
6	Velocity (kts.)
From Surface Taps	
7	CL (total)
8	CD (pressure only)
9	CM (1/4c)
10	CL (Elevator only)
11	CH (Elevator)
From Belt Taps (although not used)	
12	CL
13	CD (pressure only)
14	CM (1/4c)
15	CL (Elevator only)
16	CH (Elevator)
17	Run Number

Corrected Coefficients using Surface Taps

File Name: SC500XX.DAT

Run: 00XX

Column	Value
1	Angle-of-Attack (degrees)
2	Elevator Deflection (degrees)
3	Mach Number
4	Reynolds Number (millions)
5	Q (psi)
6	Velocity (kts.)
7	CL (total)
8	CD (pressure only)
9	CM (1/4c)
10	CH (Elevator)

Appendix E

DHC-6 Twin Otter Tailplane Coefficient Data

List of Figures From Appendix E.

Figure E 1. Ice Shape Effects, Section 1, $\delta e = 0.0^\circ$	50
Figure E 2. Ice Shape Effects, Section 1, $\delta e = 10.0^\circ$	51
Figure E 3. Ice Shape Effects, Section 1, $\delta e = 14.2^\circ$	52
Figure E 4. Ice Shape Effects, Section 1, $\delta e = -10.0^\circ$	53
Figure E 5. Ice Shape Effects, Section 1, $\delta e = -20.0^\circ$	54
Figure E 6. Ice Shape Effects, Section 1, $\delta e = -26.6^\circ$	55
Figure E 7. Ice Shape Effects, Section 2, $\delta e = 0.0^\circ$	56
Figure E 8. Ice Shape Effects, Section 2, $\delta e = 10.0^\circ$	57
Figure E 9. Ice Shape Effects, Section 2, $\delta e = 14.2^\circ$	58
Figure E 10. Ice Shape Effects, Section 2, $\delta e = -10.0^\circ$	59
Figure E 11. Ice Shape Effects, Section 2, $\delta e = -20.0^\circ$	60
Figure E 12. Section Effects, Clean, Large Elevator Deflections.....	61
Figure E 13. Section Effects, IRT1 Ice Shape, Small Elevator Deflections	62
Figure E 14. Section Effects, IRT1 Ice Shape, Large Elevator Deflections	63
Figure E 15. Section Effects, IRT2 Ice Shape, Small Elevator Deflections	64
Figure E 16. Section Effects, IRT2 Ice Shape, Large Elevator Deflections	65
Figure E 17. Section Effects, LEWICE Ice Shape, Large Elevator Deflections.....	66
Figure E 18. Section Effects, S&C Ice Shape, Large Elevator Deflections.....	67
Figure E 19. Velocity Effects, IRT1 Ice Shape, Section 1, Large Elevator Deflections.....	68
Figure E 20. Velocity Effects, IRT2 Ice Shape, Section 1, Large Elevator Deflections.....	69
Figure E 21. Clean, Section 1	70
Figure E 22. Clean, Section 2	71
Figure E 23. Grit Applied, Section 2	72
Figure E 24. IRT1 Ice Shape, Section 1, $V = 60$ kts.....	73
Figure E 25. IRT1 Ice Shape, Section 1, $V = 100$ kts.....	74
Figure E 26. IRT1 Ice Shape, Section 2.....	75
Figure E 27. IRT2 Ice Shape, Section 1, $V = 60$ kts.....	76
Figure E 28. IRT2 Ice Shape, Section 1, $V = 100$ kts.....	77
Figure E 29. IRT2 Ice Shape, Section 2.....	78

Ice Shape Effects, $V=60$ kts, Section 1, $\delta e=0.0$

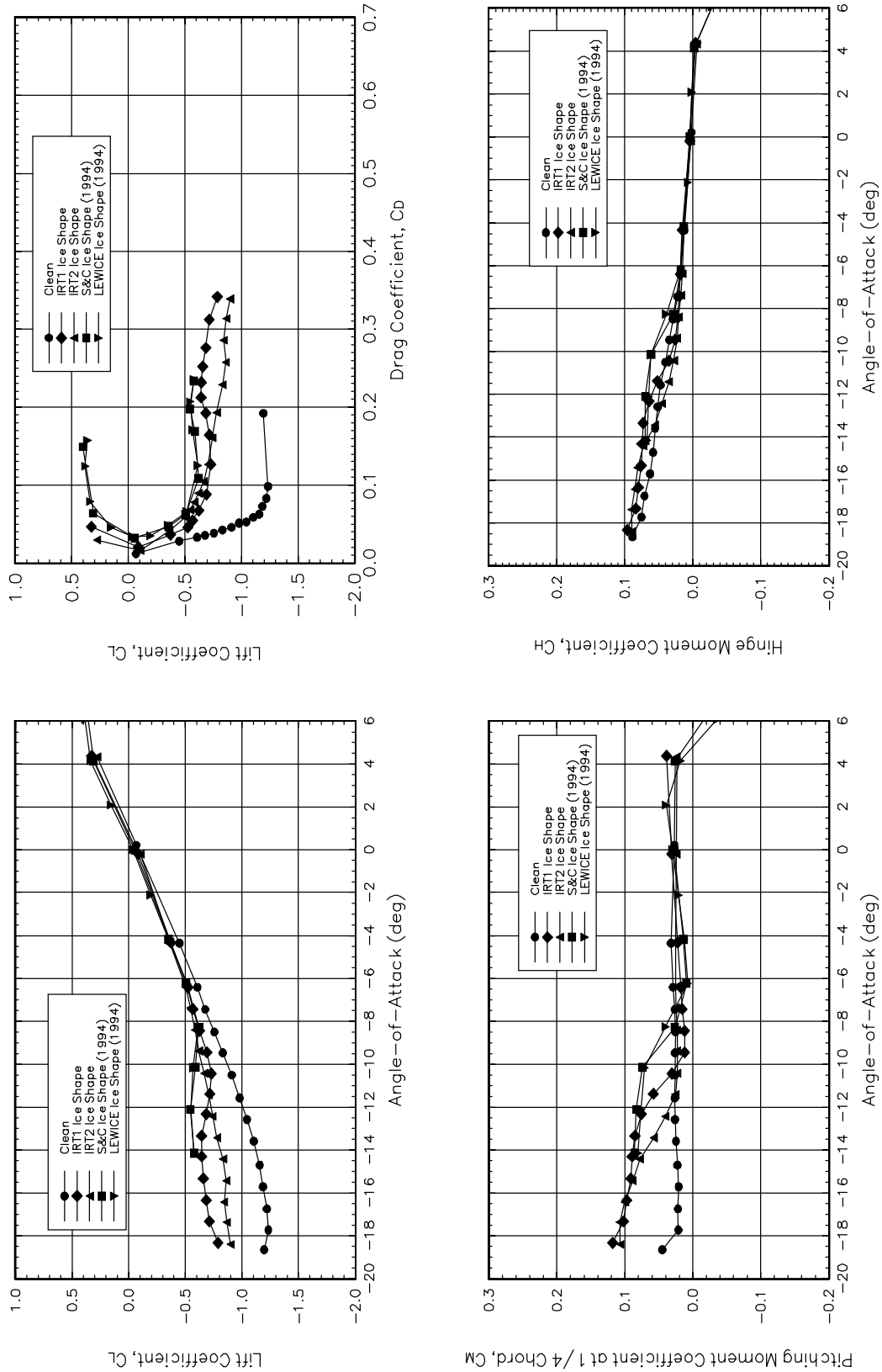


Figure E 1. Ice Shape Effects, Section 1, $\delta e = 0.0^\circ$.

Ice Shape Effects, $V=60$ kts, Section 1, $\delta e=10.0$

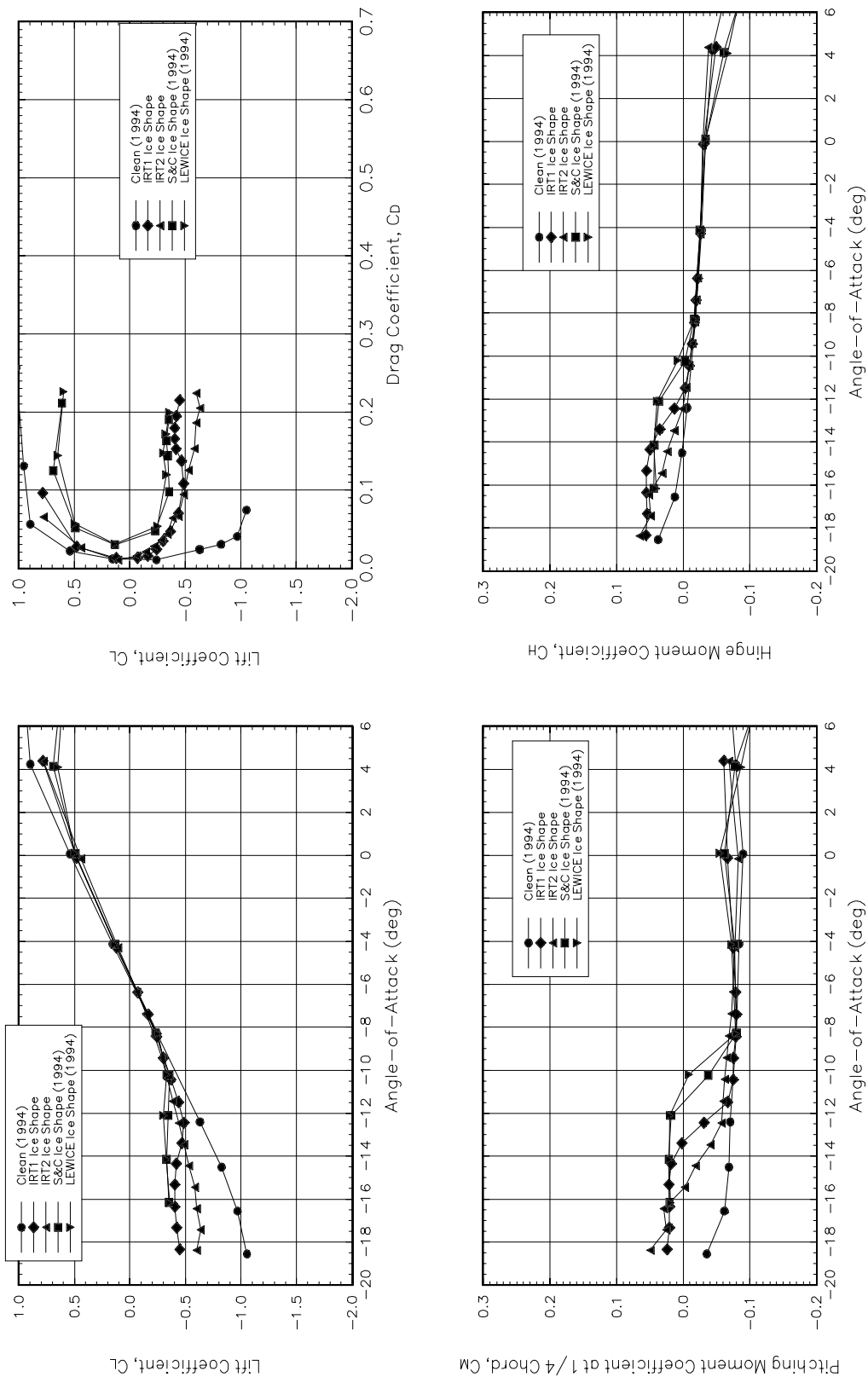


Figure E 2. Ice Shape Effects, Section 1, $\delta e = 10.0^\circ$.

Ice Shape Effects, $V=60$ kts, Section 1, $\delta e=14.2^\circ$

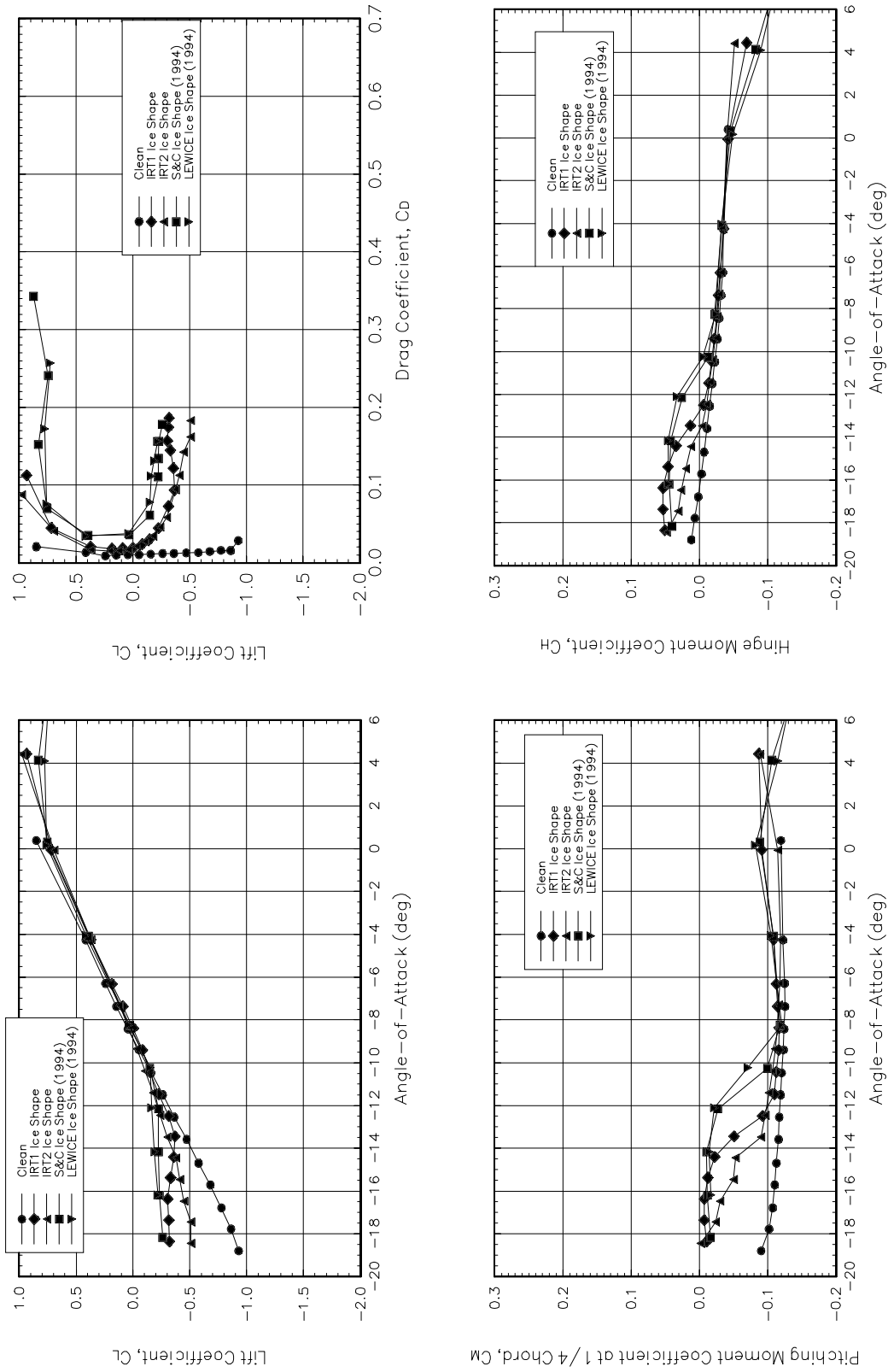


Figure E 3. Ice Shape Effects, Section 1, $\delta e=14.2^\circ$.

Ice Shape Effects, $V=60$ kts, Section 1, $\delta e=-10.0$

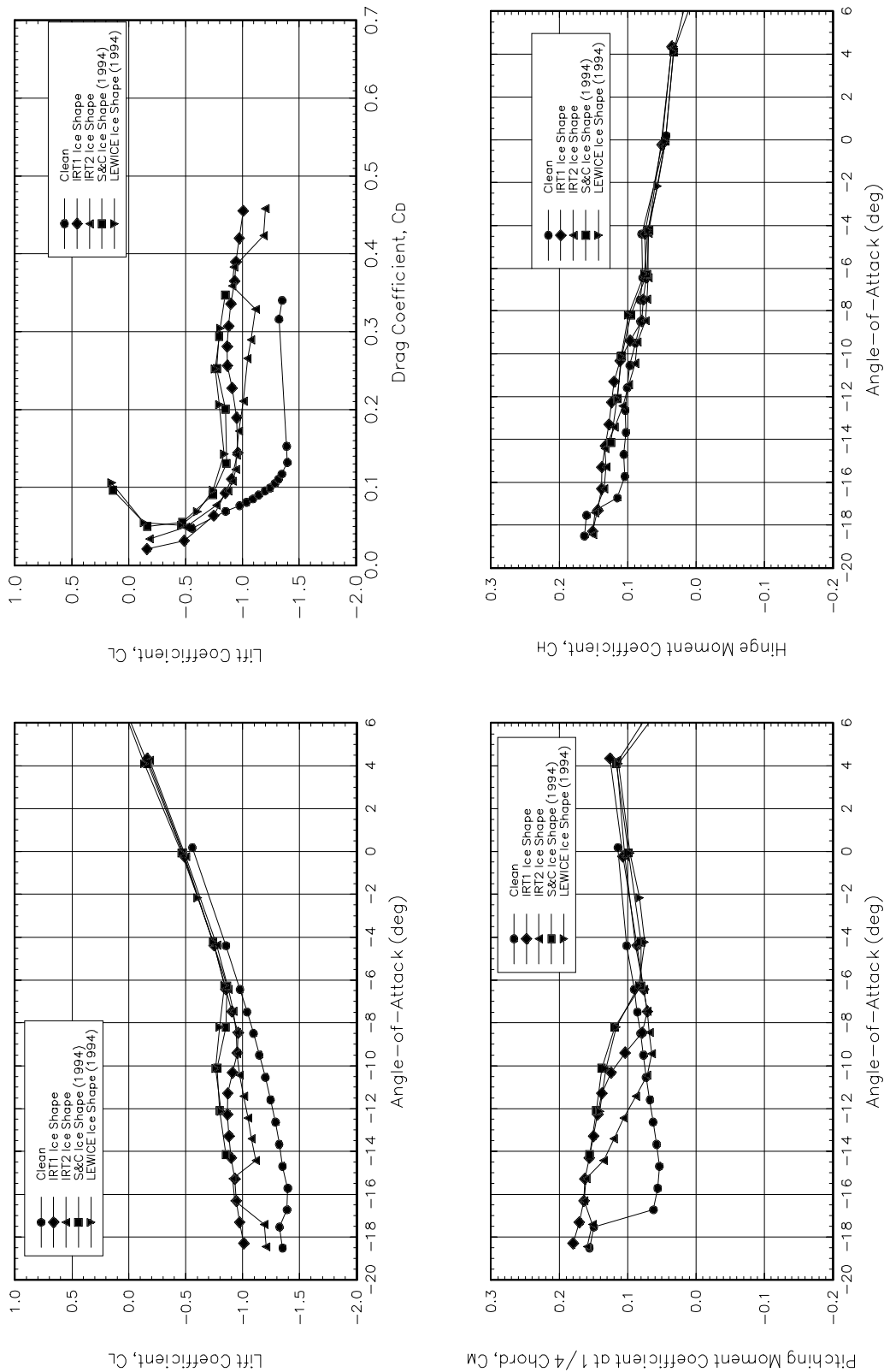


Figure E 4. Ice Shape Effects, Section 1, $\delta e=-10.0^\circ$.

Ice Shape Effects, $V=60$ kts, Section 1, $\delta e=-20.0$

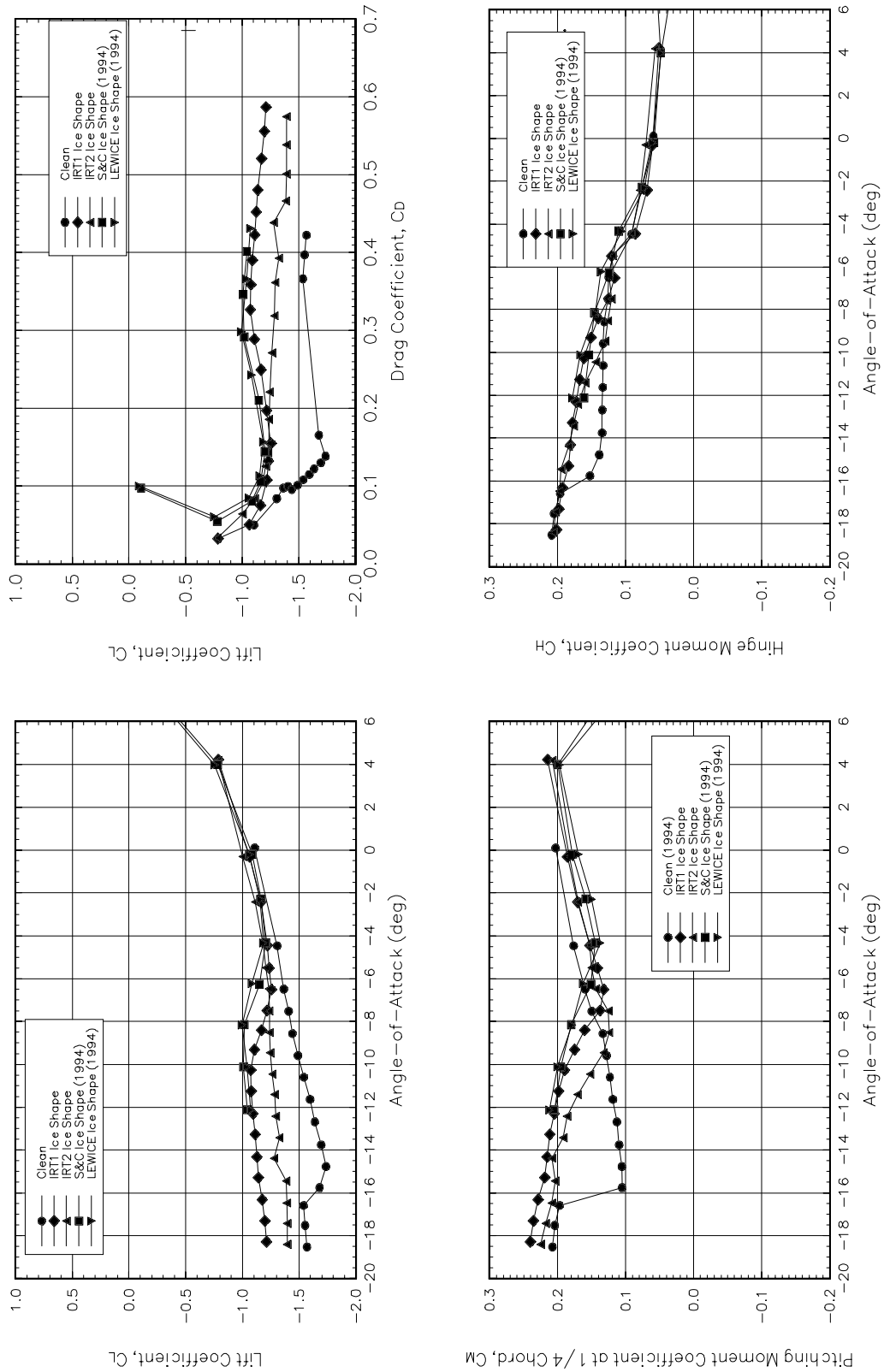


Figure E 5. Ice Shape Effects, Section 1, $\delta e=-20.0^\circ$.

Ice Shape Effects, $V=60$ kts, Section 1, $\delta e=-26.6^\circ$

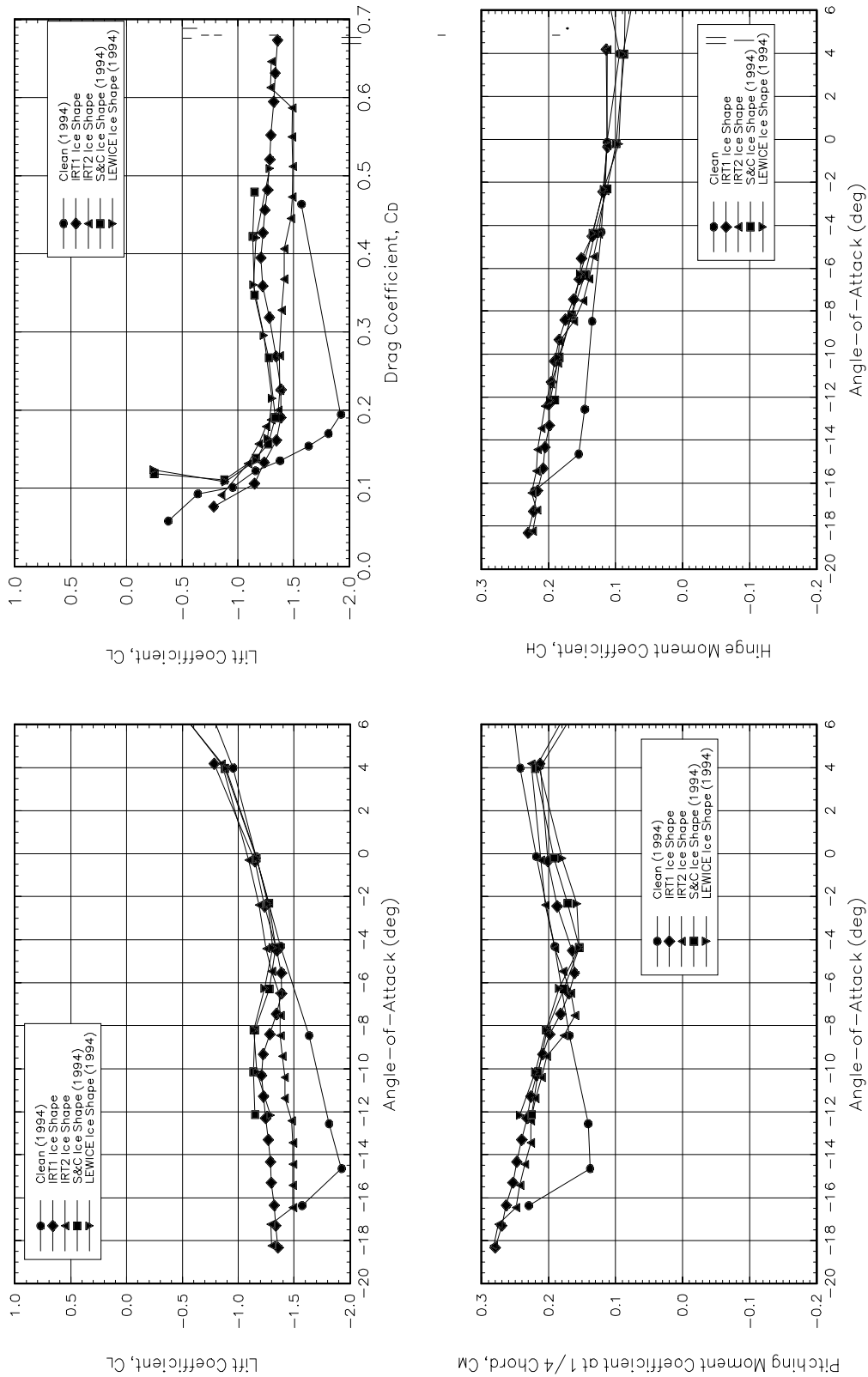


Figure E 6. Ice Shape Effects, Section 1, $\delta e=-26.6^\circ$.

Ice Shape Effects, $V=60$ kts, Section 2, $\delta e=0.0$

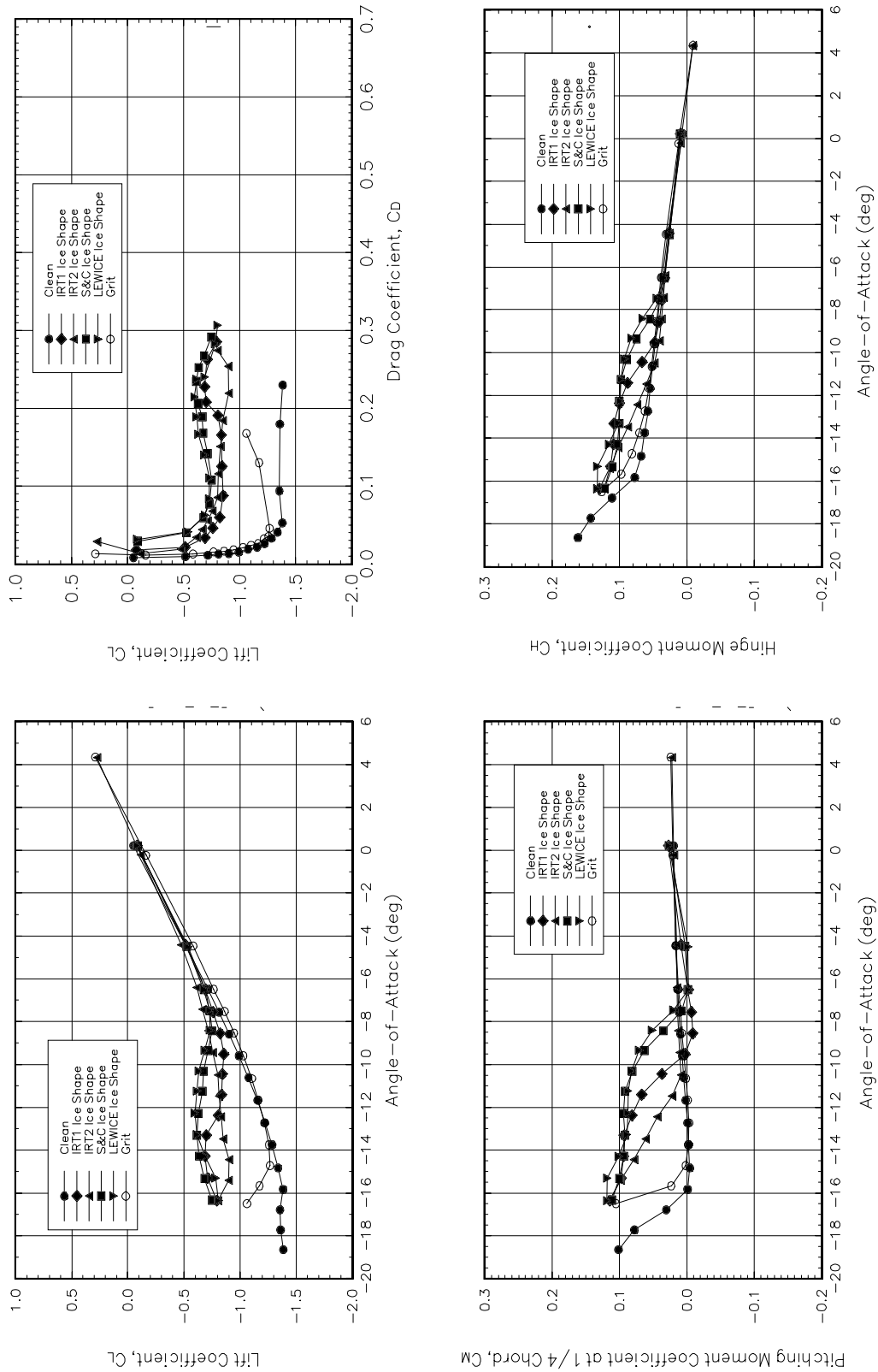


Figure E 7. Ice Shape Effects, Section 2, $\delta e=0.0^\circ$.

Ice Shape Effects, $V=60$ kts, Section 2, $\delta e=10.0^\circ$

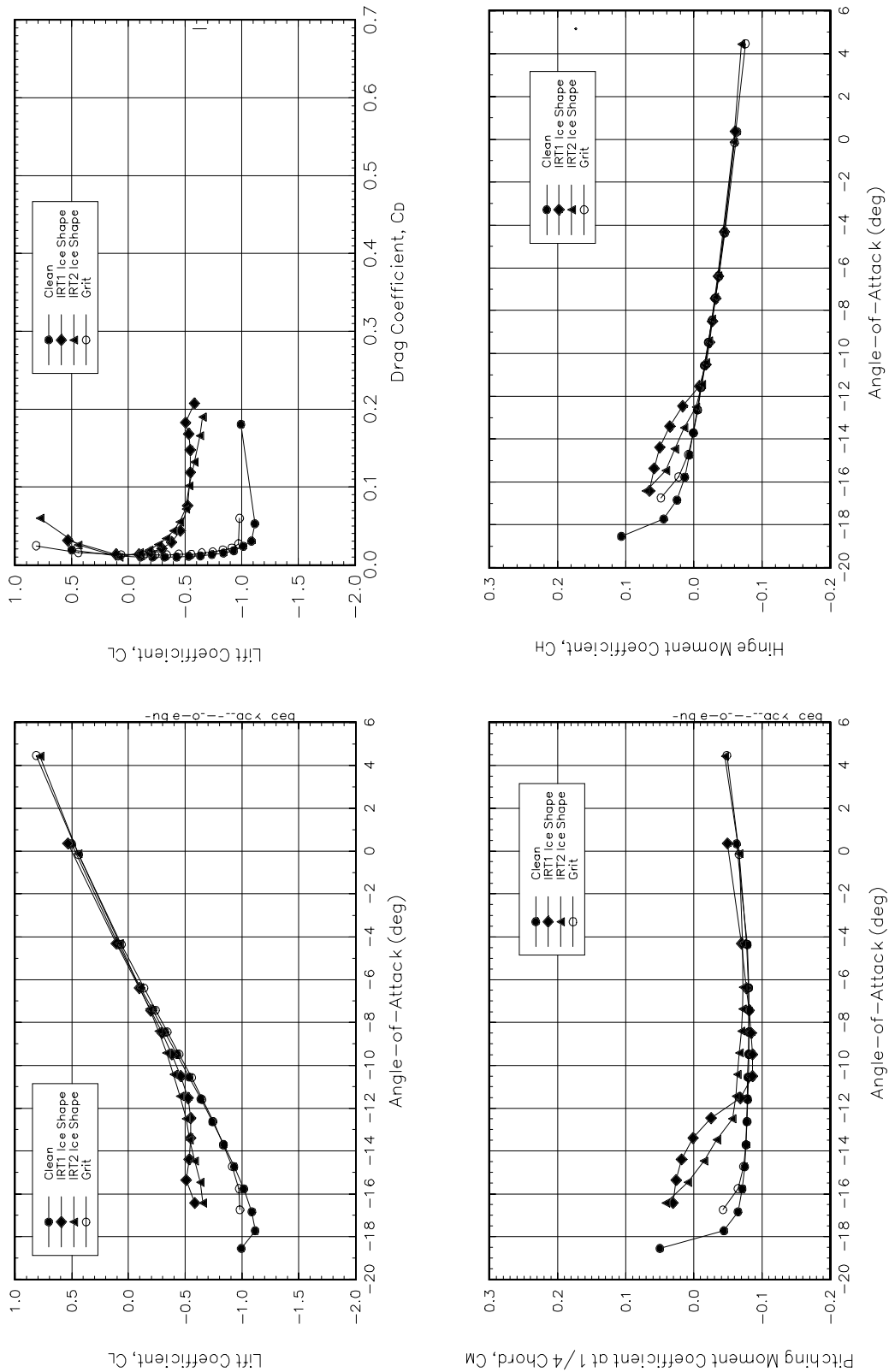


Figure E 8. Ice Shape Effects, Section 2, $\delta e=10.0^\circ$.

Ice Shape Effects, $V=60$ kts, Section 2, $\delta e=14.2^\circ$

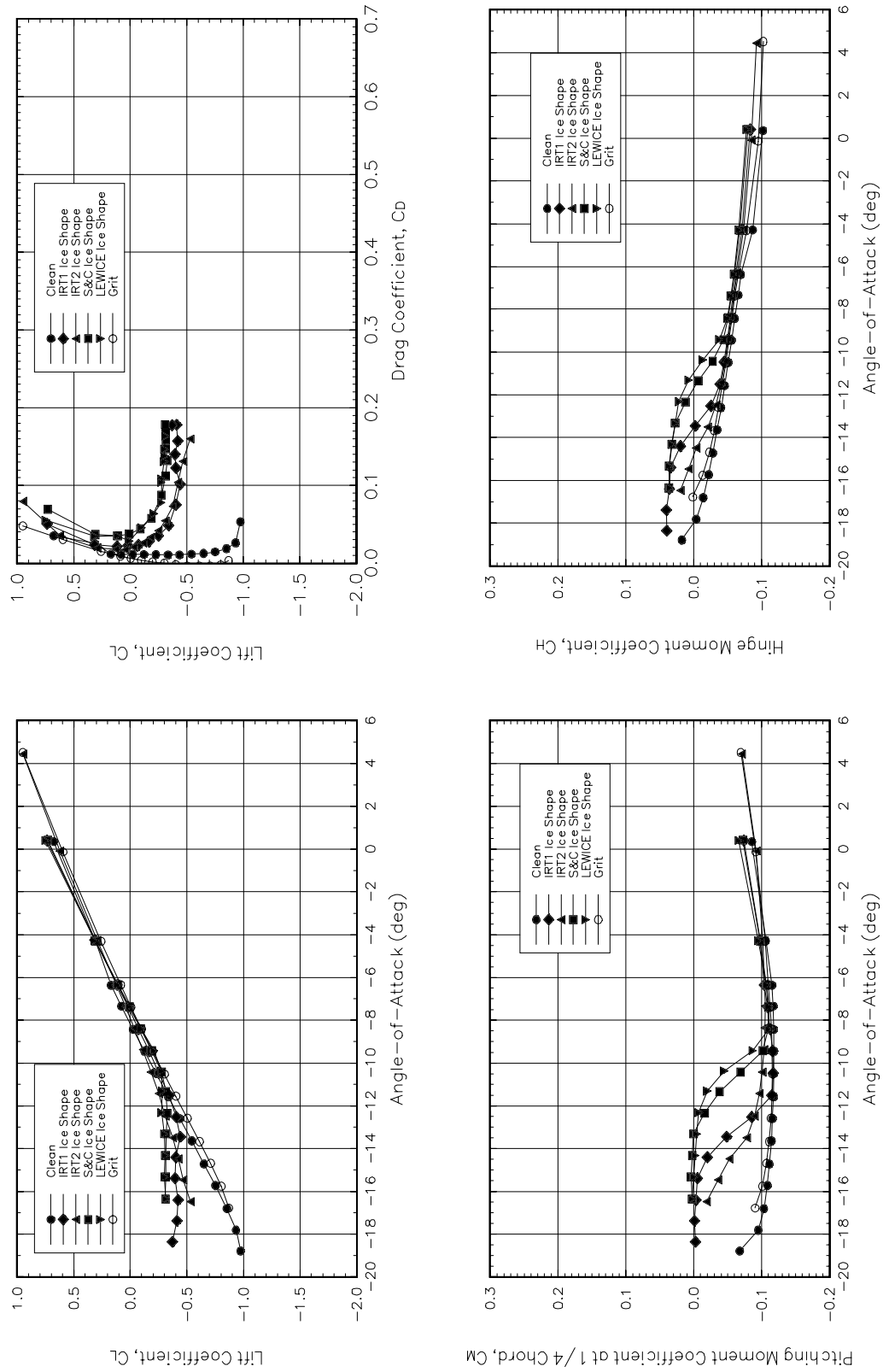


Figure E 9. Ice Shape Effects, Section 2, $\delta e=14.2^\circ$.

Ice Shape Effects, $V=60$ kts, Section 2, $\delta e=-10.0$

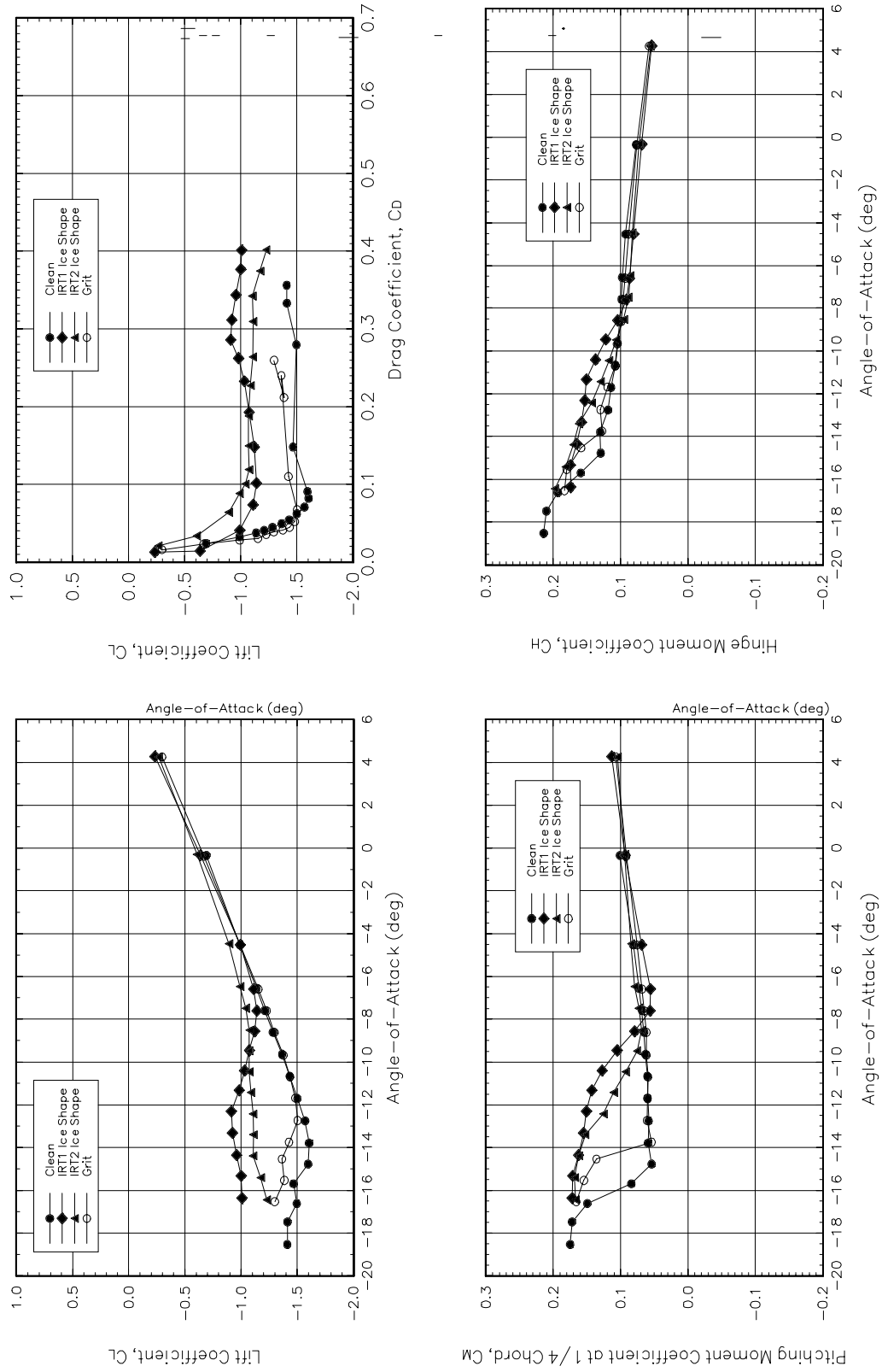


Figure E 10. Ice Shape Effects, Section 2, $\delta e=-10.0^\circ$.

Ice Shape Effects, $V=60$ kts, Section 2, $\delta e=-20.0$

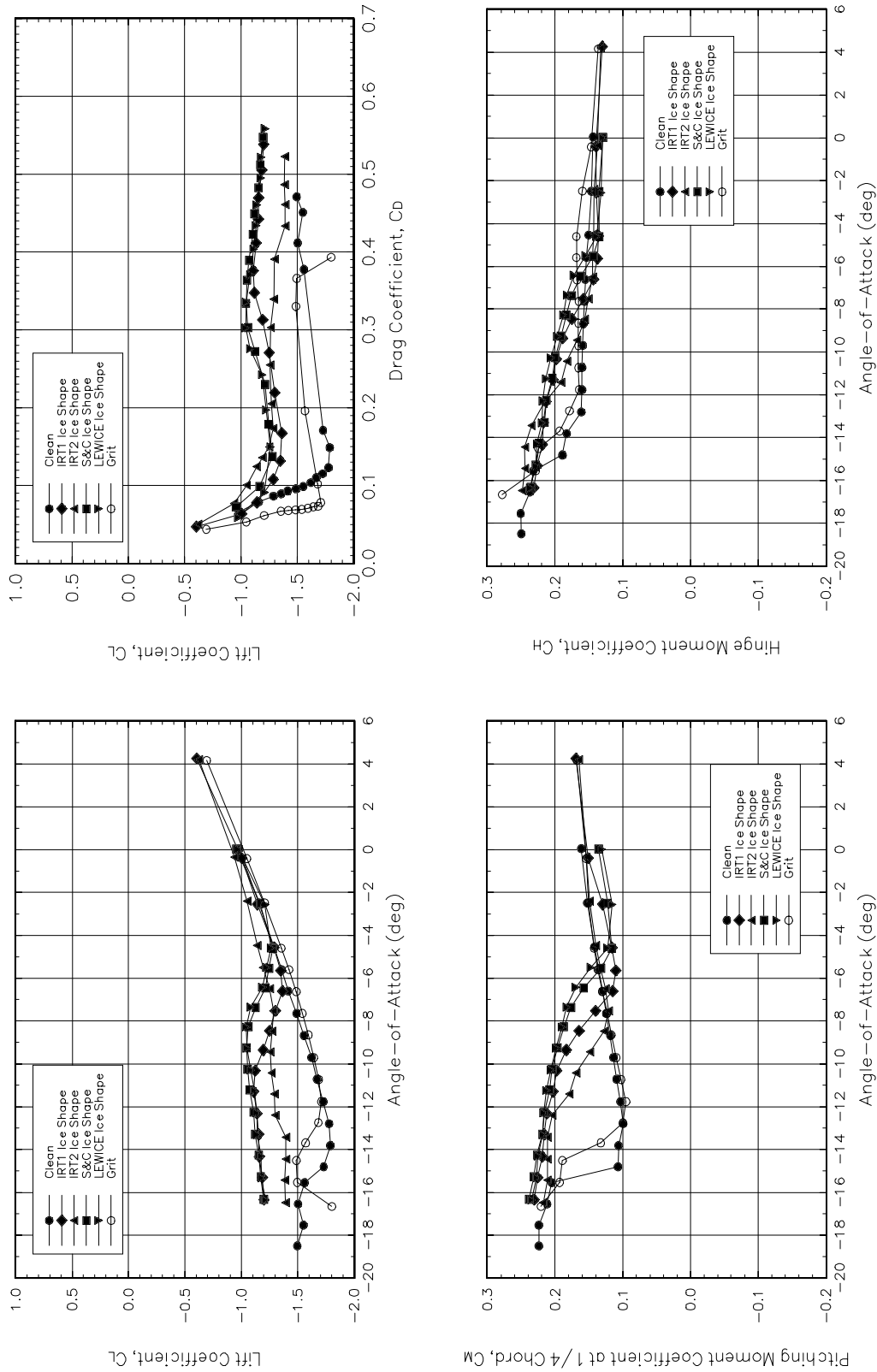


Figure E 11. Ice Shape Effects, Section 2, $\delta e=-20.0^\circ$.

Section Effects, Clean, $V=60$ kts, Large δe 's

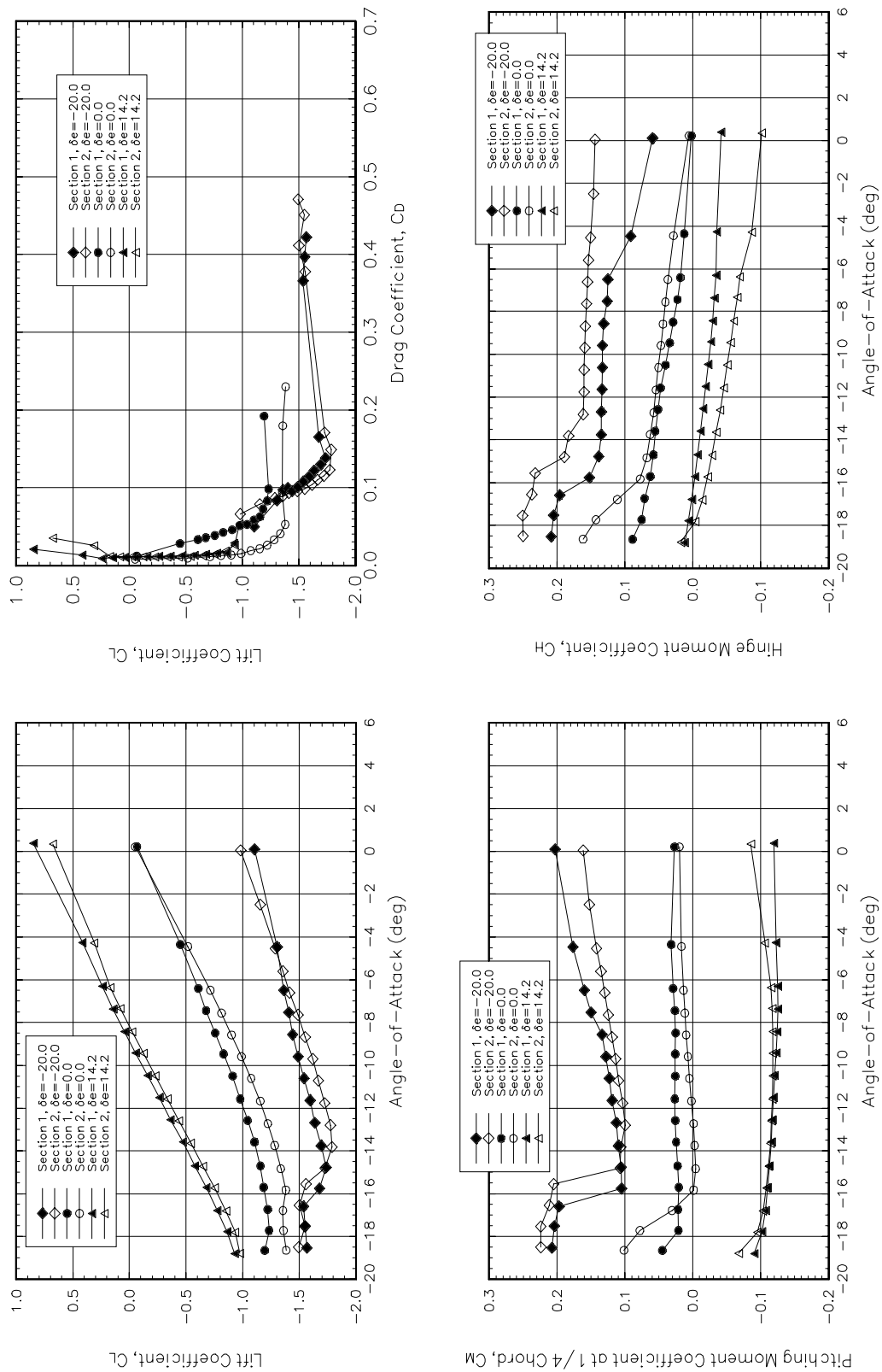


Figure E 12. Section Effects, Clean, Large Elevator Deflections.

Section Effects, IRT1 Ice Shape, $V=60$ kts, Small δe 's

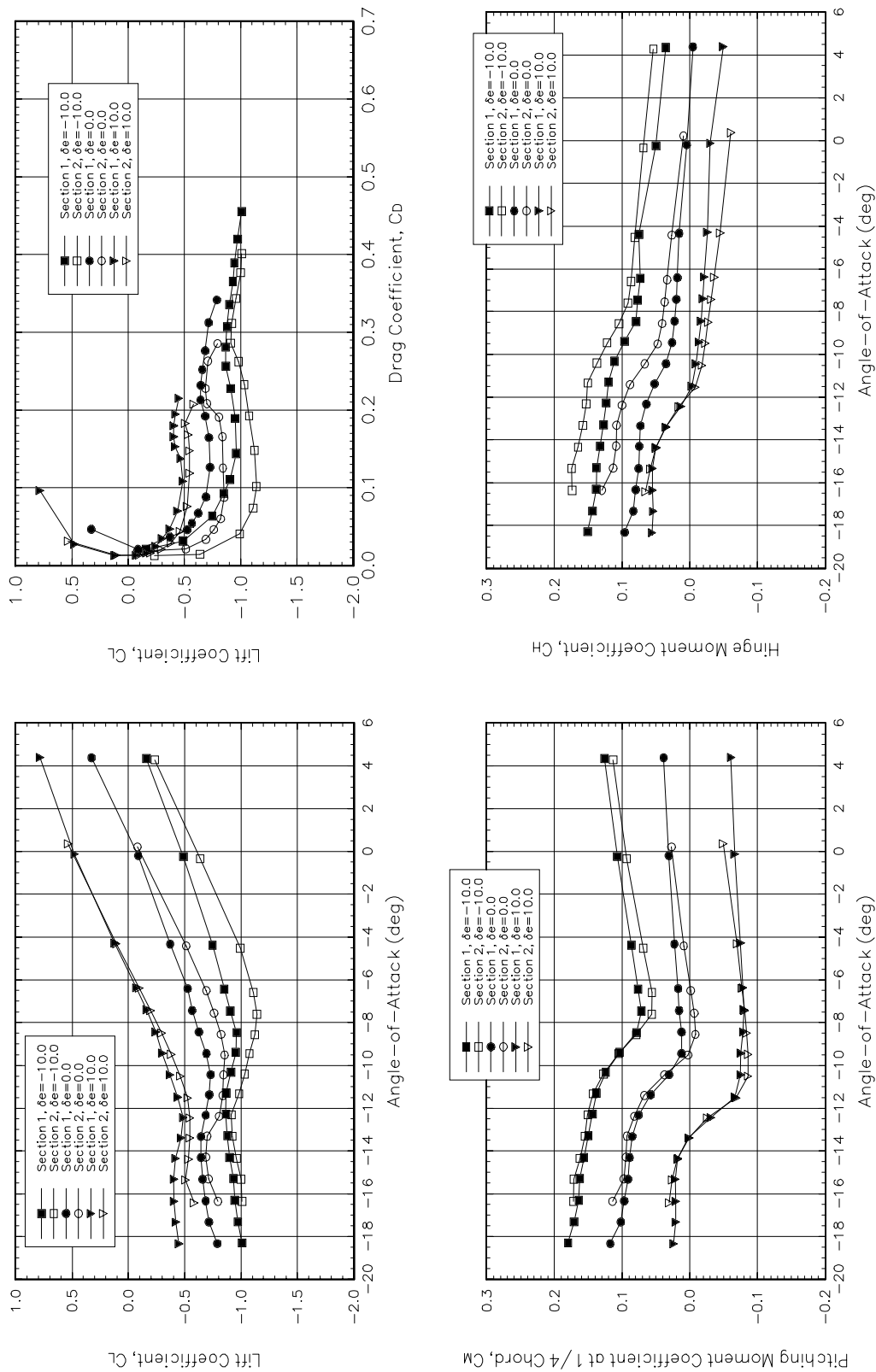


Figure E 13. Section Effects, IRT1 Ice Shape, Small Elevator Deflections.

Section Effects, IRT1, V=60 kts, Large δe 's

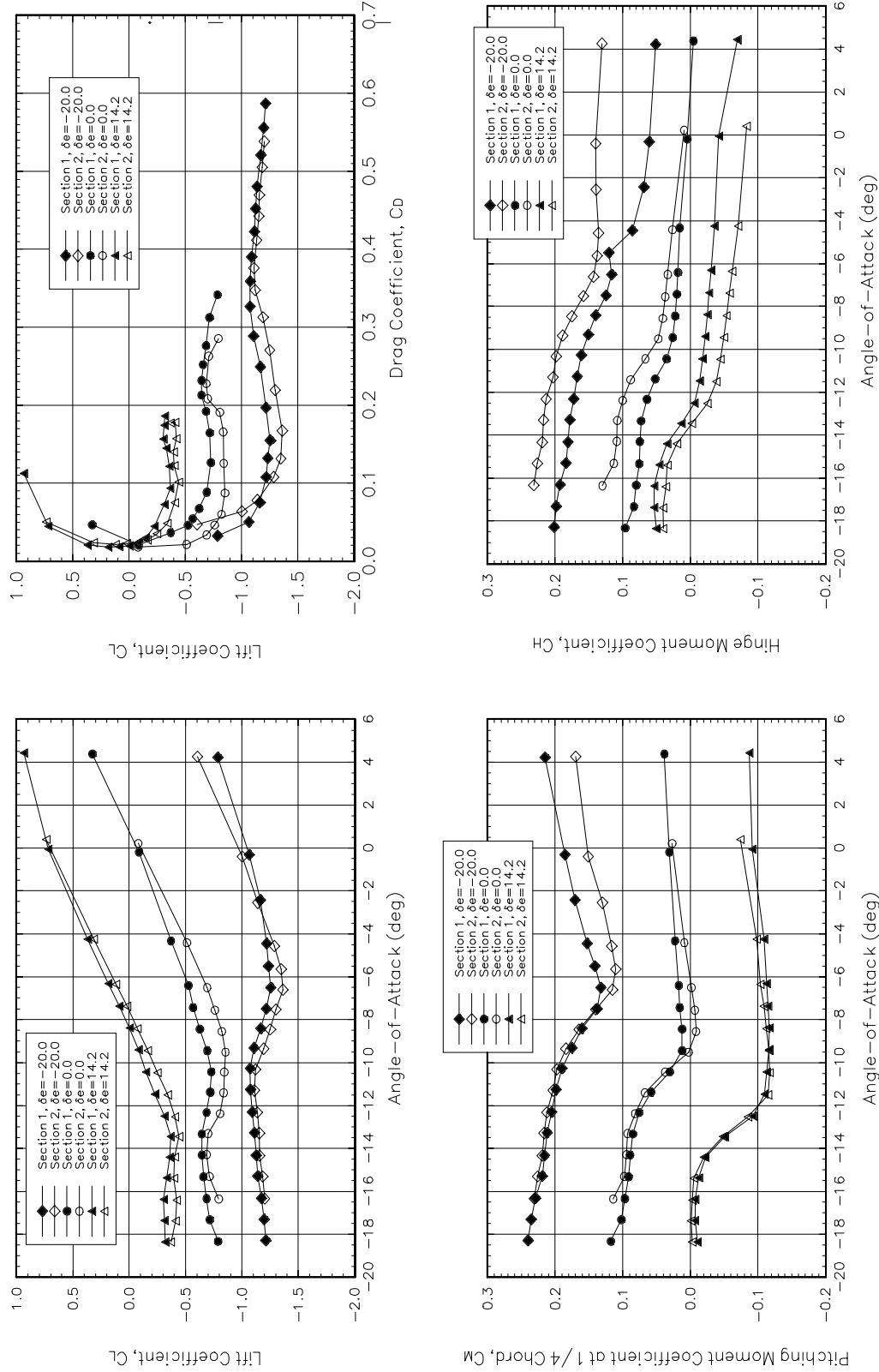


Figure E 14. Section Effects, IRT1 Ice Shape, Large Elevator Deflections.

Section Effects, IRT2 Ice Shape, $V=60$ kts, Small δe 's

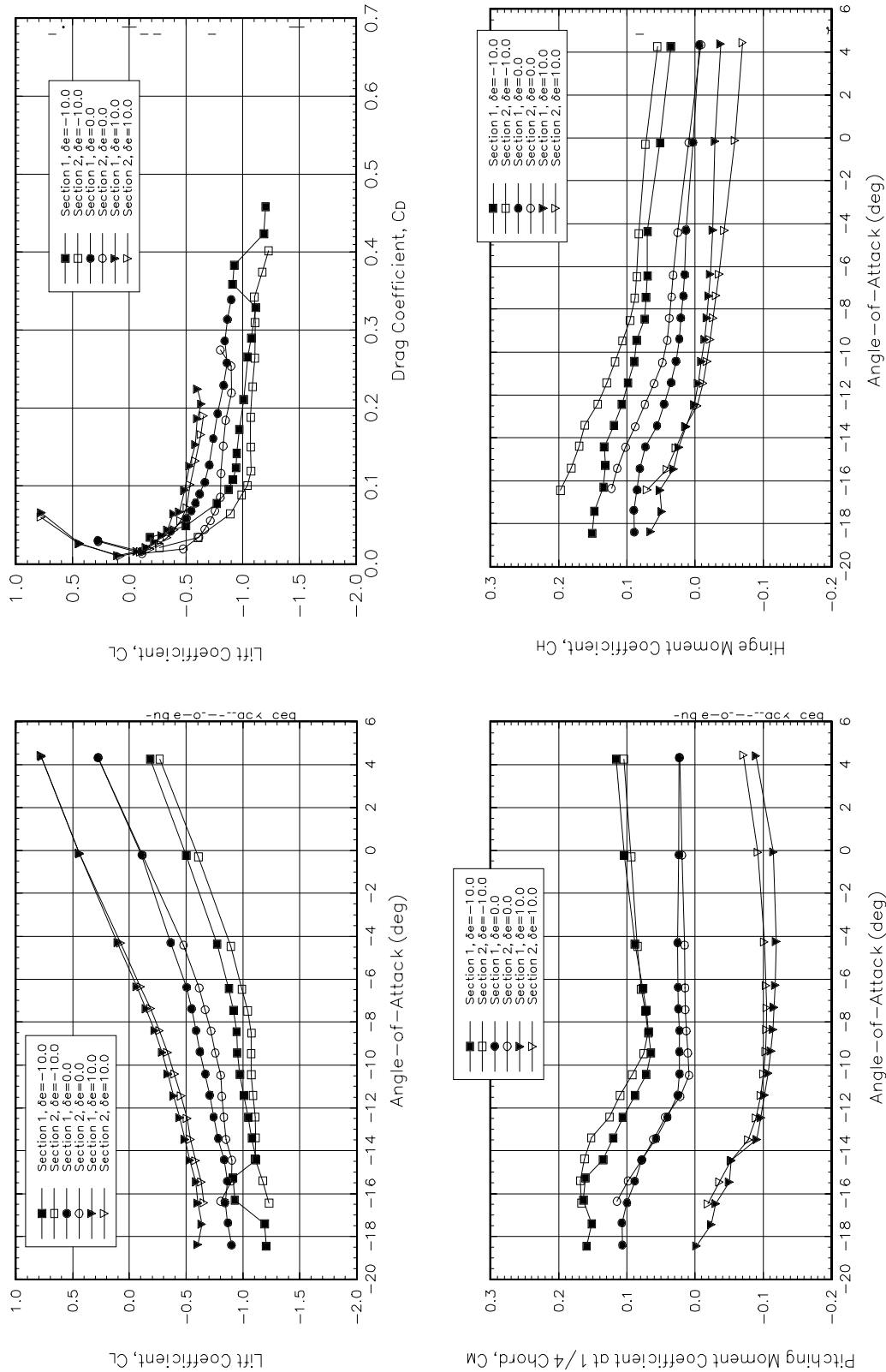


Figure E 15. Section Effects, IRT2 Ice Shape, Small Elevator Deflections.

Section Effects, IRT2, V=60 kts, Large δe 's

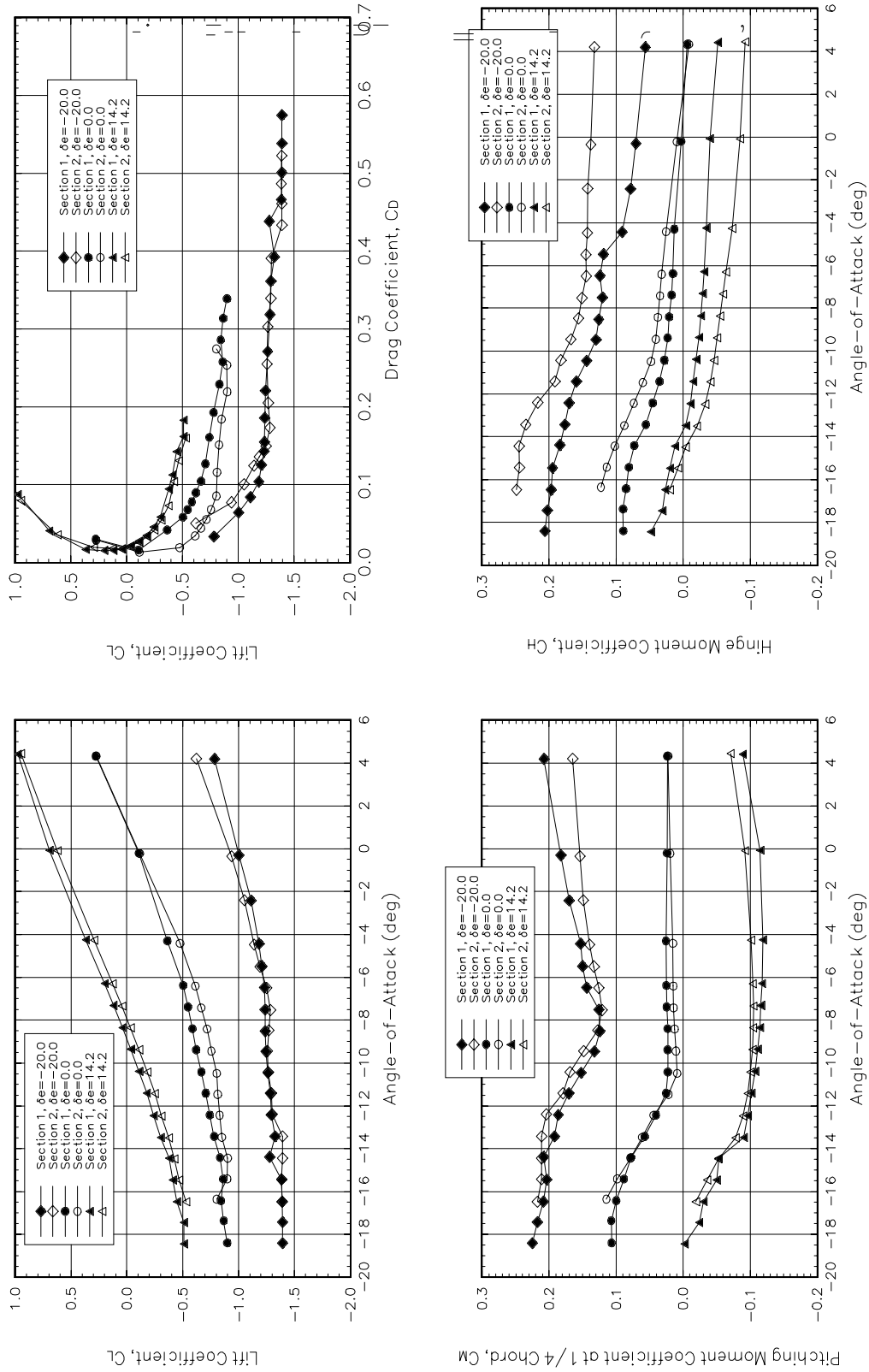


Figure E 16. Section Effects, IRT2 Ice Shape, Large Elevator Deflections.

Section Effects, LEWICE Ice Shape, $V=60$ kts, Large δe 's

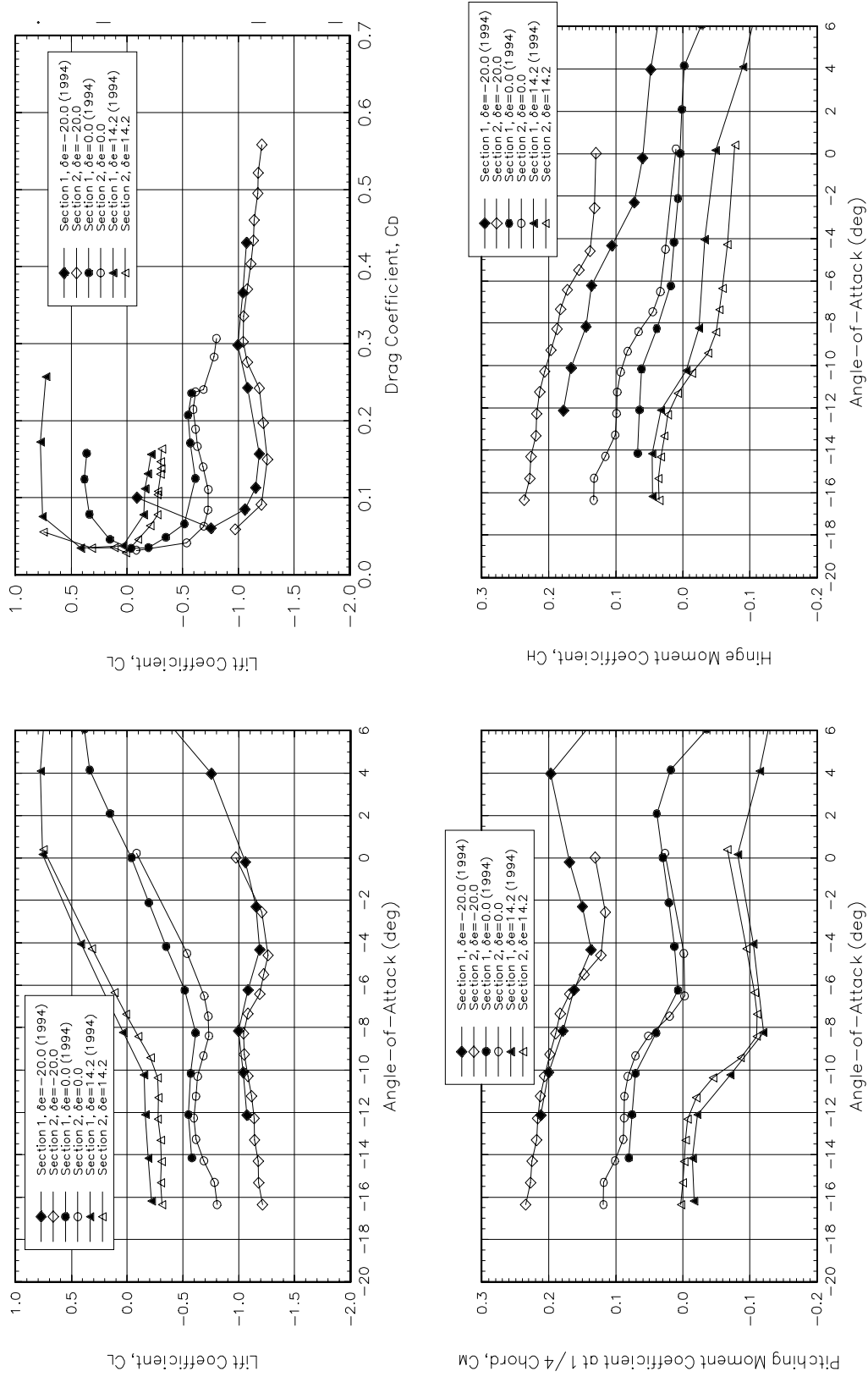


Figure E 17. Section Effects, LEWICE Ice Shape, Large Elevator Deflections.

Section Effects, S&C Ice Shape, V=60 kts, Large δe 's

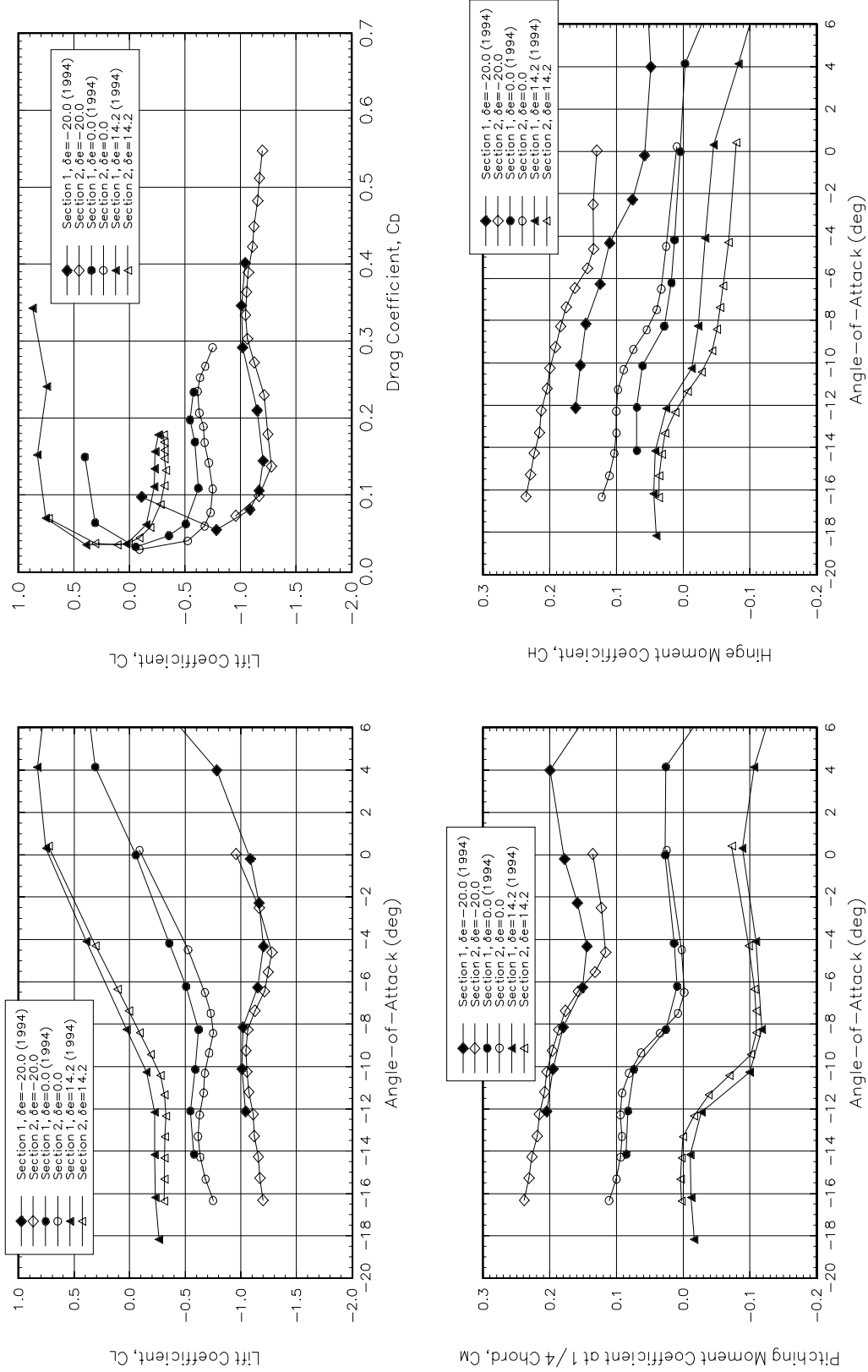
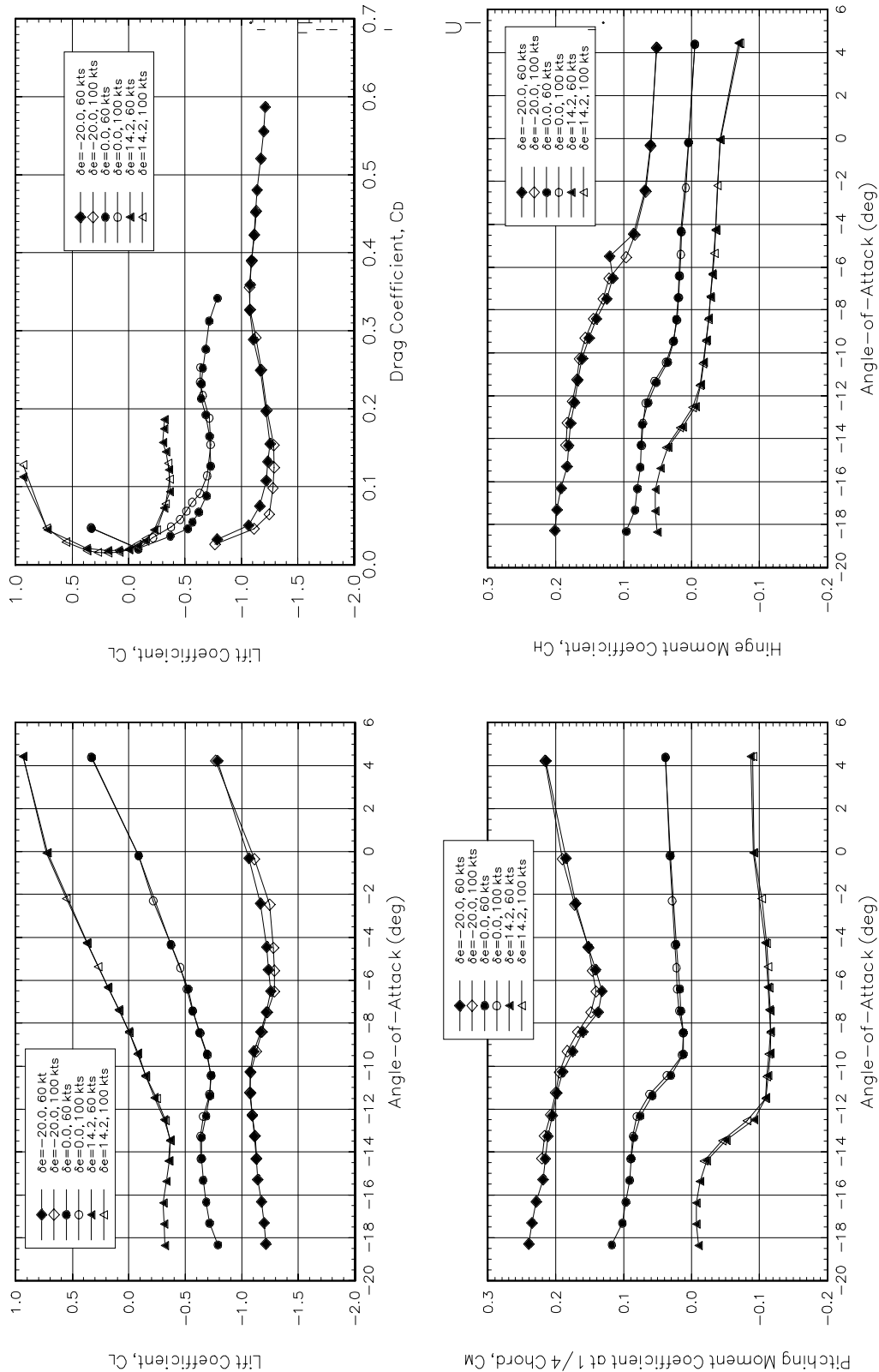


Figure E 18. Section Effects, S&C Ice Shape, Large Elevator Deflections.

Velocity Effects, IRT1, Section 1



**Figure E 19. Velocity Effects, IRT1 Ice Shape, Section 1,
Large Elevator Deflections.**

Velocity Effects, IRT2, Section 1

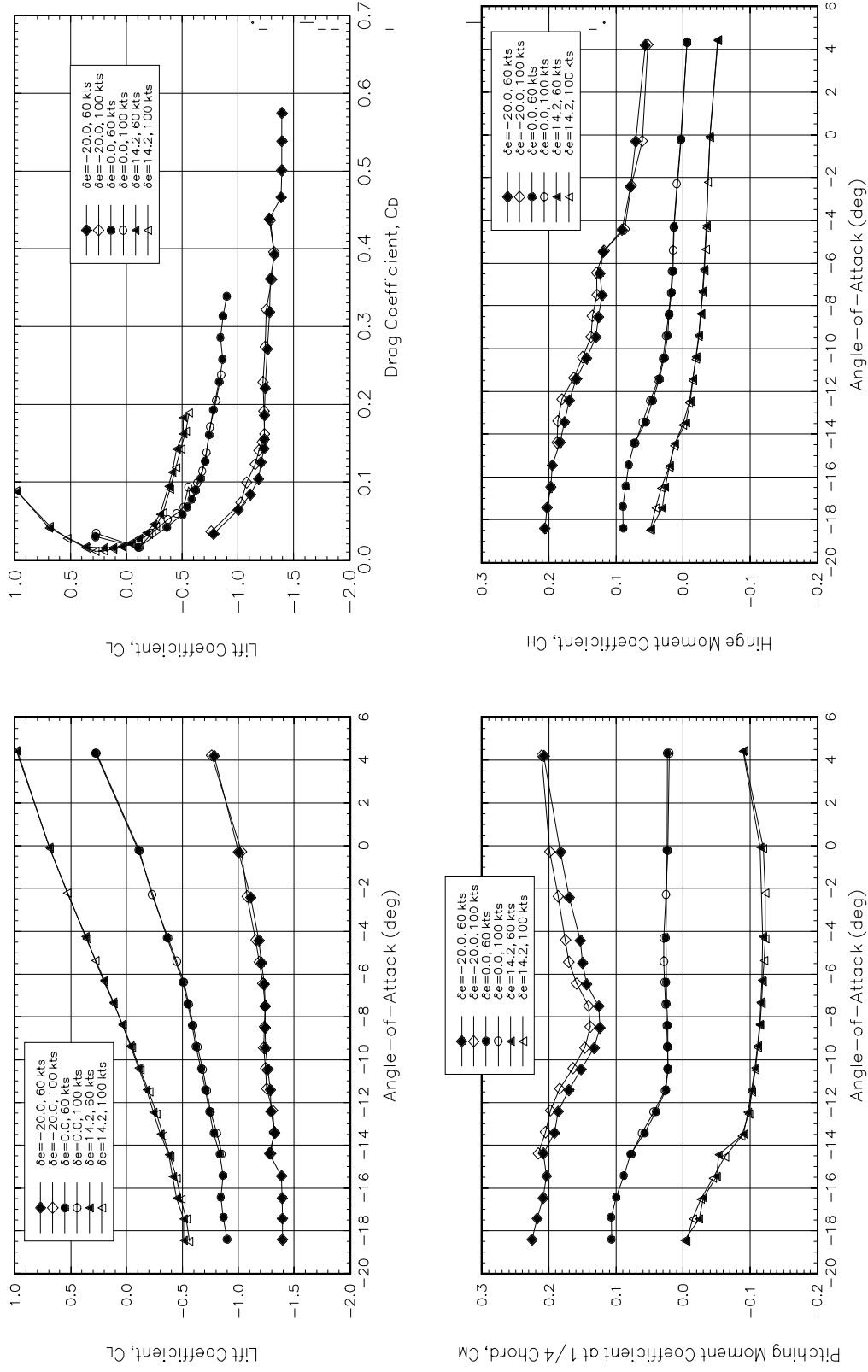


**Figure E 20. Velocity Effects, IRT2 Ice Shape, Section 1,
Large Elevator Deflections.**

Clean, V=60 kts, Section 1

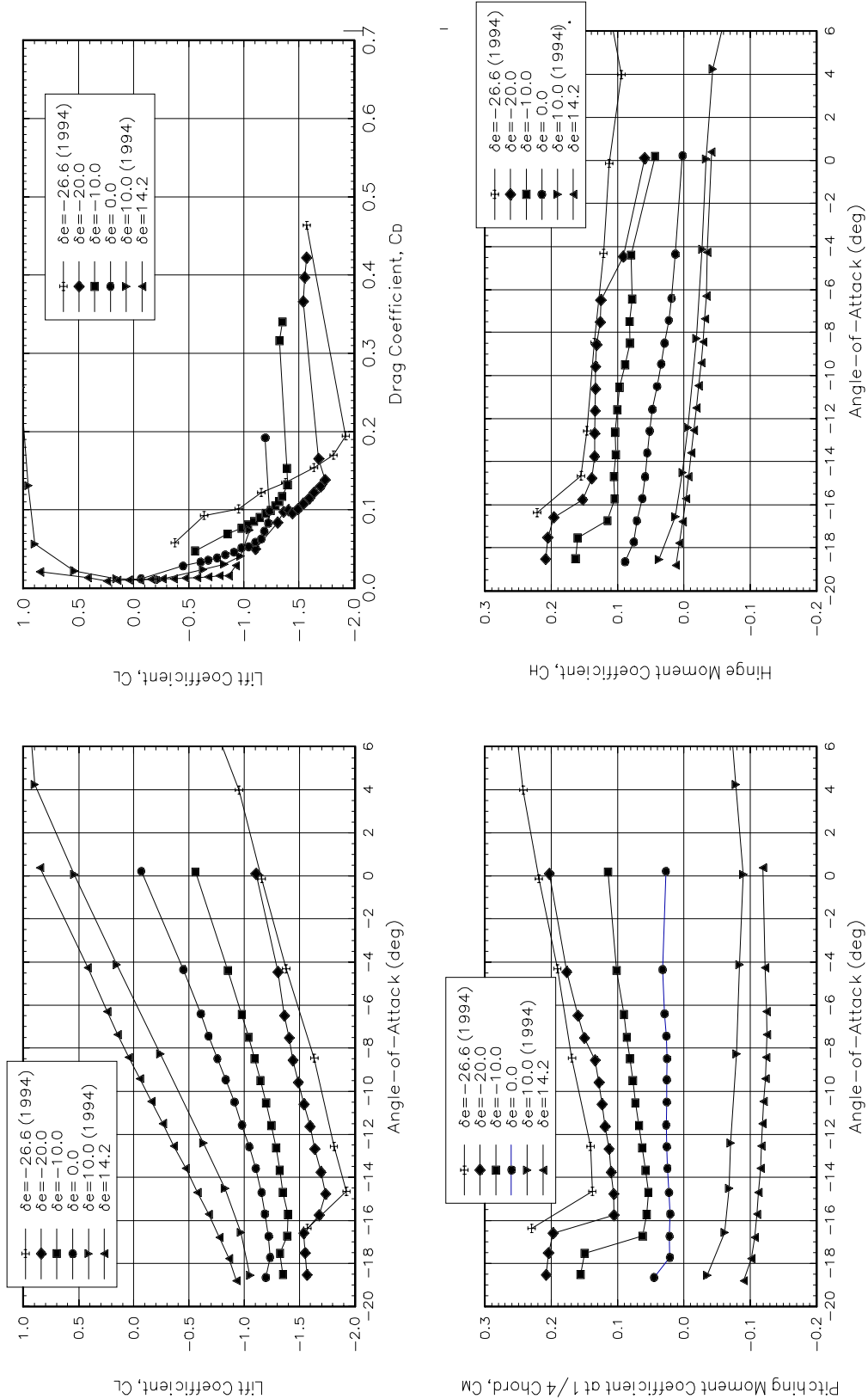


Figure E 21. Clean, Section 1.

Clean, V=60 kts, Section 2

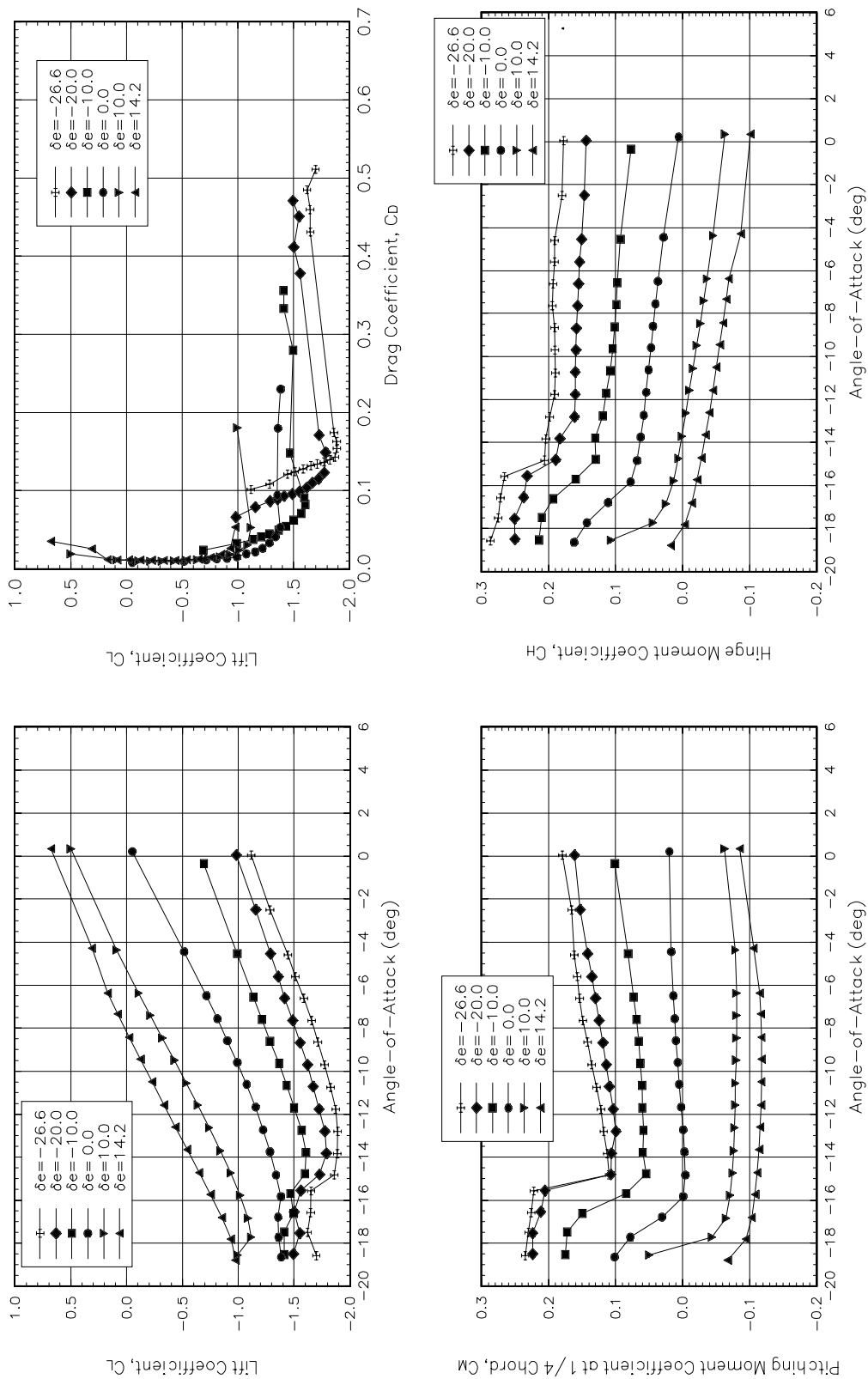


Figure E 22. Clean, Section 2.

Grit, V=60 kts, Section 2

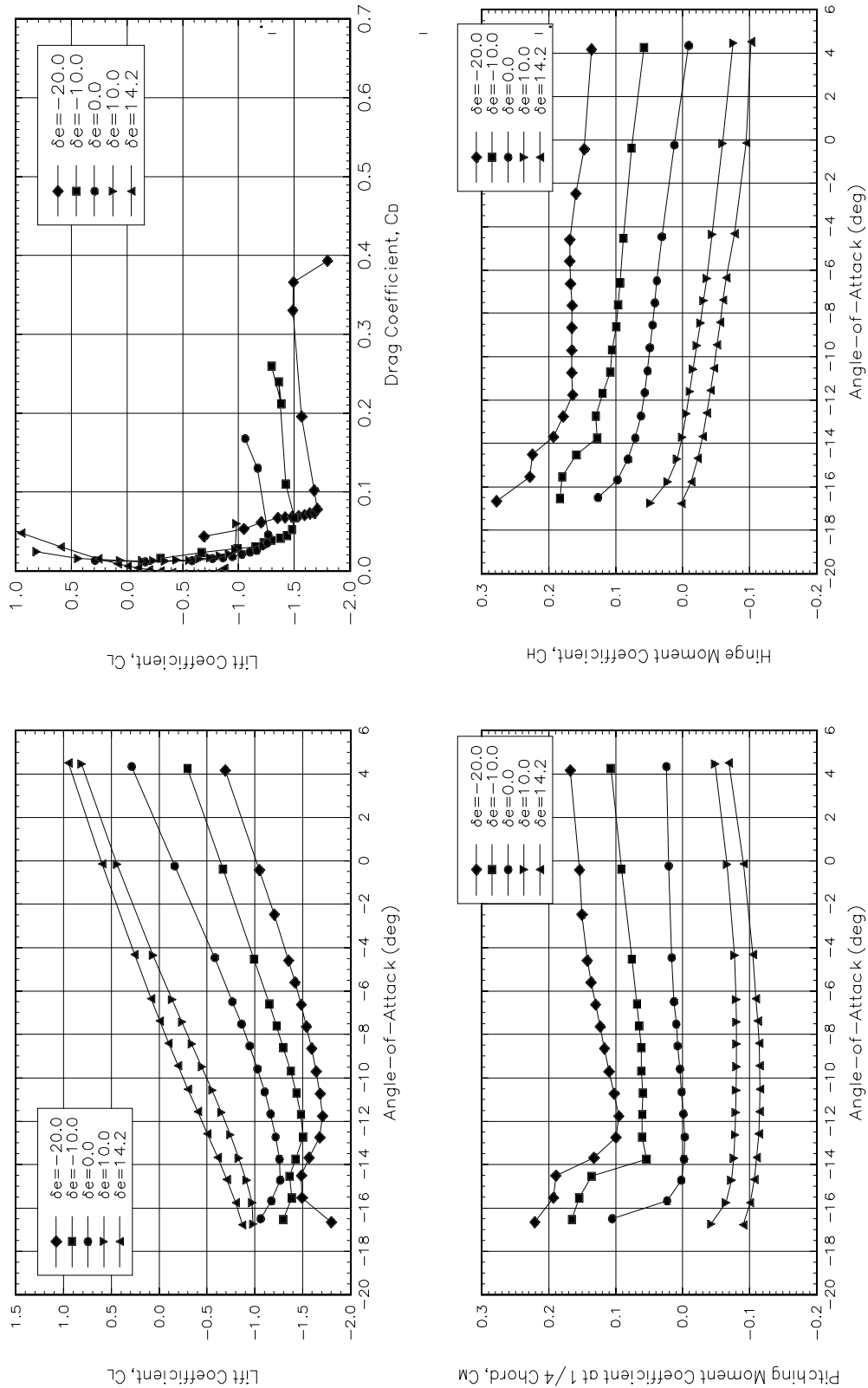


Figure E 23. Grit Applied, Section 2.

IRT1 Ice Shape, V=60 kts, Section 1

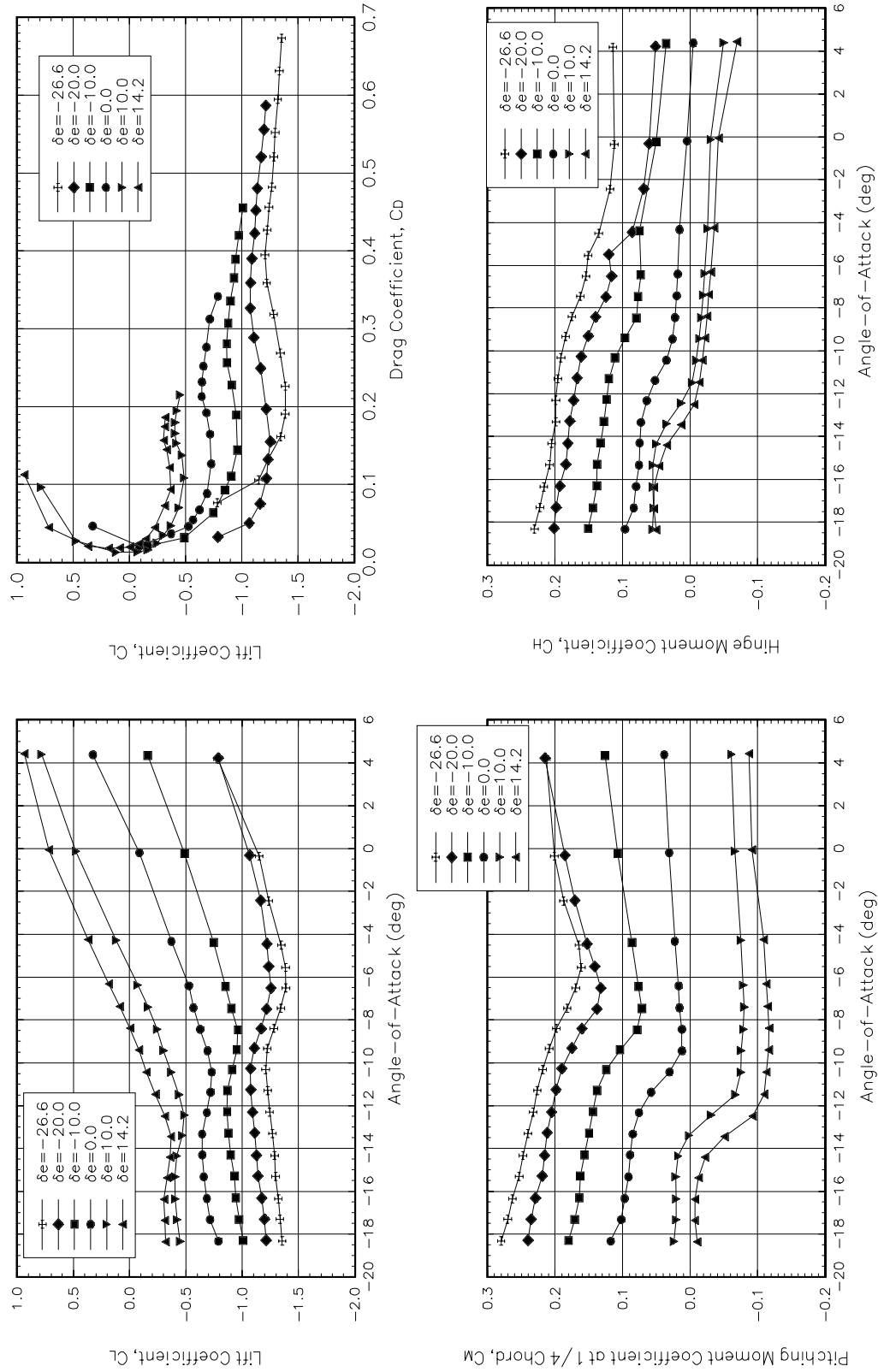
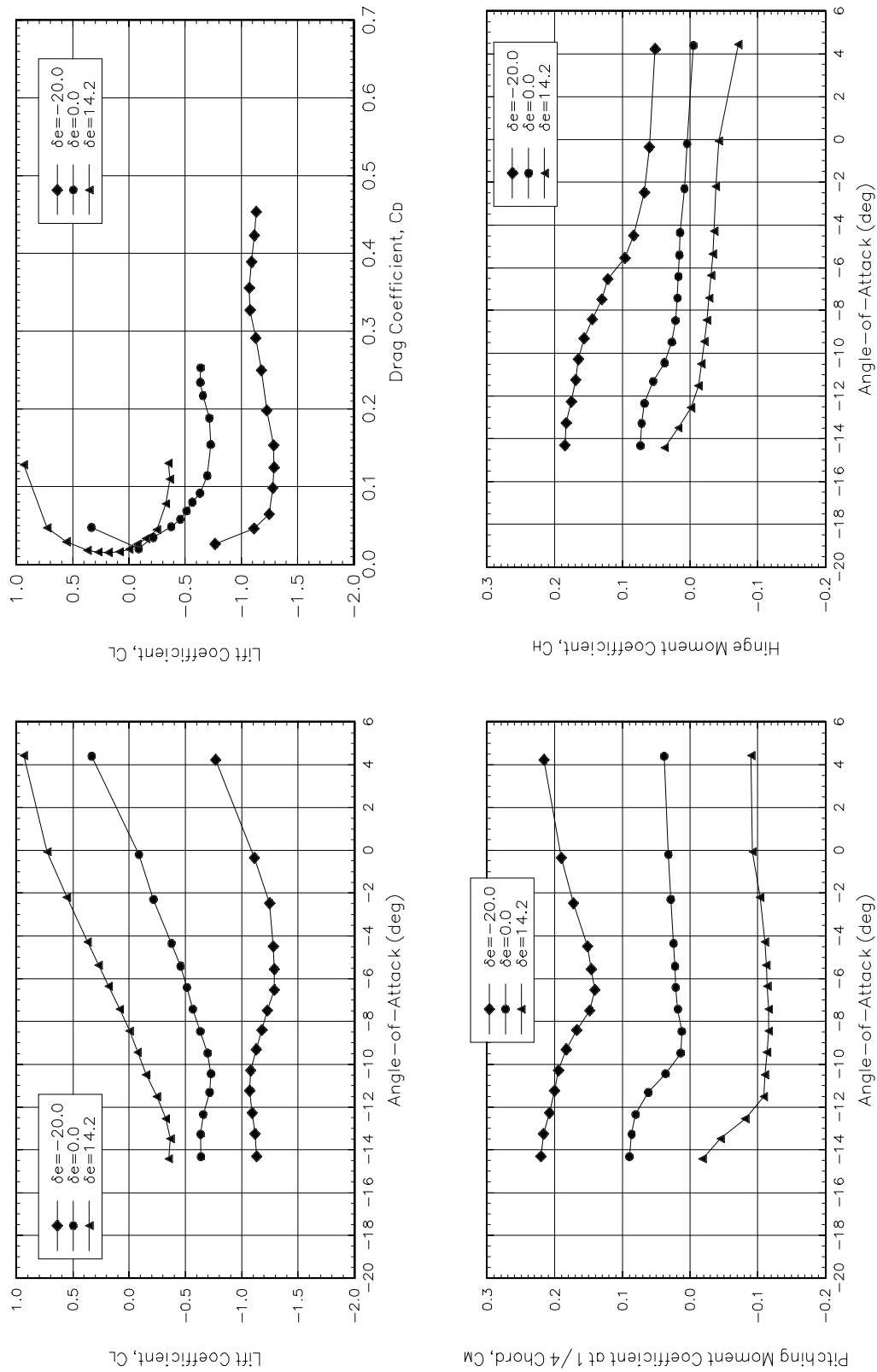


Figure E 24. IRT1 Ice Shape, Section 1, V=60 kts.

IRT1 Ice Shape, $V=100$ kts, Section 1Figure E 25. IRT1 Ice Shape, Section 1, $V=100$ kts.

IRT1 Ice Shape, V=60 kts, Section 2

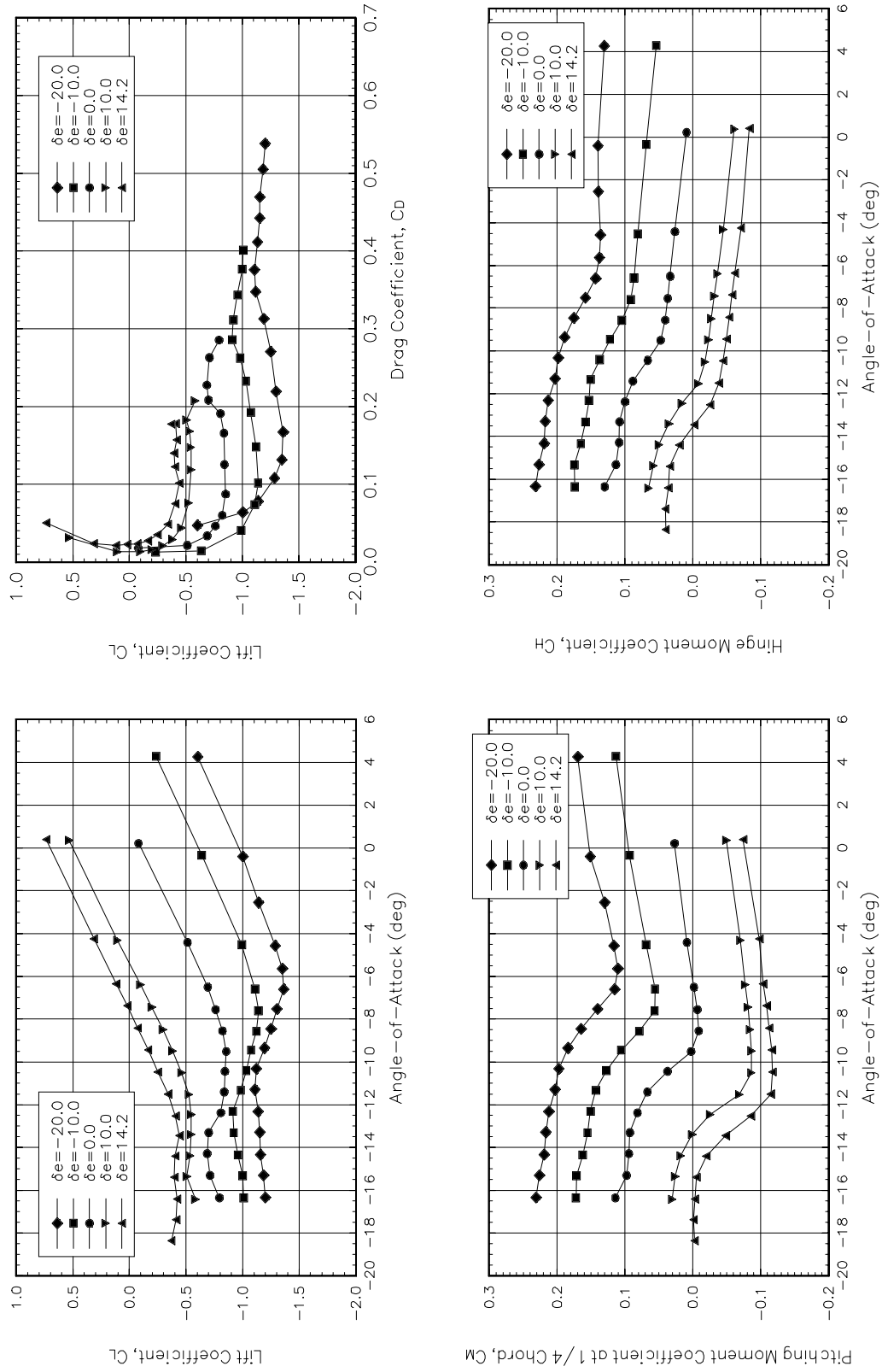
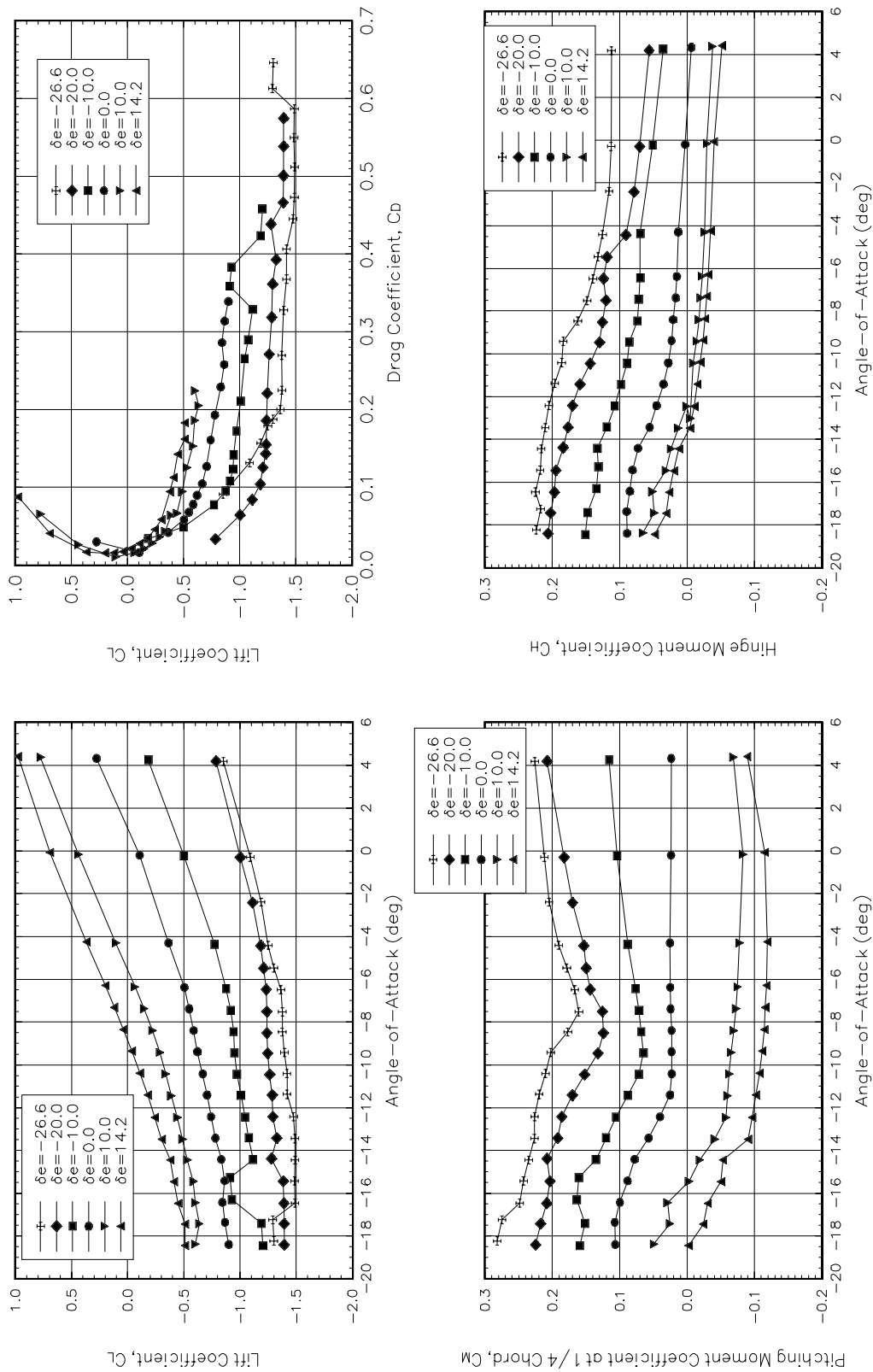


Figure E 26. IRT1 Ice Shape, Section 2.

IRT2 Ice Shape, $V=60$ kts, Section 1Figure E 27. IRT2 Ice Shape, Section 1, $V=60$ kts.

IRT2 Ice Shape, V=100 kts, Section 1

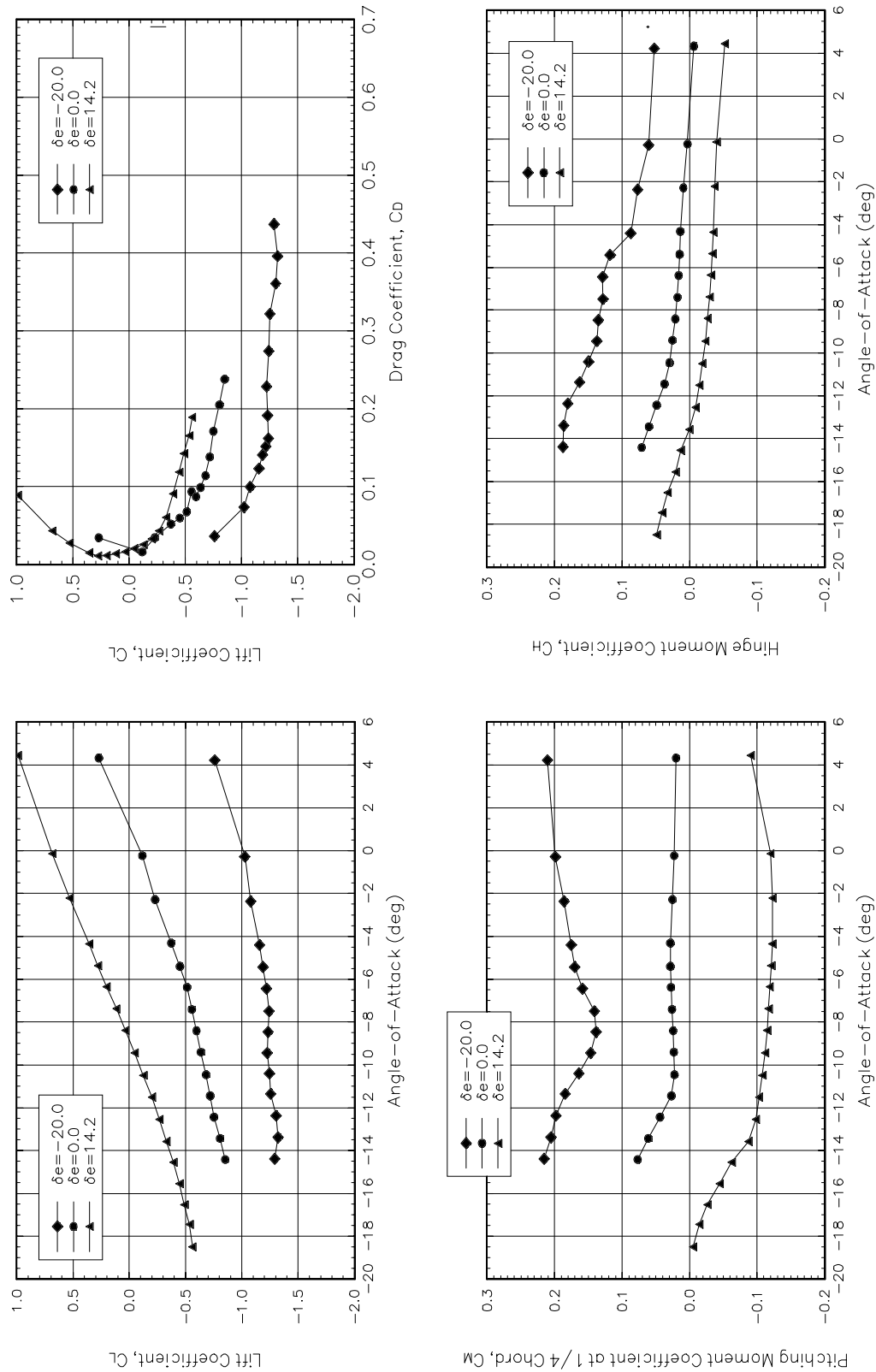


Figure E 28. IRT2 Ice Shape, Section 1, V=100 kts.

IRT2 Ice Shape, V=60 kts, Section 2

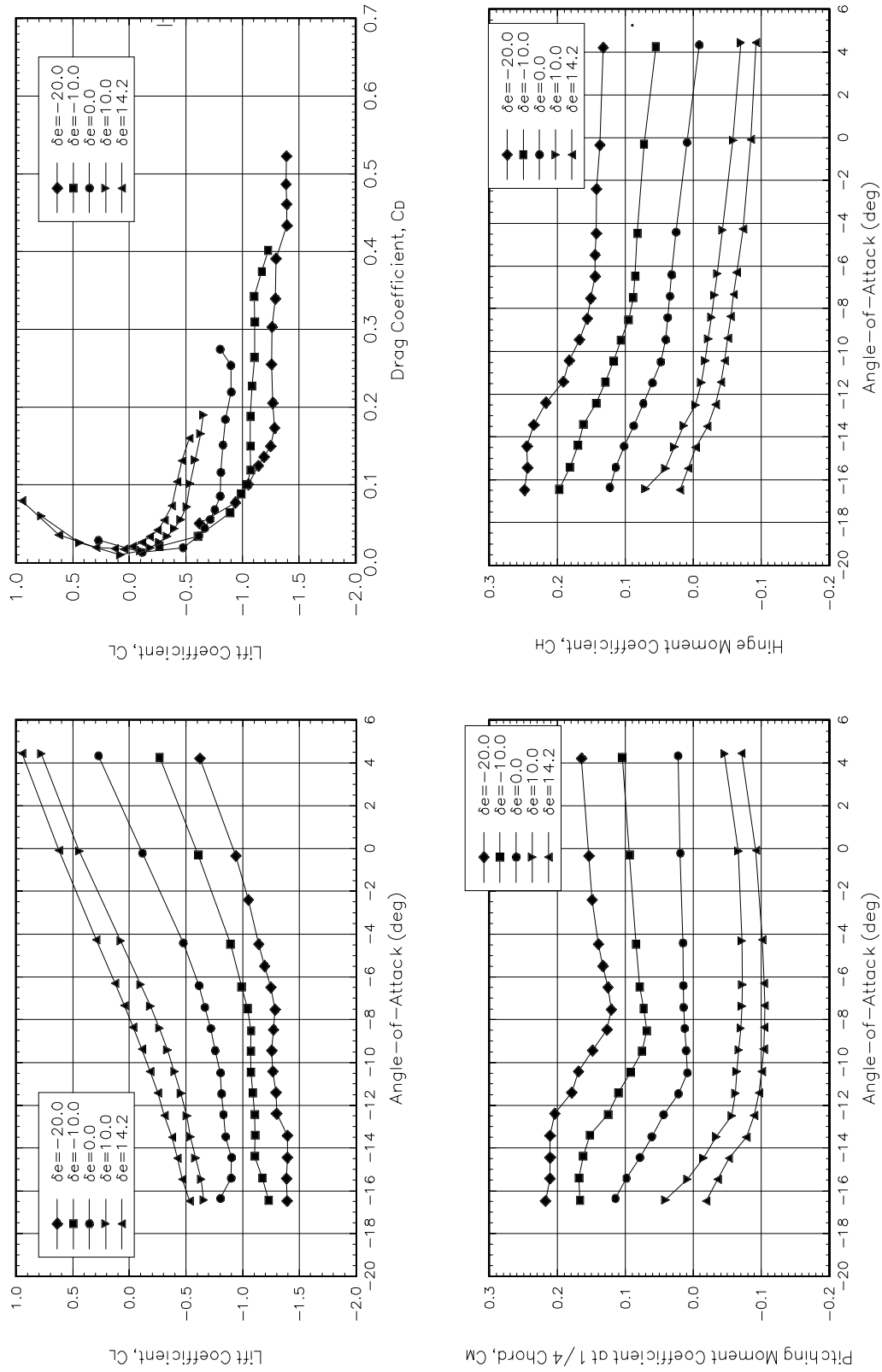


Figure E 29. IRT2 Ice Shape, Section 2.

Appendix F

IRT Ice Shape Information

The information shown below was provided by Thomas Ratvasky, NASA Flight Research Engineer.

IRT1 Ice Shape

Represents the leading edge ice buildup after failure of a de-icing boot.

Airspeed:	135 kts
Angle-of-attack:	-2.9°
Icing time:	22 minutes
LWC:	0.5 g/m ³
Total Temp:	24.3 °F
MVD:	20 microns

IRT2 Ice Shape

Represents the amount of leading edge ice accreted between de-icing boot cycles.

Airspeed:	135 kts
Angle-of-attack:	-2.9°
Icing time:	15 minutes with de-icing boot cycles every 3 minutes, so the final accretion is the residual ice left after the deicer cycle at 12 minutes plus the last 3 minutes of growth.
LWC:	0.5 g/m ³
Total Temp:	24.3 °F
MVD:	20 microns

References

- 1) Hiltner, D., DHC-6 Twin Otter Tailplane Airfoil Section Testing in the Ohio State University 7x10 Wind Tunnel, Aerospace Engineering, The Ohio State University, Columbus, Ohio, NASA/CR—2000-209921/VOL1, 2000.
- 2) Rae, W. and Pope, A., Low Speed Wind Tunnel Testing, Wiley-Interscience, 1984.

REPORT DOCUMENTATION PAGE			Form Approved OMB No. 0704-0188	
Public reporting burden for this collection of information is estimated to average 1 hour per response, including the time for reviewing instructions, searching existing data sources, gathering and maintaining the data needed, and completing and reviewing the collection of information. Send comments regarding this burden estimate or any other aspect of this collection of information, including suggestions for reducing this burden, to Washington Headquarters Services, Directorate for Information Operations and Reports, 1215 Jefferson Davis Highway, Suite 1204, Arlington, VA 22202-4302, and to the Office of Management and Budget, Paperwork Reduction Project (0704-0188), Washington, DC 20503.				
1. AGENCY USE ONLY (Leave blank)		2. REPORT DATE September 2000		3. REPORT TYPE AND DATES COVERED Final Contractor Report
4. TITLE AND SUBTITLE Additional Testing of the DHC-6 Twin Otter Tailplane Iced Airfoil Section in the Ohio State University 7x10 Low Speed Wind Tunnel			5. FUNDING NUMBERS WU-548-21-23-00 NAG3-1574	
6. AUTHOR(S) Gerald Gregorek, John J. Dresse, and Karine La Noé				
7. PERFORMING ORGANIZATION NAME(S) AND ADDRESS(ES) Ohio State University Research Foundation 1960 Kenny Road Columbus, Ohio 43210-1063			8. PERFORMING ORGANIZATION REPORT NUMBER E-12159-2	
9. SPONSORING/MONITORING AGENCY NAME(S) AND ADDRESS(ES) National Aeronautics and Space Administration John H. Glenn Research Center at Lewis Field Cleveland, Ohio 44135-3191			10. SPONSORING/MONITORING AGENCY REPORT NUMBER NASA CR-2000-209921-VOL2	
11. SUPPLEMENTARY NOTES Project Manager, Thomas Ratvasky, Turbomachinery and Propulsion Systems Division, NASA Glenn Research Center, organization code 5840, (216) 433-3905.				
12a. DISTRIBUTION/AVAILABILITY STATEMENT Unclassified - Unlimited Subject Categories: 02 and 05 This publication is available from the NASA Center for AeroSpace Information, (301) 621-0390.			12b. DISTRIBUTION CODE	
13. ABSTRACT (Maximum 200 words) The need for fundamental research in Ice Contaminated Tailplane Stall (ICTS) was established through three international conferences sponsored by the FAA. A joint NASA/FAA Tailplane Icing Program was formed in 1994 with the Ohio State University playing a critical role for wind tunnel and analytical research. Two entries of a full-scale 2-dimensional tailplane airfoil model of a DHC-6 Twin Otter were made in The Ohio State University 7'x10' wind tunnel. This report describes the second test entry that examined additional ice shapes and roughness, as well as airfoil section differences. The addition data obtained in this test fortified the original database of aerodynamic coefficients that permit a detailed analysis of flight test results with an OSU-developed analytical program. The testing encompassed a full range of angles of attack and elevator deflections at flight Reynolds number conditions. Aerodynamic coefficients, C_L , C_M , and C_{He} were obtained by integrating static pressure coefficient, C_p , values obtained from surface taps. Comparisons of clean and iced airfoil results show a significant decrease in the tailplane aeroperformance (decreased $C_{L_{max}}$, decreased stall angle, increased C_{He}) for all ice shapes with the grit having the least affect and the LEWICE shape having the greatest affect. All results were consistent with observed tailplane stall phenomena and constitute an effective set of data for comprehensive analysis of ICTS.				
14. SUBJECT TERMS Aircraft icing; Tailplane icing; Airfoil performance			15. NUMBER OF PAGES 89	
			16. PRICE CODE A05	
17. SECURITY CLASSIFICATION OF REPORT Unclassified	18. SECURITY CLASSIFICATION OF THIS PAGE Unclassified	19. SECURITY CLASSIFICATION OF ABSTRACT Unclassified	20. LIMITATION OF ABSTRACT	